EXPERIMENTAL ANALYSIS OF FLOW REGIMES PERTAINING TO ELECTROSPINNING FROM A POLYMER DROP

RAHUL

(M. E., BITS, Pilani, India)

A THESIS SUBMITTED

FOR THE DEGREE OF DOCTOR OF PHILOSOPHY

DEPARTMENT OF MECHANICAL ENGINEERING

NATIONAL UNIVERSITY OF SINGAPORE

2012

Declaration

I hereby declare that this thesis is my original work and it has been written by me in its entirety.

I have duly acknowledged all the sources of information, which have been used in the thesis.

This thesis has also not been submitted for any degree in any university previously.

Rahul

5 Dec 2012

Acknowledgments

I would like to thank A/P Teo Chiang Juay for his considerate advice during my Ph.D. research work. He has provided me with ample opportunities to grow and mature as a researcher. His systematic approach to his research work has inspired me to follow his footsteps. Additionally, I would like to thank my Co-supervisor Prof. Chew Yong Tian for his valuable support. I would also like to thank Prof. S. T. Thoroddsen, who initiated the project. Without the teaching and support of these gentlemen, I would not have been able to accomplish the task.

I would like to personally acknowledge the staff member of my research lab, who despite their tough schedule always helped me in design/fabrication of my experimental setups. Last, but not the least I would like to thank the entire Fluid Division of Mechanical Engineering Department for their general support during my entire tenure as a Ph.D. student.

Table of Contents

Summary

The fluid dynamics of an electrospun polymer jet is thoroughly analyzed, and strategies for the effective control of electrospinning for the production of fibers are proposed. Flow regimes pertaining to the electrospun jet are systematically analyzed. These regimes include Taylor cone formation/jet initiation, straight section of the jet and bending/higher-order instabilities experienced by the jet along its trajectory. Dimensional analysis has been performed to identify the salient dimensionless parameters, which govern the characteristics of the Taylor cone and the straight section of the jet. Correlation formulae presented in terms of the salient dimensionless parameters allow the resultant jet characteristics to be correlated with the operating parameters. These jet characteristics include the jet diameter at the apex of the Taylor cone, jet diameter at different locations along the jet's straight section, as well as the length of the straight section of the jet.

Three dimensionless parameters are found to govern the jet characteristics at the apex of the Taylor cone. These dimensionless parameters include dimensionless flow rate, electric field, and diameter of the electrospun jet. For the straight section of the jet, four dimensionless parameters are found to govern the evolution of the jet. These are dimensionless electric field, flow rate, axial distance, and diameter of the electrospun jet. Subsequently, two of these dimensionless parameters are combined to yield a three-parameter system. Additionally, three dimensionless parameters are found to govern the length of the straight section of the jet. Subsequently, all these three parameter correlation formulae were reduced to two-parameter systems, assuming that the effects of the dimensionless electric field were weak. The proposed correlation formulae are invaluable for envisioning jet characteristics to control and optimize the electrospinning phenomenon.

Instabilities and failure modes experienced by the electrospun jet are analyzed. These instabilities include bending and branching. In order to characterize bending instability, an imaging system was designed to capture images at different time instances. These time-resolved images enabled the effects of the salient operating parameters to be systematically investigated. The parameters studied include wavelength, growth rate and the phase velocity. The failure modes of the electrospun jet during bending instability have also been investigated. In order to characterize higher-order instabilities, linear stability analyses of the electrified jet incorporating non-Newtonian effects have been performed. The linear stability analysis yields the axial wavelength corresponding to the highest order azimuthal mode. Subsequently, the axial wavelength is compared with the experimentally determined inter-undulation distance. An extensive analysis has been performed to reconcile the differences between the experimental and theoretical results.

Finally, techniques for the effective control of electrospinning have been proposed. In the first technique, a pulsed laser is focused onto the interior of the surface of the drop close to the liquid-air interface to overcome surface tension and produce an electrified jet. This approach can reduce the required applied electric field to half its value necessary for conventional electrospinning. Another technique proposed yields regular-sized microfibers through near-field electrospinning. Mass production of fibers can be rendered feasible using these technologies.

List of Tables

List of figures

List of symbols

Symbol	Description	SI Unit
a	Perturbed radius of the jet	m
Ca	Capillary Number $\left(\frac{\eta_e Q}{\gamma r^2}\right)$	-
c	Concentration of polymer solution	kg/L
De	Deborah Number $\left(\frac{\tau_p Q}{\pi r^3}, \frac{\tau_p}{\sqrt{\rho {r_0}^3/\gamma}}, \delta\tau_p\right)$	-
d	Jet diameter	m
$\tilde{d}$	Dimensionless Jet diameter $\left(\frac{d\eta_e K}{\gamma\varepsilon}\right)$	-
E	Applied electric field	V/m
E_z	Electric field in axial direction	V/m
$\tilde{E}$	Dimensionless applied electric field $\left(\frac{E\varepsilon}{(\eta_e K)^{1/2}}\right)$	-
Fr	Froude Number $\left(\frac{Q^2}{g\pi^2 r^5}\right)$	-

G	Shear modulus	Pa
h	Distance between nozzle-tip and collector	m
I	Electric current	A
k	Axial wave number	1/m
K	Electrical conductivity of polymer solution	S/m
m	Exponent	-
M_w	Weight average molecular weight	N
n	Azimuthal mode	1/radian
Oh	Ohnesorge Number $\left(\frac{\eta}{(\rho\gamma r_0)^{1/2}}\right)$	-
Pe	Electric Peclet Number $\left(\frac{2\bar{\varepsilon}Q}{\pi K r^3}\right)$	-
Q	Volumetric flow rate	m^3/s

$\tilde{Q}$	Dimensionless volumetric flow rate $\left(\frac{Q\eta_e{}^3K^2}{\gamma^3\varepsilon^2}\right)$	-
r_o	Internal radius of the nozzle	m
r	Jet radius	m
$\boldsymbol{r}$	Radius vector	m
Re	Reynolds Number $\left(\frac{2\rho Q}{r\eta_e}\right)$	-
t	Time	s
U_o	Electrical potential	V
V_c	Critical voltage	V
v	Free-stream velocity	m/s
$\boldsymbol{V}$	Velocity vector	m/s
z	Axial distance	m
$\tilde{z}$	Dimensionless axial distance $\left(\frac{z\eta_eK}{\gamma\varepsilon}\right)$	-
γ	Surface tension	N/m
δ	Growth rate	1/s

$\tilde{\delta}$	Dimensionless growth rate	-
ε	Dielectric constant (polymer solution)	F/m
$\bar{\varepsilon}$	Dielectric constant (air)	F/m
η	Dynamic Viscosity	Pa·s
η_e	Extensional viscosity	Pa·s
λ	Axial wavelength	m
υ	Kinematic viscosity	m^2/s
ρ	Density	kg/m^3
σ	Surface charge density	C/m^2
τ_p	Polymer relaxation time $\left(\frac{\eta}{G}\right)$	s
τ_γ	Rayleigh timescale $\left(\sqrt{\frac{\rho {r_0}^3}{\gamma}}\right)$	s

Chapter 1 Introduction

An experimental study of the flow regimes* pertaining to the electrospun jet and their characterization through relevant correlation formulae is performed. Instabilities and failure modes experienced by the electrospun jet are also analyzed. Methods for the effective control of electrospinning for the production of fibers are also proposed. In order to appreciate the scope and contributions of the present study pertaining to electrospinning, it will be helpful to review previous research work in this field. The study of electrospinning has a history of more than 100 years with the first patent obtained in 1900. Since then, a variety of experimental and theoretical studies has been performed. Numerous applications of electrospinning have been invented and studied. In Section 1.1, the evolution of electrospinning, its principle, and motivating factors governing the research in this field are discussed. The section also describes the diverse applications of electrospinning. Section 1.2 covers basic setup of electrospinning to help understand the theoretical analysis presented in section 1.3. To effectively use electrospinning in specific applications, a theoretical understanding of the electrospinning is essential. The theoretical understanding of electrospinning is broadly divided into three flow regimes. In Section 1.3, these three flow regimes are described in detail. Section 1.3 examines governing parameters for these three flow regimes. Later, these governing parameters will help to devise correlation formulae for these flow regimes. Chapter 1 concludes with the aim and scope, as well as an outline of the thesis in the sections 1.4 and 1.5, respectively.

**The term 'flow regimes' refers to different spatial regions along the electrospun jet.*

1.1 Motivating factors with historical Background

The unique and interesting properties of nanostructured materials have generated tremendous motivation among scientists and engineers to explore the possibilities of using them in a variety of industrial applications. The performances of such nanostructured materials/devices are expected to be superior as the quantum confinement of charge carriers in small dimensions gives rise to significant desirable properties [1-4]. One such area includes nanofiber-based technologies, which has grown exponentially considering the potential opportunities provided by nanofibers. The technologies usually employed for the production of nanofibers are the template method [5, 6], drawing [7, 8], phase separation [9], self-assembly [10, 11], and electrospinning [12, 13]. From the above-mentioned technologies, electrospinning have attracted tremendous interests due to its simplicity, low cost, and versatility in design with potential for industrial-scale processing of continuous nanofibers. In this thesis, electrospinning from a polymer drop is experimentally and theoretically analyzed for its control and optimization.

The fundamental principle underlying the fiber formation by electrospinning involves the application of a high externally applied electric field to a polymer solution/melt drop suspended from the tip of the nozzle. When an electric field is applied to the drop discharging from the tip of the nozzle, the surface of the liquid becomes electrically charged. If the electric field exceeds a critical value, the electrical forces overcome surface tension, and the droplet attains a conical shape. This conical shape is known as 'Taylor cone.' [14, 15] A straight electrically charged jet will erupt from the tip of the cone before it experiences electrical bending instability resulting in curling and spiraling of the electrospun jet in three-dimensional space. This curling and spiraling of the polymer jet is responsible for the

reduction of its diameter to submicron size. The electrospun jet dries and solidifies to fabricate fibers ranging from a few micrometers to submicron size. Later, these fibers are deposited on the grounded collector.

Cooley et al. [16] in their patent dated 1900 were the first to document the phenomenon of electrospinning. Electrospinning was considered the result of 'electrical disruption of the fluid' with the emphasis given to the requirement of adequately viscous polymer solution. A quarter-century later, Formhals [17-19] in a series of patents from 1930s to 1940s presented improved process and apparatus systems. His major contributions include improved apparatus systems allowing an appreciable degree of fiber alignment and production of multi-component nanofibrous webs. Later, in the 1960s, Taylor's contributions towards the understanding of the behavior of droplet placed in an electric field helped in understanding the fundamental physics behind the phenomenon [14, 15].

Baumgarten [20] analyzed the correlation between the fiber diameter with the viscosity of the polymer solution as well as the applied electric field. Larrondo et al. [21-23] spun fiber from thermoplastics polymer melt. They observed that the fiber diameter could be varied with the temperature of the polymer melt. Melt spinning in comparison to solution spinning has to be carried out at high temperatures, requires larger electric fields and an inert environment. Although these early works laid down the basic technique and understanding of the process, the phenomenon was aggressively explored in the last two decades due to the advances in nanotechnology. Major contributions include Yarin et al. [24, 25], Hohman et al. [26, 27] and Feng [28, 29]. They systematically documented the electrohydrodynamics pertaining to the electrospinning phenomenon. Material and process parameters were also analyzed to ascertain their relationship with the final fiber morphology [30-32].

Electrospinning is slowly but surely becoming a well-established technique in laboratories and industries that can fabricate continuous fibers with the diameter as small as a few nanometers. These nanofibers possess largest surface area to volume ratio among all cohesive porous materials making them the building block of a range of state-of-the-art nano-devices and technologies. Moreover, electrospinning can be applied to synthetic/natural polymers, ceramics, metal oxides and co-polymers, etc. These nanofibers can also be functionalized with desirable drugs, nanoparticles, and active agents, thus further cultivating the application space of electrospun nanofibers. The application space can be extended by controlling/optimizing the electrospinning phenomenon to obtain patterned nanostructures [33-35], yarns [36-38], multicomponent fibers [39-42]. As electrospun nanofibres are capable of achieving large surface area to volume ratio with desirable physical and chemical properties, it has been considered for a wide variety of applications, ranging from sensors [43, 44], antibacterial surfaces [45-47], scaffolds [48-50], photocatalyst [51-53], filters [54-56], solar cells [57, 58], electronics [59], skeletal muscle regeneration [60] to polarized luminescence [61]. Furthermore, electrospinning is being successfully scaled up for the fabrication of industrial products such as air and water filter [62].

1.2 The basic setup of the electrospinning

Figure 1.1 shows a schematic of the basic setup. The basic hardware components of the electrospinning process remain the same, as described in the initial patents. Nevertheless, modifications to the basic experimental setup have been made to control bending instability during electrospinning to be discussed in detail in the next section. The basic electrospinning system consists of a syringe pump, HVDC (High voltage direct current) supply and a grounded collector. The syringe pump connected to the syringe is employed to control the

volumetric flow rate of the polymer solution. An HVDC power supply is connected to the metallic nozzle, which connects to the syringe. From here on and hereafter, the term 'nozzle system' will comprise of the syringe pump with a syringe connected to the metallic nozzle as shown in Figure 1.1. The circuit is completed with a grounded or oppositely charged collector for the collection of resultant nanofibers.

A high electric field is applied to the pendent drop at the end of the nozzle. At a certain threshold electric field strength, depending on a number of factors, hemispherical shape of drop changes to a cone-shaped meniscus, known as Taylor cone [14, 15]. At some critical value of the applied electric field proposed by Taylor, the forces due to the applied electric field overcome the forces due to surface tension and results in jetting from the Taylor cone. The polymer jet, after traversing a straight-line motion for a certain distance, follows a curling and spiraling motion to be deposited on the collector. Collectors usually employed are rotating mandrel [63-66], a group of counter electrodes [67-69], and a flat-grounded surface [24]. The solvent, which may account for 80% of the solution weight, normally evaporates along the trajectory of the polymer jet resulting in dry nanofibers on the collector surface.

1.3 The electrostatics of electrospinning process

A vast majority of work related to electrospinning is of an experimental nature. Nevertheless, some theoretical studies have been proposed.

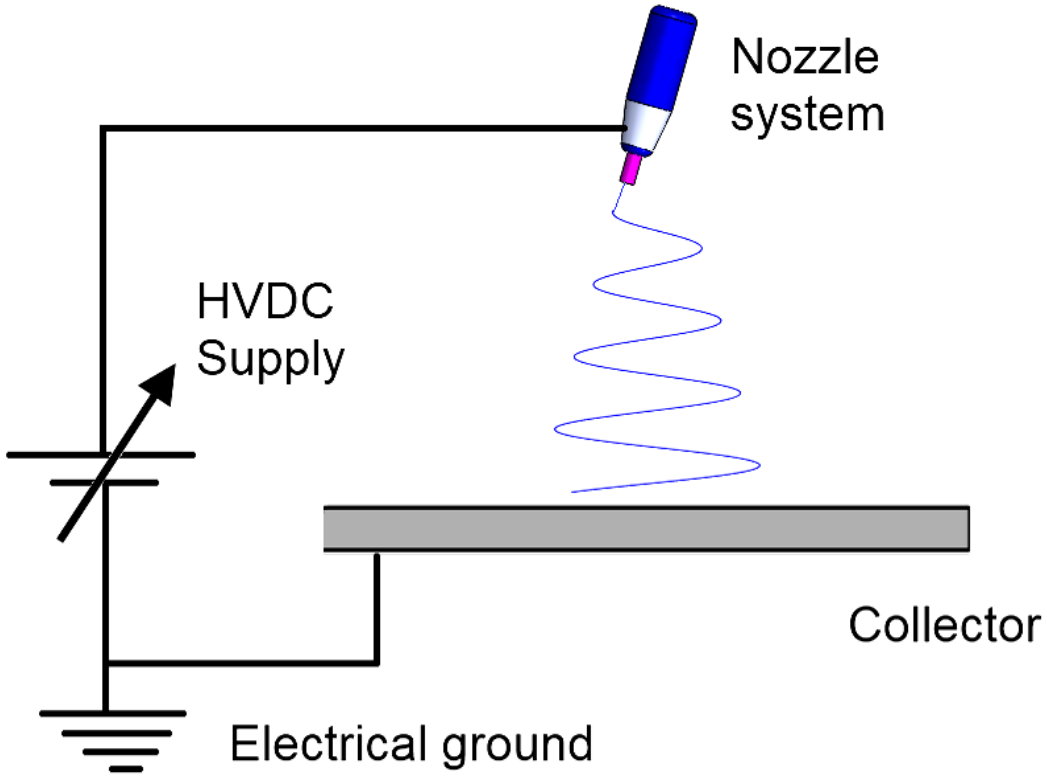

Figure 1.1 Schematic diagram of electrospinning setup. Not drawn to scale.

In this section, the aim is to compile models describing the electrospinning process to better understand the underlying phenomenon for the process control and optimization. Forces and parameters governing different flow regimes of the electrospun jet are analyzed. Detailed analysis pertaining to the flow regimes will be presented as and when required in the subsequent chapters of the thesis.

The electrostatics of the electrospinning process can be broadly divided into three flow regimes. These regimes include Taylor cone formation/jet initiation, straight section of the jet and bending/higher order instabilities of the electrospun jet. In terms of electrostatics, electrospinning closely follows the work on electrospraying [70-72]. The main difference is the application of viscoelastic polymer solution in case of electrospinning as opposed to low

molecular weight fluids in electrospraying. The viscoelastic polymer solution results in the extraction of the polymer fibers as opposed to the production of droplets in electrospraying.

1.3.1 Taylor cone formation and jet initiation

Firstly, the behavior of the charged droplet under the influence of high-applied electric field is examined. Rayleigh studied the instabilities of the electrically charged liquid droplet and calculated the maximum amount of charge (C_{max}) the droplet can maintain before exploding into a number of smaller droplets, which is given by Eq. (1.1) [73]:

$$C_{max} = 8\pi(\varepsilon\gamma {r_d}^3)^{1/2}, \tag{1.1}$$

where γ, r_d and ε are the surface tension, droplet radius and the dielectric constant of the liquid droplet, respectively. In the case of low molecular weight fluids, when the condition of maximum maintainable charge is surpassed, the electrical force results in axisymmetric fission of the droplet, giving rise to smaller highly charged sibling droplets. Zeleny [74, 75] noted that when the electric field strength is raised above a critical value, the shape of the charged droplet becomes unstable and a conical tip appears at the end of the charged droplet, from which a jet of charged sibling droplets is ejected. Later, Taylor identified the critical electric field required for the formation of the conical meniscus known as Taylor cone [14, 15]. He noted that a Newtonian viscous droplet existed in equilibrium in an electric field and took the form of a cone with half angle of 49.3^{o}. He observed that the governing forces are the forces due to surface tension that tend to minimize the surface area, and the forces due to normal electrical stress that tend to maximize the surface area. When the forces due to the normal electrical stress are large enough to surpass the forces due to surface tension, the droplet is deformed into a Taylor cone.

Taylor employed a glycerin solution in his analysis, which although viscous in nature, lacked the critical chain entanglement due to the low molecular weight of the glycerin molecules resulting in a jet of spherical droplets. This chain entanglement evident in the polymer solution is responsible for the stability of the polymer jet under the application of high electric fields. Later, Yarin et al. [25] analyzed the configuration of the polymer solution droplet in the presence of the electric field. He emphasized that Taylor cone's half-angle calculated at the tip of an infinite cone was self-similar in nature. However, a family of non-self-similar solutions exists for the hyperbolical shapes in equilibrium with their own electric field and surface tension force. The hyperboloidal liquid surface approaches a static shape that is very close to that of a cone with a rounded tip. It was shown that a hyperboloidal liquid surface develops a critical shape of a cone with a half angle of 33.5^{o}, rather than 49.3^{o}. Yarin et al. [25] also showed that the critical half angle did not depend on fluid properties as predicted by Taylor, since an increase in surface tension is always accompanied by an increase in the critical electric field. However, the sharpness of the cone will depend on the elastic and surface tension forces in viscoelastic fluids. As soon as the forces due to normal electrical stress overcome the surface tension forces, a fine charged jet is ejected from the Taylor cone. Taylor estimated the critical voltage at which the jet is initiated from the cone, which is given by the expression:

$$V_c^2 = 4\frac{h^2}{L_t^2}\pi\left(ln\frac{2L_t}{r_o} - \frac{3}{2}\right)(0.117\pi\gamma r_o\ ), \tag{1.2}$$

where V_c, the critical voltage, h, the capillary tube to collector distance, L_t and r_o are the length and radius of the capillary tube, respectively and the other symbols have their usual meaning. In the case of a polymer viscoelastic solution, the application of the critical voltage

results in a jet traversing a straight-line trajectory before undergoing higher-order instabilities.

1.3.2 Straight section of the electrospun jet

Firstly, we will study the assumptions and conservation laws employed in the analysis of the polymer slender jet originating from the Taylor cone. The polymer solution employed in electrospinning is usually assumed as 'leaky dielectric,' which implies that free charged ions are assumed to be on the surface of the jet [76]. Additionally, the jet radius decreases along the axial direction, and the axial velocity is uniform across the cross-section of the jet, and the process is steady in an Eulerian sense. Models employed for the straight section of the jet use conservation of electric charge, mass, linear momentum and electric field equation for the simplified one-dimensional analysis. The polymer behavior is modeled as Newtonian as well as viscoelastic by incorporating appropriate constitutive equation in the analysis.

Spivak et al. [77] were among the first researchers to propose a one-dimensional model for the straight section of the electrospun jet. The fluid behavior of the jet was represented by a Non-linear power law rheological constitutive equation. Nevertheless, the model did not incorporate the effect of normal electrostatic stress and viscous contributions to the jet momentum equation. The models pertaining to the straight section were improved by Yarin et al. [24, 25] and Hohman et al. [26, 27] following different approaches. Yarin et al. derived quasi-one-dimensional equations for the conservation of mass, momentum, and electrical charge describing the dynamics of the electrospun jet, as follows:

$$f\phi = f_0\phi_0, \tag{1.3}$$

$$\rho\phi_0 f_0 \frac{\partial \boldsymbol{V}}{\partial t} = \boldsymbol{j}\frac{\partial P}{\partial s} + \phi|i|P\boldsymbol{n} - \rho g\phi_0 f_0 \boldsymbol{i} + \phi|i| \times \left(\pi r\gamma - e^2 ln\frac{L_e}{r}\right)\boldsymbol{n} - \phi e\frac{U_0}{h}\boldsymbol{i}, \tag{1.4}$$

$$e\phi = e_0\phi_0, \tag{1.5}$$

where $'s'$ is the Lagrangian parameter 'frozen' into the jet elements, e is the charge per unit length and L_e *is* the length of a certain element of the jet. The $\boldsymbol{j}$ and $\boldsymbol{n}$ are respectively the unit vectors in the tangential and the normal direction of the jet profile, whereas $\boldsymbol{i}$ is the unit vector parallel to the externally applied electric field. Equation (1.3) represents conservation of mass, where ϕ is the geometrical stretching ratio such that $\phi ds = d\Xi$, Ξ is the arc length and $f = \pi r^2$ is the cross-sectional area. The subscript zero denotes the parameter values at the time $t = 0$. Equation (1.4) is the momentum balance equation with ρ being the liquid density, $\boldsymbol{V}$, its velocity vector, P, the longitudinal force in the jet cross-section and g, the acceleration due to gravity. U_o is the value of electrical potential at the jet's origin and h is the distance between the nozzle-tip and the collecting plate. Equation (1.5) represents the conservation of charges. In Cartesian coordinates, the kinematics relations are given as, $\partial \boldsymbol{r}/\partial t = \boldsymbol{V}$, where, $\boldsymbol{r}$ is the radius vector of a point on the axis of the jet. Substituting the kinematic relations in the Equation (1.4), a system of scalar equations was obtained. The simplest version of the Upper-convected Maxwell model of viscoelasticity was assumed to describe the behavior of an electrospun jet.

The discretized system of the equations allowed Yarin et al. to obtain the jet configuration in space at any particular instance of time. Comparisons were made between

experimental and theoretical results for a 6 wt% Poly (ethylene oxide) solution dissolved in 60/40 v/v water/ethanol mixture. The applied electric field strength was 100 kV/m. The predicted motion of the jet was found to be in good agreement with the experimental data until about 3 ms after jet initiation.

On the other hand, Hohman et al. [26, 27] modeled the electrospun jet on the assumption that the instabilities occurred on a length scale much longer than the jet radius. As a result, the jet was represented as a long, slender object. Feng [28, 29] simplified the Hohman et al. [26, 27]'s formulation by making it insensitive to the initial charge density, except inside a tiny 'boundary layer' at the nozzle-end. He also accounted for the nonlinear viscoelasticity by incorporating Giesekus constitutive equation into the governing equations. The dimensionless governing equations for the unknown parameters $r,\ v,\ E, \sigma,\ \tau_{pzz}$ and τ_{prr} were given by the Equation (1.6) - (1.11). The characteristic quantities used to non-dimensionalize unknown parameters were r_0, $v_0 = \frac{Q}{\left(\pi r_0^2\right)}$, $E_0 = \frac{I}{\left(\pi r_0^2 K\right)}$, $\sigma_0 = \bar{\varepsilon} E_0, \tau_0 = \frac{\eta v_0}{r_0}$, with $\eta = \eta_s + \eta_p$, where, η_s and η_p are viscosities due to the solvent and the polymer, respectively. Q is the volumetric flow rate, I is current flowing through the jet and r_0 is the internal radius of nozzle. The resultant dimensionless governing equations were:

$$\pi \tilde{r}^2 \tilde{v} = 1, \tag{1.6}$$

$$\tilde{r}^2 \tilde{E} + Pe \tilde{r} \tilde{v} \tilde{\sigma} = 1, \tag{1.7}$$

$$\tilde{v}\tilde{v}' = \frac{1}{Fr} + \frac{3\left(1 - r_\eta\right)}{Re}\left(\frac{\left(\tilde{r}^2 \tilde{v}'\right)'}{\tilde{r}^2}\right) + \frac{T_p'}{Re\left(\tilde{r}^2\right)} + \frac{1}{We}\frac{\tilde{r}'}{\tilde{r}^2} + \Re\left(\tilde{\sigma}\tilde{\sigma}' + \beta \tilde{E}\tilde{E}' + \frac{2\tilde{\sigma}\tilde{E}}{\tilde{r}}\right), \tag{1.8}$$

$$\tilde{E}_z = \tilde{E} - \ln\chi\left(\left(\tilde{\sigma}\tilde{r}\right)' - \frac{\beta}{2}\left(\tilde{E}_z\tilde{r}^2\right)''\right), \tag{1.9}$$

$$\tilde{\tau}_{prr} + De\left(\tilde{v}\tilde{\tau}'_{prr} + \tilde{v}'\tilde{\tau}_{prr}\right) + \varsigma\frac{De}{r_\eta}\tilde{\tau}^2_{prr} = -r_\eta\tilde{v}', \tag{1.10}$$

$$\tilde{\tau}_{pzz} + De\left(\tilde{v}\tilde{\tau}'_{pzz} - 2\tilde{v}'\tilde{\tau}_{pzz}\right) + \varsigma\frac{De}{r_\eta}\tilde{\tau}^2_{prr} = 2r_\eta\tilde{v}', \tag{1.11}$$

where $\tilde{r}$, $\tilde{v}$, $\tilde{E}$, $\tilde{\sigma}$, $\tilde{\tau}_{pzz}$ and $\tilde{\tau}_{prr}$ represent dimensionless radius, velocity, electric field, surface charge density, polymer stress in the axial and radial directions, respectively. From here on and hereafter, tilded quantities will represent a dimensionless quantity of their respective dimensional counterpart. The dimensionless groups were given as $\tilde{T}_p = r^2\left(\tau_{pzz} - \tau_{prr}\right)$, $Fr = \frac{v_0^2}{gr_0}$, $Pe = \frac{2\bar{\varepsilon}v_0}{Kr_0}$, $Re = \frac{\rho v_0 r_0}{\eta}$, $We = \frac{\rho v_0^2 r_0}{\gamma}$, $\Re = \frac{\bar{\varepsilon}E_0^2}{\rho v_0^2}$, $De = \frac{\tau_p v_0}{r_0}$, $r_\eta = \frac{\eta_p}{\eta}$, $\beta = \left(\frac{\varepsilon}{\bar{\varepsilon}}\right) - 1$, and $\chi = \frac{L}{r_0}$ where L is the length of the straight section of jet, ς is the mobility factor, τ_p is the polymer relaxation time, $\bar{\varepsilon}$ is the dielectric constant of air, whereas τ_{pzz} and τ_{prr} are polymer stress in the axial and radial directions, respectively. The other symbols include $\rho, \gamma, K, \varepsilon$ and η, i.e. density, surface tension, electrical conductivity, dielectric constant, and viscosity of the polymer solution, respectively. Later, the system of second and first-order ordinary differential equations was solved numerically to obtain the jet characteristics.

Feng [28, 29] documented that strain hardening promoted jet thinning at the beginning but suppressed it further downstream to produce thicker jet. In addition, the Giesekus model also predicted earlier onset of strain hardening at higher strain rates. Though complete comparisons with experiments were not performed, the theory appeared to predict

jet thinning on the right order of magnitude. The electrospun jet, after traversing a straight-line motion, experiences instabilities depending upon operating parameters, which will be discussed in the next section.

1.3.3 Instabilities experienced by the electrospun jet

As the jet ejects from the tip of the Taylor cone, it follows a straight-line path for a certain distance depending upon the process and material parameters before experiencing electrical bending instability. It is worth mentioning that before the advent of high-speed imaging, it was believed that the jet splays into multiple jets [78]. Later, high-speed imaging demonstrated that the jet curls so fast giving the impression of multiple jets but in reality, is a single jet, curling and spiraling in 3D space [79]. This curling and spiraling motion of the jet is considered responsible for the reduction of jet diameter on the order of nanometers. Nevertheless, it is possible to suppress curling and spiraling motion of the jet in near-field electrospinning to produce microfibers [80].

During its trajectory, the jet can experience a number of instabilities depending upon process and material parameters. The bending instability normally realized during electrospinning is one of the several possible instabilities that may occur in an electrified liquid jet [27]. The additional instabilities experienced by an electrospun jet include the capillary instability responsible for the breakup of the jet into droplets or non-uniform morphologies [73]. As mentioned, bending instability during electrospinning is the reason for the massive stretching of the polymer jet and the continuous decrease of the jet diameter [27]. Yarin et al. [24] considered this electrically driven bending instability of an electrospun jet as the particular case of the general Earnshaw theorem in electrostatics. The theorem states that it is impossible to create a stable structure in which the elements interact only by

Coulomb's law. The result of the phenomenon will be a lateral force component that will cause the jet to deviate from its original initiated path into a curling and spiraling trajectory.

Hohman et al. [27] and Yarin et al. [24] performed a linear stability analysis to better understand the phenomenon of bending instability of the electrospun jet. Hohman et al. [27] predicted three different types of instabilities, two of which were axisymmetric whereas the third was non-axisymmetric in nature. The first axisymmetric mode was stated to be associated with the capillary instability, which is dominated by surface tension. The other two axisymmetric and non-axisymmetric conducting modes were dominated by electrical stress. These conducting modes were largely sensitive to fluid conductivity and insensitive to the surface tension at high-applied electric field strengths. The conducting mode that will dominate depends on both the surface charge density and the radius of the jet as it thins away from the tip of the nozzle to the collector surface.

When the electric field is further increased above the value required for producing electrospinning, higher-order instability is observed, known as branching [81]. Branching allows a means of rapidly increasing surface area to accommodate local concentrations of charges. It was noted that the Ohnesorge number was higher than the imposed limit ($Oh \gg 1$)**,** which implies that the process requires higher viscous stresses than usually employed for typical electrospinning. Nevertheless, the growth of branches on the surface of the jet is directly proportional to the competition between radial electrostatic stress and surface tension. Additional detailed analysis pertaining to the flow regimes will be presented in the subsequent chapters of the thesis.

It is clear from the analysis that the characteristics of the polymer jet can be obtained by proper control of the operating parameters, and will be systematically discussed in

subsequent chapters of the thesis. These operating parameters include volumetric flow rate, applied electric field, concentration (viscosity), density, dielectric constant, polymer relaxation time, conductivity, and the surface tension of the polymer solution. Comprehensive predictive models comprising all the pertinent operating parameters will be developed and analyzed in the subsequent chapters.

1.4 Aim and scope of the thesis

The thesis deals with a detailed study of electrospinning, as well as development of the techniques for the effective control of electrospinning. The thesis includes both experimental techniques and a theoretical understanding of electrospinning.

- Flow regimes such as Taylor cone formation/jet initiation, straight section of the jet and bending/higher-order instabilities experienced by the jet along its trajectory are systematically analyzed.
- Dimensional analysis has been performed to identify the salient dimensionless parameters, which govern the characteristics of the Taylor cone and the straight section of the jet. Correlation formulae presented in terms of the salient dimensionless parameters allow the jet characteristics to be correlated with the operating parameters.
- Instabilities and failure modes experienced by the electrospun jet are analyzed. An imaging system was designed to capture images at different time instances to characterize bending instability. These time-resolved images enabled the effects of the salient operating parameters to be systematically investigated. The parameters studied include wavelength, growth rate and the phase velocity.

- The failure modes of the electrospun jet during bending instability have also been investigated.
- A linear stability analysis of the electrified jet incorporating non-Newtonian effects has been performed to characterize higher-order instability. The linear stability analysis yields the axial wavelength corresponding to the highest order azimuthal mode. Subsequently, the axial wavelength is compared with the experimentally determined inter-undulation distance. An extensive analysis has been performed to reconcile the differences between the experimental and theoretical results.
- Techniques for the effective control of electrospinning have been proposed. In the first technique, a pulsed laser is focused onto the interior of the drop close to the liquid-air interface to overcome surface tension and produce an electrified jet. This approach can reduce the required applied electric field to half its value necessary for conventional electrospinning. Another technique proposed yields regular-sized microfibers through near-field electrospinning. Mass production of fibers can be rendered feasible using these technologies.

It is anticipated that the research work presented in this thesis will help in the control and optimization of the electrospinning and therefore will help in its utilization in nanofiber based mass-production techniques.

1.5 Outline of the thesis

The research work in the thesis is divided into 7 chapters, following chapter 1 'Introduction.' The outline of the subsequent chapters is presented as follows: Chapters 2 to 4 will deal with dimensional analysis of the Taylor cone and the straight section of the electrospun jet.

Chapter 2 covers aspects of the Taylor cone with a brief overview of the solution properties and electrostatics of the electrospinning phenomenon. A 'correlation formula' to predict the radius at the apex of the Taylor cone against the operating parameters is presented. Similarly, in Chapter 3, a 'correlation formula' to predict the radius at different locations along the straight section of the electrospun jet against the operating parameters is proposed. Then, in Chapter 4, a 'correlation formula' to predict the length of the straight section of the electrospun jet before the initiation of bending instability against the operating parameters is presented.

In Chapter 4, we also present a detailed study of the bending instability experienced by the electrospun jet. An imaging system is designed to obtain time-resolved images pertaining to bending instability to characterize it against the operating parameters. The parameters calculated in order to characterize bending instability include wavelength, growth rate as well as their phase velocity. The failure modes of an electrospun jets during bending instability are also investigated. Following that, Chapter 5 focuses on a higher-order instability known as branching of the electrospun jet. Chapter 5 elucidates the modeling of branches of the electrospun jet. The nonlinear rheological behavior of the polymeric fluid is incorporated in the formulation for the first time. Detailed derivations of the governing equations pertaining to instability experienced by the jet are performed. Comparison is made between the inter-undulation distances obtained experimentally with the theoretical model. The analysis also measures the effect of the relevant dimensionless parameters on the inter-undulation distance. The validity of the theoretical model is checked with the help of experimental data.

Lastly, Chapter 6 considers techniques for the control of electrospinning. In one of these techniques, a pulsed laser is focused inside the drop close to the liquid surface to overcome surface tension and produce an electrified jet. Another technique proposed yields regular-sized microfibers through near-field electrospinning. In Chapter 7, the investigation is summarized by answering the questions pertaining to the research aims and objectives.

Chapter 2 Taylor cone formation and jet initiation

2.1 Introduction

This chapter covers aspects of the initiation of the electrospun jet with a brief overview of the solution properties and electrostatics of the electrospinning phenomenon. In section 2.2, the experimental setup and configurations employed for electrospinning are analyzed. Material properties of polymer solutions employed in electrospinning are studied in section 2.3. Sections 2.4 and 2.5 study Taylor cone formation/jet initiation and the analysis of jet radius at the apex of the Taylor cone, respectively. In the section 2.6, dimensional analysis is performed to obtain pertinent parameters to scheme relevant 'correlation formula.' Three dimensionless parameters are found to govern the jet characteristics at the apex of the Taylor cone. These dimensionless parameters include dimensionless flow rate, electric field, and diameter of the electrospun jet. The proposed correlation formula will help envision jet characteristics to control and optimize the electrospinning phenomenon. The other relevant correlation formulae pertaining to the straight section will be covered in chapters 3 and 4. Finally, results are summarized in section 2.7.

2.2 Experimental details

2.2.1 Experimental setup

Two electrospinning setups were designed for the experiments. These are shown in Figure 2.1. One of them is a Point-plate setup shown in Figure 2.1 (a). The 'Point' in the Point-plate setup is represented by a nozzle, whereas, the 'plate' corresponds to the collector. The collector is an aluminum disc of 62 mm diameter and 10 mm thickness. The metallic nozzle was connected to a syringe pump (Model: SP200IZ, World Precision Instruments, U.S.A.)

which was used for controlling the volumetric flow rate of the polymer solution. The outer diameter of the metallic nozzle used for the production of electrospun nanofibers was 1.24 mm (inner diameter = 1 mm). For selected experimental cases, glass nozzles with diameter ranging from 5 to 200 μm were employed. The distance between the nozzle-tip and the collector surface was on the order of 100 mm. For near-field electrospinning, nozzle-tip to collector distance was on the order of 10 mm. The electrospinning setup shown in Figure 2.1 (a) was encased within an acrylic box of dimensions 160×130×130 mm^3 to avoid any interaction with the exterior environment. Experiments were conducted at room temperature, approximately 25 °C.

Electrospinning started when a sufficiently high electric field was applied to the metallic nozzle containing the polymer solution. Subsequently, the resultant electrospun fibers were collected on the electrically grounded metallic collector as realized in Figure 2.2. The diameters of the electrospun nanofibers shown in Figure 2.2 were found to range from 350 nm to 1.5 μm for 2.5 wt% PEO (M_w = 400,000) aqueous solution. The average fiber diameter was found to be 640 nm.

Electrospinning is extremely sensitive to process parameters such as flow rate, applied voltage, and nozzle-tip to grounded collector distance. For the purposes of this study, most of the process parameters remained in the same general range. The applied voltage varied from 4 to 20 KV. The volumetric flow rates for the experiments varied from 0.01 to 0.3 ml/min for the majority of the experimental cases.

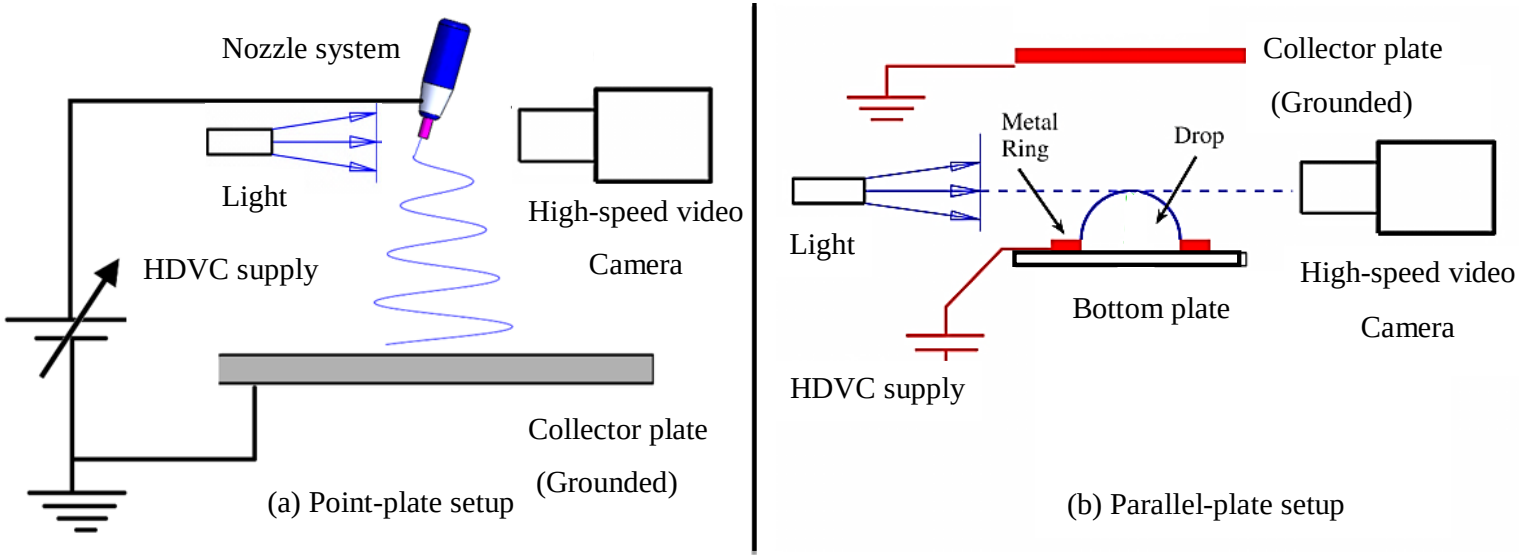

Figure 2.1 Schematic diagram of electrospinning setup, (a) Point-plate setup, and (b) Parallel-plate setup. Not drawn to scale.

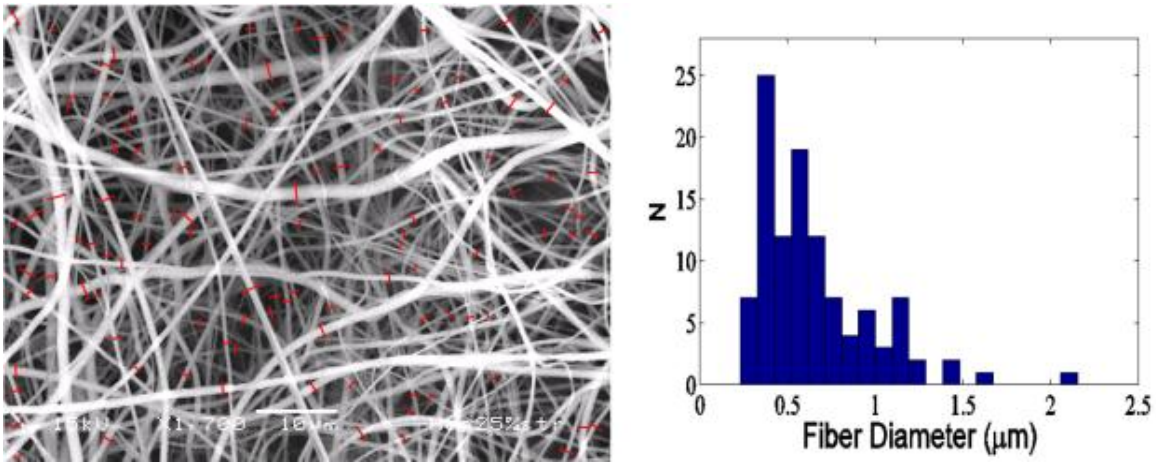

Figure 2.2 SEM image of 2.5 wt% PEO (M_w = 400,000) dissolved in distilled water electrospun at electric field strength (flow rate) of 45 kV/m (0.03 ml/min). The diameter of electrospun fiber was found to range from 350 nm to 1.5 μm.

Researchers have analyzed applied electric voltage (U_o) and the nozzle-tip to collector distance (h) as independent parameters. Nevertheless, changing either voltage or nozzle-tip to collector distance changes the externally applied electric field (U_o/h). This implies that externally applied field is the relevant process parameter chosen in the current analysis. For a particular applied electric field strength, the process was sustained for several minutes to obtain a steady-state condition.

The electrospinning setup was located on a levitator to raise or lower its height, as and when required. This movement of the electrospinning setup in the vertical direction helped to capture the complete trajectory of the electrospun jet. The images were obtained with the help of a High-speed camera (Model: Photron FASTCAM-Ultima APX-RS**)** connected to a long distance microscopic lens. The frame rates used for the analysis ranged from 5,000 to 200,000 fps. In some of the experimental cases, images were obtained with the help of a still camera (Model: Nikon D80) connected to a long distance microscopic lens.

The second setup shown in Figure 2.1 (b) depicts the Parallel plate arrangement. Two aluminum discs were arranged in a parallel configuration. The diameter of the aluminum disc was 6 mm (thickness = 2 mm). One of the parallel plates was connected to the High-voltage power supply, whereas the other plate was grounded. The distance between the parallel plates was about 20 mm. The high voltage was applied to the polymer drop placed on the bottom plate. The Taylor cone and subsequently, the jet was ejected, when the forces due to the electric field were able to surpass those arising from surface tension.

The setup shown in Figure 2.1 (b) was employed for the Taylor cone analysis in section 2.4 and in laser-induced electrospinning in section 6.3. For all other experimental analysis, the Point-plate setup shown in Figure 2.1 (a) was employed. This is because the Point-plate setup requires low applied electric fields in comparison to the Parallel plate arrangement to produce a spinning phenomenon, thus making it a widely employed setup for electrospinning [24]. It is noted that for the same externally applied electric field, the Point-plate setup produces higher electrostatic forces near the vicinity of the nozzle [82]. These higher electrostatic forces near the vicinity of the nozzle help to overcome surface tension and produce jetting at relatively low electric fields in comparison to the Parallel plate arrangement. The parallel plate arrangement was employed when the uniform electric field is required, as in sections 2.4 and 6.3.

2.2.2 Material preparation

The polymer solutions employed in the electrospinning range from 0.125 to 6 wt% Poly (ethylene oxide) (PEO) (M_w = 400,000, 900,000 and 2,000,000) dissolved in distilled water. Ethanol was also employed as a partial a solvent in some of the experimental studies. The

ethanol employed was 99% pure denatured in 5% methanol. The typical concentrations of polymer solution ranged from 1 to 40 wt% depending on the specific polymer-solvent system.

PEO-water solution system was selected as the test system due to the low volatility of water at room temperature, resulting in relatively low evaporation rates as compared to the highly volatile solvents employed in electrospinning. This solution system prevented the occurrence of undesirable outcomes such as polymer skins, the growth of the Taylor cone with time and eventual blockage of the nozzle. This allowed steady-state conditions to be achieved for longer durations of time. Thus, this allowed for a large 'processing window' as compared to systems such as nylon 6, 6-formic acid, which can only be electrospun for a limited range of process parameters.

2.3 Material properties of PEO-water/ethanol solution system

In the thesis, experimental data are systematically analyzed against operating parameters. Process parameters such as the applied electric field and volumetric flow rate were collected through experiments for stable jetting from the polymer drop. In this section, all the relevant material parameters of the polymer solution used are compiled. These material parameters include density, viscosity, conductivity, dielectric constant, surface tension, and polymer relaxation time of the polymer solution. Before collecting the solution properties of the PEO-water/ethanol solution system, it is worthwhile to calculate the Knudsen number, which defines the transition from micro to nanoscale. The Knudsen number defines the upper limit where the continuum hypothesis is still valid.

$$K_n = \Gamma / L_a. \tag{2.1}$$

L_a is a representative physical length scale, i.e., the diameter of the electrospun fibers, which was found to be 640 nm for the condition shown in Figure 2.2. Γ is the mean free path, which is on the order of 5-10 nm for liquids. The value of the Knudsen number is 0.015. The low value of the Knudsen number implies that the continuum hypothesis is valid for the flow regimes pertaining to the electrospun jet. It is well known that a convenient way to characterize a polymer in solution at low concentrations is to measure the viscosity with the help of the viscosity function.

$$\eta = (\eta_{sp} + 1)\eta_s, \tag{2.2}$$

where,

$$\eta_{sp} = c[\eta_m] + K_h[\eta_m]^2 c^2, \tag{2.3}$$

$$\eta_m = K_0 M_{w.}^a \tag{2.4}$$

Equation (2.2) was used to calculate the viscosity (η) for the dilute polymer solution employed during the experimental analysis. The symbols include η_{sp}, the specific viscosity, η_s, the viscosity of the pure solvent, and η_m, the intrinsic viscosity of the solution. Other symbols are c, concentration of the polymer solution and K_h, the Huggins viscosity coefficient. The Huggins viscosity coefficient is taken to be 0.4 for water as a solvent.

Here, the intrinsic viscosity is defined by the Mark-Houwink equation (Equation (2.4)). In Equation (2.4), K_0 and a are constants for a given polymer solvent system. For the molecular weight employed during the analysis M_w = 400,000 to 2,000,000, $K_0 = 12.58 \times 10^{-3}$ ml/g and $a = 0.78$ for distilled water [84]. The intrinsic viscosity obtained from Equation (2.4) is dependent on the solvent and the molecular weight of the polymer employed. Nevertheless, it is independent of the polymer concentration. The calculated value

of intrinsic viscosity from Equation (2.4) was used in Equation (2.3) to obtain specific viscosity. Then, the specific viscosity enabled us to calculate concentration dependent dilute solution viscosity (Equation (2.2)). It is noted that the assumption of dilute polymer solution is valid until the given condition is satisfied $\left(c \times \eta_m < o(1)\right)$ [85].

For 0.5 to 2 wt% PEO (M_w = 400,000) dilute solution, viscosity is calculated from Equation (2.2). Data from Helgeson et al. [86] was employed to linearly extrapolate/interpolate the values of viscosity for 1.5 to 6 wt% (M_w = 900,000). The values of viscosity were extrapolated/interpolated against the concentration of the polymer solution. Similarly, viscosity for 0.75 to 2 wt% (M_w = 2,000,000) were obtained against concentration from Arnolds et al. [87].

In case of dilute polymer solutions, surface tension can be assumed to be close to that of solvent, i.e. water. The values of surface tension for 1.5 to 6 wt% (M_w = 900,000) were linearly extrapolated/interpolated against the concentration of the polymer solution from Fong et al. [88]. Similarly, surface tension for 0.75 to 2 wt% (M_w = 2,000,000) were obtained against concentration from Arnolds et al. [87]. The value of density for 0.5 to 6 wt% (M_w = 400,000, 900,000 and 2,000,000) is assumed to be 1000 kg/m^3 [24].

For 0.5 to 2 wt% PEO (M_w = 400,000) dilute polymer solutions, polymer relaxation time is calculated from Fong et al. [88]. Data from Helgeson et al. [86] was employed to extrapolate/interpolate the values of polymer relaxation time for 1.5 to 6 wt% (M_w = 900,000). Polymer relaxation time for 0.75 to 2 wt% (M_w = 2,000,000) were obtained against concentration from Arnolds et al. [87].

For 0.5 to 2 wt% PEO (M_w = 400,000) dilute polymer solutions, electrical conductivity were calculated from Fong et al. [88]. Data from Helgeson et al. [86] was employed to extrapolate/interpolate the values of electrical conductivity for 1.5 to 6 wt% (M_w = 900,000). The values of electrical conductivity of 0.75 to 2 wt% (M_w = 2,000,000) were obtained against concentration from Theron et al. [31].

The estimates of relative permittivity for the polymer solutions are 60 for 0.5 to 2 wt% PEO (M_w = 400,000), 80 for 1.5 to 6 wt% (M_w = 900,000) and 100 for 0.75 to 2 wt% (M_w = 2,000,000) [31]. The physical properties for 1 wt% (M_w = 2,000,000) dissolved in a water/ethanol mixture by volume were extrapolated from PEO-water/ethanol systems [31, 88]. The values of the above-mentioned material parameters compiled in Table 2.1 were incorporated in the analysis performed in the subsequent sections.

Table 2.1 Material parameters of different concentration of polymer solutions employed during the analysis.

Concentrations (w%)	Viscosity Pa·s	Surface tension 10^{-3} N/m	Electrical conductivity $(\text{ohm-m})^{-1}$	Polymer Relaxation time (sec)
0.5 (M_w = 400,000)	0.00332	77	$9.5\text{X}10^{-6}$	$4\text{X}10^{-7}$
1.0	0.00736	77	$1.9\text{X}10^{-5}$	$7\text{X}10^{-7}$
1.5	0.0131	75	$2.6\text{X}10^{-5}$	$1.2\text{X}10^{-6}$
2.0	0.0205	70	$3.5\ \text{X}10^{-5}$	$1.5\text{X}10^{-6}$
0.75 (M_w = 2000,000)	0.10	68	$9\text{X}10^{-5}$	0.020

1.0	0.22	65.7	$1X10^{-4}$	0.024
1.5	1.09	62.8	$7X10^{-4}$	0.030

2.4 Taylor cone formation/jet initiation

The phenomenon of formation of Taylor cone and the initiation of the jet is depicted in Figure 2.3. Figure 2.3 depicts the experimental study of a polymer drop placed in a parallel plate system shown in Figure 2.1 (b). The parallel plate system was able to achieve uniform electric field between the metallic plates resulting in a uniform Taylor cone profile, which was not the case for the point-plate system shown in Figure 2.1 (a). The phenomenon of the emergence of electrified jet starts with the application of an electric field to a spherical polymer droplet placed on the bottom plate of the parallel plate system. The images obtained were inverted due to the microscopic lens. The polymer employed was 1 wt% PEO (M_w = 2,000,000) with 0.005 wt% NaCl dissolved in distilled water. The complete cycle of the jet formation can be divided into three phases, namely, Taylor cone formation, jet initiation, and then relaxation of the polymer drop.

Initially, before the application of electrostatic forces, the polymer droplet was in equilibrium with the balance of gravitational and surface tension forces. As the applied voltage was increased in steps of 0.2 kV, the curvature at the tip of the polymer drop increases, which subsequently results in the formation of a conical meniscus known as Taylor cone as shown in Figure 2.3 (a) [14]. The depicted frames were 2.14 ms apart. The maximum applied electric field occurred at the tip of the Taylor cone due to its large curvature. This implies that the tip of Taylor cone is the most likely location to surpass

surface tension and results in the formation of a polymer jet as shown in Figure 2.3 (b). The depicted frames were 0.357 ms apart. The applied electric field for the jet initiation was 1055 kV/m. The half angle (θ) of the Taylor cone was close to 49^{o} at initiation of the jet, which was found to be close to that observed in the literature [14, 15]. This is reasonable as low viscosity liquid was applied in the current analysis. Nevertheless, the sharpness of the cone will vary with the variation in the viscoelastic behavior of the polymer solution as noted by Yarin et al. [25].

Later, when the majority of the charged ions collected at the tip of the Taylor cone are emitted with the jet, the drop settles down with a lower curvature at its tip. The excess depletion of charged ions is considered responsible for the reduction of curvature at the tip of static polymer droplet employed during the analysis. However, it is possible to maintain a stable Taylor cone profile for dynamic fluid flow by the continuous replenishment of the charged ions.

2.5 Analysis of the radius along the trajectory of the electrospun jet

The focus of the experiments was the region where the jet emanates from the polymer drop. The experimental setup shown in Figure 2.1(a) was employed for the analysis. Images were obtained with the help of a still camera with resolution as high as 0.3 µm/pixel. Figure 2.4 shows a close-up image of this particular region taken at the maximum magnification. Fresnel diffraction patterns were observed along the jet, showing that any further increase in the magnification would not be helpful. Most images were taken at a slightly lower magnification, but sufficient to resolve variations on the order of one micrometer

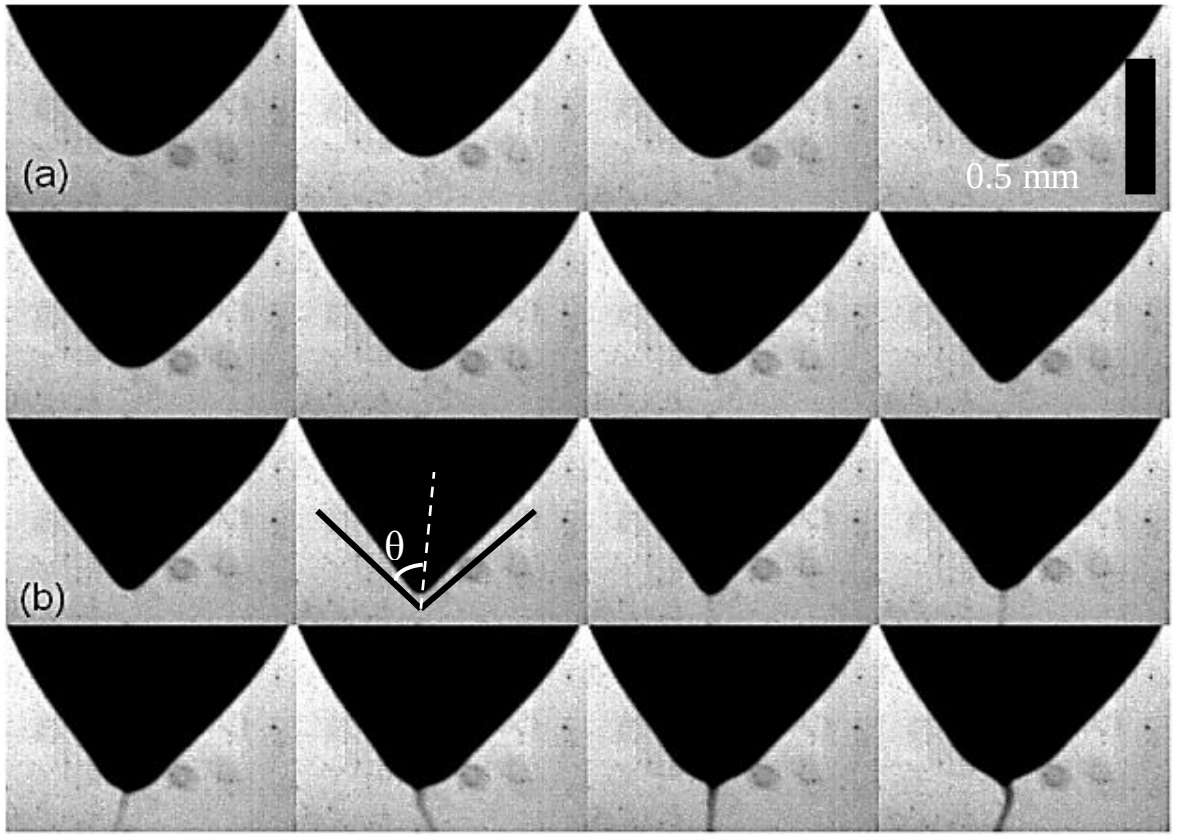

Figure 2.3 Taylor cone formation and jet initiation, (a) conversion from spherical to a conical meniscus, the frames are 2.14 ms apart, (b) jet initiation from the tip of the cone; the frames are 0.357 ms apart. Figure depicts the instance of a drop placed in a parallel plate system. The applied electric field for jet initiation was 1055 V/m. The polymer employed, was 1 wt% PEO (M_w = 2,000,000) with 0.005 wt% NaCl dissolved in distilled water. The images obtained were inverted due to the microscopic lens.

Figure 2.4 clearly shows that the jet thins from the apex of the Taylor cone along its trajectory depicting an increase in stretching of the jet. This is well known from the earlier studies [27, 28, 89], but has not been accurately measured. Therefore, a systematic study was performed to precisely correlate the jet radius with the operating parameters to devise relevant correlation formulae.

A set of images was obtained for a particular concentration of the polymer solution at progressively increasing electric field strengths. For a given volumetric flow rate, the applied electric field was varied until a stable jetting condition was maintained. Maintaining this stable jetting condition turned out to be a nontrivial task, as precise matching of the process parameters (applied electric field and flow rate) had to be achieved for the given material parameters. Subsequently, these images were digitized using a code written in Matlab®, which extracts the surface shape using image thresholding. An image of the nozzle was taken for each set of images, which served as a reference image. Later, the reference image was used for converting pixel data available from the digitized images into metric units.

Subsequently, the data was averaged over 30 images for each set of operating conditions to ensure measurement precision. The repeatability was also checked by performing experiments at a regular interval of time in the same controlled laboratory environment. The variation in the absolute value of the jet radius was found to be about 8% of all the experimental cases. The data obtained gave a systematic understanding of the variation in jet radius with respect to the operating parameters.

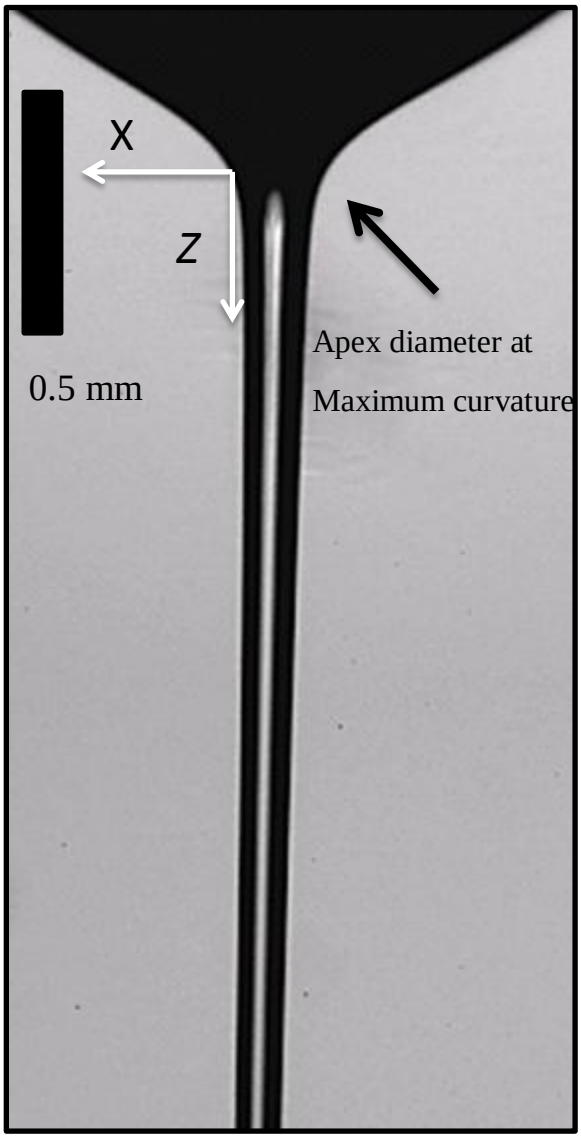

Figure 2.4 Close-up of the electrified jet using large magnification for 0.75 wt% PEO (M_w = 2,000,000) dissolved in distilled water electrospun at applied electric field strength (flow rate) of 82.17 kV/m (0.11 ml/min). The apex diameter was obtained at the point of maximum curvature, which also corresponds to z = 0.

2.6 Dimensional analysis pertaining to the diameter at the apex of Taylor cone

One of the major issues with electrospinning is the lack of functional models that can link operating parameters to the jet characteristics. The majority of the models proposed are only applicable for a specific polymer-solvent system. In view of the shortcomings, a group of

correlation formulae is proposed in Chapters 2-4, which will be helpful to predict the jet characteristics against the operating parameters for a variety of polymer-solvent systems. These jet characteristics include the dimensionless jet diameter $(\tilde{d})$ at the apex of the Taylor cone, dimensionless jet diameter at different locations along the jet's straight section, as well as dimensionless length of the straight section of the jet $(\widetilde{Z_{\text{in}}})$.

During the experimental analysis, radius profiles from the apex of the Taylor cone along the jet's trajectory were obtained for a wide range of operating parameters. A detailed analysis of these radius profiles will be discussed in Chapter 3. For the current analysis, we will work with the diameter ($2r$) at the apex of the Taylor cone. The apex diameter was obtained at the maximum curvature as depicted in Figure 2.4 for the operating parameters. Later, these diameters were employed in the dimensional analysis to study their dependence on the process as well as material parameters. The process and material parameters chosen are the usual parameters employed for the scaling analysis pertaining to the Taylor cone [90-93]. The process parameters for the analysis include Q and E, volumetric flow rate and the applied electric field, respectively. The material parameters include $\rho, \gamma, K, \varepsilon$ and η, i.e. density, surface tension at the interface, electrical conductivity, dielectric constant, and viscosity of the polymer solution, respectively. Nonetheless, generalized parametric relationship of the diameter along the straight section of the jet from the apex of the Taylor cone to the initiation of the bending instability, derived in section 3.2 and extensively discussed in section 3.4 is given as:

$$d = f(Q, E, \gamma, K, \varepsilon, \rho, z, g, r_0), \tag{2.5}$$

where r_0 is the internal radius of the nozzle, z is the distance measured along the axial direction from the apex of the Taylor cone. During the dimensional analysis in Chapters, 2 to 4, extensional viscosity is employed, given by the limiting relationship $\eta_e = 3\eta$. The number of governing parameters was reduced to a manageable number by making calculated assumptions with the help of dimensionless numbers. Reynolds number $\left(Re_r = \frac{2\rho Q}{\pi r \eta_e}\right)$ based on jet radius at the apex of Taylor cone (r) for the complete analyzed data is $2.9 \times 10^{-3} < Re_r < 7.8$. Additionally, the range of Reynolds number $\left(Re_{r_o} = \frac{2\rho Q}{\pi r_o \eta_e}\right)$ based on nozzle radius (r_o) is $5.8 \times 10^{-4} < Re_{r_o} < 7.0 \times 10^{-1}$. The relatively small Reynolds number signifies the importance of viscosity and therefore, its inclusion in the dimensional analysis as well as the omission of density from the analysis. The large range of Froude number $(8.01 \times 10^1 < Fr_r < 3.4 \times 10^5)$ also signifies the insignificance of acceleration due to gravity for the straight section of the jet. Furthermore, the nozzle diameter may not be the correct characteristic diameter as appreciable degree of stretching is observed from the nozzle along the straight section of the electrospun jet.

As the diameter at the apex of the Taylor cone corresponds to z = 0, therefore, Equation (2.6) after discarding ρ, g, r_0 and z and incorporating η_e, is employed for the dimensional analysis to correlate apex diameter with the process as well as material parameters:

$$d = f(\gamma, \eta_e, K, \varepsilon, E, Q), \tag{2.6}$$

Hence, dimensional analysis yields:

$$\frac{d\eta_e K}{\gamma\varepsilon} = f\left(\frac{E\varepsilon}{(\eta_e K)^{1/2}}, \frac{Q{\eta_e}^3 K^2}{\gamma^3 \varepsilon^2}\right). \tag{2.7}$$

Through dimensional analysis, dimensionless apex diameter $\left(\tilde{d} \equiv \frac{d\eta_e K}{\gamma\varepsilon}\right)$, as a function of dimensionless flow rate $\left(\tilde{Q} \equiv \frac{Q{\eta_e}^3 K^2}{\gamma^3 \varepsilon^2}\right)$, and dimensionless electric field $\left(\tilde{E} \equiv \frac{E\varepsilon}{(\eta_e K)^{1/2}}\right)$ was obtained as depicted in Equation (2.7) and shown in Figure 2.5. It should be noted that the characteristic length scale is given by $\left(\frac{\gamma\varepsilon}{\eta_e K}\right)$, which consists of material parameters. This is more meaningful than using a constant nozzle radius (r_0) as done in the literature. In Figure 2.5, each color/symbol represents the wt% of a given polymer in distilled water. Four data values for each color/symbol represent different process parameters. Figure 2.5 (a) shows that dimensionless apex diameter $\tilde{d}$ is a very strong function of the dimensionless flow rate $\widetilde{Q}$ and rather weak function of dimensionless electric field $\widetilde{E}$.

Figure 2.5 (b) depicts the relationship between dimensionless apex diameter and dimensionless electric field for constant values of polymer solution concentrations. It can be seen from Figure 2.5 (a) that there is little overlapping of data points corresponding to constant dimensionless flow rates. Therefore, no constant flow rate lines can be generated in Figure 2.5 (b). However, Figure 2.5 (b) shows that there is overlapping of data points corresponding to the constant dimensionless electric field, which are depicted by vertical dashed lines. Subsequently, these constant dimensionless electric field lines were plotted as three red/solid lines in Figure 2.5 (a). The slopes of these three parallel dimensionless electric field lines is 0.49, but with slightly different vertical intercepts (log(*B*)). Therefore,

the dimensionless apex diameter of the electrospun jet can be expressed in terms of dimensionless flow rate given by the Equation (2.8):

$$\log\left(\frac{d\eta_e K}{\gamma\varepsilon}\right) = m \times \log\left(\frac{Q{\eta_e}^3 K^2}{\gamma^3 \varepsilon^2}\right) + \log(B). \tag{2.8}$$

As the effect of dimensionless electric field is more prominent in log(*B*) than *m*, *m* is taken to be a constant value of 0.49, whereas log(*B*) is considered as a correction factor as depicted in Figure 2.6. Thus, if the effect of electric field is to be considered on the apex diameter, Equation (2.8) can be employed for constant *m* with varying log(*B*). As evident in Figure 2.5 (a), the dimensionless electric field has a relatively small effect on the dimensionless apex diameter of the electrospun jet. If the effects of dimensionless electric field are neglected, a more general correlation formula consisting of only two dimensionless parameters can be obtained. This two-parameter general correlation formula, which is shown as a dashed line in Figure 2.5 (a), is given by Equation (2.9).

$$\log\left(\frac{d\eta_e K}{\gamma\varepsilon}\right) = m \times \log\left(\frac{Q{\eta_e}^3 K^2}{\gamma^3 \varepsilon^2}\right) + \log(A). \tag{2.9}$$

The slope *m* and the intercept log(*A*) for the best-fit dashed line are 0.44 and 0.0158, respectively. Removing the logarithm, we obtain the correlation between the dimensionless apex diameter of the electrospun jet and dimensionless flow rate as:

$$\tilde{d} = 1.03\tilde{Q}^{0.44}. \tag{2.10}$$

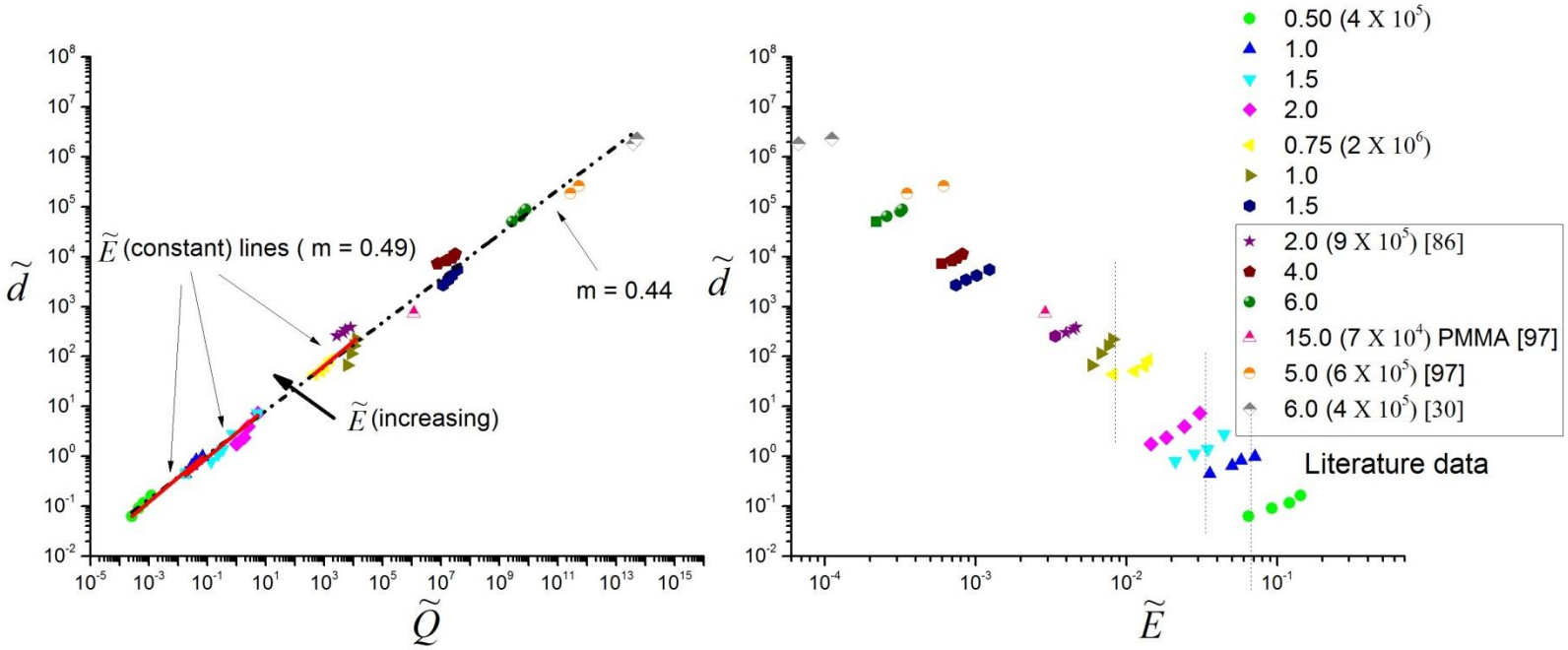

Figure 2.5 Dimensionless diameter at the apex of the Taylor cone vs. (a) the dimensionless flow rate, and (b) the dimensionless electric field for different operating parameters. Each color/symbol represents the wt% of a given polymer in distilled water. The numerical quantity in the bracket represents the molecular weight of the polymer employed. Four data values for each color/symbol represents different process parameters. Literature data correspond to the symbols against the legend placed inside the box.

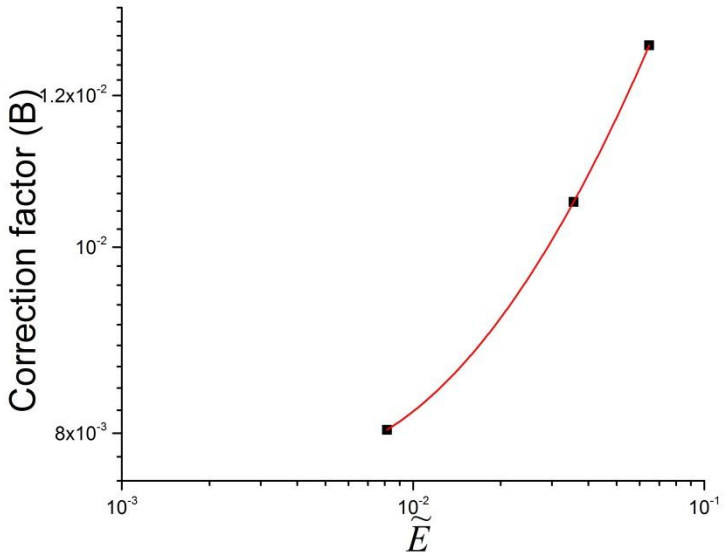

Figure 2.6 The correction factor as a function of dimensionless electric field.

The correlation formula is valid for the analyzed range of dimensionless flow rates $\left(2.6 \times 10^{-4} < \tilde{Q} < 3.6 \times 10^{7}\right)$ and dimensionless electric fields $\left(7.4 \times 10^{-4} < \tilde{E} < 1.4 \times 10^{-1}\right)$. Additionally, the correlation formula is valid for the analyzed range of dimensionless numbers, $3.3 \times 10^{-7} < De_{r_o} < 3.8 \times 10^{-2}$, $5.8 \times 10^{-4} < Re_{r_o} < 7.0 \times 10^{-1}$, $4.2 \times 10^{-5} < De_r < 3.8 \times 10^{1}$ and $2.9 \times 10^{-3} < Re_r < 7.8$.

To check the validity of the correlation formula, comparisons are made with the data presented in the literature. The data compared with the proposed correlation formula include 15 wt% PMMA (M_w = 70,000) chloroform solution [97] and 2, 4 and 6 wt% PEO (M_w = 900,000) water solution [86], 6 wt% PEO (M_w = 400,000) water solution [30] and 5 wt% PEO (M_w = 600,000) water solution [97]. The literature data were found to compare well with the correlation formula related to the straight section of the jet, thus validating the applicability of correlation formula under the assumptions made during the analysis. The

literature data also helped in extending the range of the dimension parameters under which the proposed correlation formula is valid. Therefore, the correlation formula for the diameter at the apex of the Taylor cone with the addition of literature data is valid for the given range of dimensionless flow rates $\left(2.6 \times 10^{-4} < \tilde{Q} < 5.1 \times 10^{13}\right)$ and dimensionless electric fields $\left(6.7 \times 10^{-5} < \tilde{E} < 1.4 \times 10^{-1}\right)$. Additionally, the correlation formula is valid for the analyzed range of dimensionless numbers, $3.3 \times 10^{-7} < De_{r_o} < 3.2 \times 10^{-1}$ and $2.0 \times 10^{-4} < Re_{r_o} < 7.0 \times 10^{-1}$.

2.7 Conclusion

An experimental investigation of the jet diameter (d) at the apex of the Taylor cone emitted from electrified menisci was performed. Three dimensionless parameters, namely dimensionless apex diameter $\tilde{d}$, dimensionless flow rate $\tilde{Q}$, and dimensionless electric field $\tilde{E}$ were found to govern the jet characteristics at the apex of the Taylor cone. The relevant correlation formulae with/without the influence of electrical parameter were devised. Consequently, the correlation formula $\left(\tilde{d} = 1.03\tilde{Q}^{0.44}\right)$ for the diameter at the apex of the Taylor cone ignoring the weak $\tilde{E}$ effect was formulated. The correlation formula is valid for the analyzed range of dimensionless flow rates $\left(2.6 \times 10^{-4} < \tilde{Q} < 3.6 \times 10^{7}\right)$ and dimensionless electric fields $\left(7.4 \times 10^{-4} < \tilde{E} < 1.4 \times 10^{-1}\right)$. Additionally, the correlation formula is valid for the analyzed range of dimensionless numbers, $3.3 \times 10^{-7} < De_{r_o} < 3.8 \times 10^{-2}$, $5.8 \times 10^{-4} < Re_{r_o} < 7.0 \times 10^{-1}$, $4.2 \times 10^{-5} < De_r < 3.8 \times 10^{1}$ and $2.9 \times 10^{-3} < Re_r < 7.8$.

The validity of the correlation formula was further increased with the help of literature data. Therefore, the correlation formula for the diameter at the apex of the Taylor cone with the addition of literature data is valid for the given range of dimensionless flow rates $\left(2.6 \times 10^{-4} < \tilde{Q} < 5.1 \times 10^{13}\right)$ and dimensionless electric fields $\left(6.7 \times 10^{-5} < \tilde{E} < 1.4 \times 10^{-1}\right)$ and dimensionless numbers, $3.3 \times 10^{-7} < De_{r_o} < 3.2 \times 10^{-1}$ and $2.0 \times 10^{-4} < Re_{r_o} < 7.0 \times 10^{-1}$. The correlation formula combined with the other correlation formulae discussed in Chapters 3 and 4 will help in the control and optimization of electrospinning phenomenon.

Chapter 3 Analysis of straight section of the electrospun jet

3.1 Introduction

This chapter covers aspects of the straight section of the electrospun jet. In section 3.2, asymptotic solutions pertaining to the straight section of an electrified jet are studied to help in the dimensional analysis. In section 3.3, the jet radii for the straight section are measured against the process as well as the material parameters. In section 3.4, a comprehensive dimensional analysis is presented to obtain pertinent parameters to scheme relevant 'correlation formula.' This 'correlation formula' is intended to predict the diameter of the electrospun jet at different locations against the given operating parameters. It is envisioned that correlation formula would help in the determination of appropriate jet characteristics to control, optimize, and improve the electrospinning phenomenon. Finally, results are summarized in section 3.5.

3.2 Asymptotic solutions pertaining to the straight section of the electrospun jet

Before devising the correlation formula, a comprehensive analysis of the asymptotic solutions of the electrospun jet is performed. A variety of asymptotic solutions has been proposed to estimate the radius of the thinning jet against the operating parameters. This is possible because electrospun jet enters its power law asymptotic regime relatively quickly after it exits the nozzle. The power law asymptotic variation of dimensionless radius $(\tilde{r})$ can be given by the relation $(r/r_0) \sim (z/r_0)^{-b}$ or $\tilde{r} \sim \tilde{z}^{-b}$, where $\tilde{z}$ is the corresponding dimensionless axial distance and b is a positive exponent. Dimensionless axial distance is measured from the nozzle exit, i.e. at nozzle exit, z is equal to zero and r corresponds to the internal radius of the nozzle (r_0).

A number of asymptotic relationships were obtained by correlating relevant forces for a given flow regime. Kirichenko et al. [94], was one of the first researchers to formulate an asymptotic relationship for the radius of a Newtonian jet in a uniform electric field. The jet radius followed a power law relationship with the axial distance i.e. $\tilde{r} \sim \tilde{z}^{-1/4}$. The other notable power law exponent obtained is $b = 1$. Reznik et al. [95] obtained $b = 1$ for capillary-dominated viscous electrified jet. Similarly, Rutledge et al. [96] predicted $b = 1$ for near-nozzle to the asymptotic transition regime. Rutledge et al. obtained the asymptotic scaling by the balance between electrostatic and viscous stresses. On the other hand, Spivak et al. [77] obtained an asymptotic solution based on rheological constitutive equation governing the behavior of the non-Newtonian jet. The power law rheological constitutive equation employed was $\tau_v = \left(\dot{s}\eta\left((\Pi_i)^{(f-1)/2}\right) - PI_i\right)$. The symbols include the viscous shear stress tensor (τ_v), the second invariant (Π_i) corresponding to strain rate tensor $(\dot{s})$, the flow index (*f*), the hydrostatic pressure (*P*), and the unit tensor (I_i). They obtained $b \geq 1/2$ for $f > 2$. The solution was found to converge to $b = 1/2$ for jets with high flow indices.

Greenfeld et al. [97] correlated dimensionless radius with dimensionless axial length with the help of a dimensionless parameter $\left(\tilde{r} \sim \left(\frac{1}{\Lambda}\right)\tilde{z}^{-1/2}\right)$. The calculated dimensionless parameter (Λ) was the combination of Peclet number, electric Bond number, and the capillary number. Greenfeld et al. [97] obtained the dimensionless parameter (Λ) for two different flow regimes. These flow regimes include viscosity-dominated and capillary-dominated flow regimes. The dimensionless parameter for viscosity-dominated flow regime was independent of surface tension. Similarly, a dimensionless parameter for capillary-

dominated flow regime was independent of solution viscosity. Dimensionless parameter for these flow regimes were $\left(\Lambda_{vis} = \bar{\varepsilon}^{1/6}\left(\frac{2v_0}{Kr_0}\right)^{-1/4}\left(\frac{r_0E^2}{\gamma}\right)^{5/12}\left(\frac{\eta v_0}{\gamma}\right)^{-5/12}\right)$ for viscosity-dominated and $\left(\Lambda_{cap} = \bar{\varepsilon}^{2/7}\left(\frac{2v_0}{Kr_0}\right)^{-3/7}\left(\frac{r_0E^2}{\gamma}\right)^{5/7}\right)$ for capillary-dominated flow regime. Here, the relation $\left(v_0 = \frac{Q}{(\pi r_0^2)}\right)$ gives the characteristic velocity. Greenfeld et al. [97] observed improved correlation with experimental data for dimensionless parameter pertaining to viscosity-dominated flow regime. Nevertheless, asymptotic solutions by Greenfeld et al. present two extreme results pertaining to the straight section of the electrospun jet. It will be shown during dimensional analysis in section 3.4 that both surface tension and viscosity are relevant for the straight section of the electrospun jet.

Although a number of power law exponents are obtained, nevertheless, $b = 1/4$ is the exponent verified through experimental analysis. Greenfeld et al. [97] modeled the straight section of the electrospun jet based on the simplest version of the Upper-convected Maxwell model of viscoelasticity, also employed by Yarin et al. [24]. They observed $b = 1/4$ over a wide range of operating parameters. Feng [29] also obtained asymptotic scaling $\tilde{r} \sim \tilde{z}^{-1/4}$, close to the lower end of the electrospun jet. Feng observed that as $\tilde{z} \to \infty$ at the lower end of jet, $\tilde{r} \to 0$. From Equation (1.6), $\tilde{v} \sim \tilde{r}^{-2}$ for constant flow rate. At the lower end of the jet, convection is considered as the dominant mode of charge transfer. Therefore, from Equation (1.7), $\tilde{\sigma} \sim (\tilde{r}\tilde{v})^{-1} \sim \tilde{r} \to 0$. This implies that the electric field becomes uniform and equal to the externally applied electric field. Therefore, in Equation (1.8), only the electrostatic, inertia, and gravity terms remain finite, thus resulting in $\tilde{v}\tilde{v}' = -2\tilde{r}^{-5}\ \tilde{r}' = O(1)$, which leads to the scaling relationship $\tilde{r} \sim \tilde{z}^{-1/4}$.

Similarly, Hohman [96, 98] also obtained $b = 1/4$ at the lower end of the Newtonian fluid jet placed in an axially applied electric field. The dimensionless equations for the conservation of mass, charge, conservation of momentum, and the tangential field inside the jet were given as follows:

$$\tilde{r}^2\tilde{v} = \tilde{Q}, \tag{3.1}$$

$$\tilde{\sigma}\tilde{r}\tilde{v} + \frac{K^*}{2}\tilde{r}^2\tilde{E}_z = \tilde{I}, \tag{3.2}$$

$$\left(\frac{\tilde{v}^2}{2}\right)' = -\left(\frac{1}{\tilde{r}} - 2\pi\tilde{\sigma}^2 - \frac{\tilde{E}_z{}^2}{8\pi} - \tilde{r}''\right)' + g^* + \frac{2\tilde{\sigma}\tilde{E}_z}{\tilde{r}\sqrt{\beta}} + \frac{3\upsilon^*}{\tilde{r}^2}(\tilde{r}^2\tilde{v}')', \tag{3.3}$$

$$\tilde{E}_z - ln\left(\frac{1}{\chi}\right)\left[\frac{\beta}{2}\left(\tilde{r}^2\tilde{E}_z\right)'' - 4\pi\sqrt{\beta}(\tilde{r}\tilde{\sigma})'\right] = \tilde{E}, \tag{3.4}$$

where $\tilde{Q} = \frac{Q\tau_\gamma}{(\pi r_0^3)}$, $\tilde{I} = \frac{I\tau_\gamma}{(2\pi {r_0}^2\sigma_{sc})}$, $\beta = \left(\frac{\varepsilon}{\bar{\varepsilon}}\right) - 1$, $K^* = K\sqrt{\frac{\rho r_0^3}{(\beta\gamma)}}$, $\upsilon^* = \sqrt{\frac{\upsilon^2}{(\rho\gamma r_0)}}$, $g^* = \frac{g\rho r_0^2}{\gamma}$, $\tau_\gamma = \sqrt{\frac{\rho {r_0}^3}{\gamma}}$. Surface charge density is non-dimensionalized with $\sigma_{sc} = \sqrt{\frac{\gamma(\bar{\varepsilon})}{r_0}}$. E_z and E were non-dimensionalized with $E_0 = \sqrt{\frac{\gamma}{(\varepsilon - \bar{\varepsilon})r_0}}$. Q is the volumetric flow rate, I is current flowing through the jet and r_0 is the internal radius of nozzle. The other symbols have their usual meaning. Hohman assumed that as the jet thins asymptotically ($\tilde{z} \to \infty \ \to \tilde{r} \to 0$), it could be approximated as a cylinder. Furthermore, for a cylindrical jet, the electric field within the jet can be considered equal to the externally applied electric field strength, i.e. $\tilde{E}_z \to \tilde{E}$. The other assumption was that in the asymptotic regime, the current is carried through convection resulting $\tilde{\sigma} \to \frac{\tilde{I}\tilde{r}}{\tilde{Q}}$. Furthermore in the asymptotic regime, the dominant balance in the

momentum equation is between forces due to inertia, tangential electric stress, and gravity, thus resulting in:

$$\left(\frac{\tilde{v}^2}{2}\right)' = \left(\frac{\tilde{Q}^2}{2\tilde{r}^4}\right)' \approx g^* + \frac{2\tilde{\sigma}\tilde{E}_z}{\tilde{r}\sqrt{\beta}} = g^* + \frac{2\tilde{I}\tilde{E}}{\tilde{Q}\sqrt{\beta}}. \tag{3.5}$$

The resultant momentum equation, after some calculation, resulted in the given asymptotic relationship for the dimensionless radius of the jet.

$$\tilde{r} \approx \tilde{z}^{-1/4}\left(\frac{2g^*}{\tilde{Q}^2} + \frac{4\tilde{I}\tilde{E}}{\tilde{Q}^3\sqrt{\beta}}\right)^{-1/4}. \tag{3.6}$$

Therefore, the generalized parametric relationship for jet radius in terms of process as well as material parameters can be given as:

$$r = f(Q, E, \gamma, K, \varepsilon, \rho, z, g, r_0). \tag{3.7}$$

Before performing extensive dimensional analysis, we will analyze parametric Equation (3.7) to gain a better understating of governing parameters on the radius of the electrospun jet. For the general case of electrohydrodynamics, four repeating parameters are usually employed. For four repeating parameters, Equation (3.7) containing ten parameters will result in six dimensionless parameters. Large number of dimensionless parameters will make it difficult to formulate a two or three parameter operating system. Nevertheless, the governing dimensionless parameters can be reduced to a manageable number by making calculated assumptions.

For instance, it was observed that reduction in Froude number by a factor of 10 resulted in about 5% change in radius of the jet, depicting the Froude number as a relatively insignificant parameter [28]. The gravitational forces were found to be smaller than inertial forces along the straight section of the jet, which were in turn smaller than electrostatic and

viscous forces pertaining to the electrospinning process (discussed later). This signifies that ρ, g can be discarded from Equation (3.7) for the analysis of straight section of the electrospun jet. The other shortcoming of Equation (3.7) is the use of internal diameter of the nozzle as the characteristic jet diameter. This may not be the correct characteristic diameter as appreciable degree of stretching is observed as the jet traverses from the nozzle-tip to the collector surface. Therefore, a characteristic diameter based on material parameters should be used to better signify the local flow characteristics.

Asymptotic analysis by Hohman did not include viscosity of the polymer solution. The viscosity of the polymer solution turns out to be a relevant parameter for the dimensional analysis pertaining to the straight section of the electrospun jet. Thus, governing dimensionless parameters can be reduced to a manageable number (four) by discarding ρ, g, r_0 and incorporating η_e in Equation (3.7), as discussed in detail in section 3.4.

3.3 Analysis of the radius of the straight section of the electrospun jet

Initially, we collected the raw data pertaining to the radius of the straight section of the jet to be employed in the dimensional analysis. The setup shown in Figure 2.1 (a) was employed to capture the complete radius profile of the straight section of the electrospun jet against the process and material parameters. A representative set of data is plotted in Figure 3.1 depicting the variation in the jet radius with applied electric field and volumetric flow rate (process parameters) for a given concentration of polymer solution (material parameters). The plots shown in Figure 3.2 depict the variation of jet radius with respect to the axial distance for different operating parameters corresponding to a representative polymer solution.

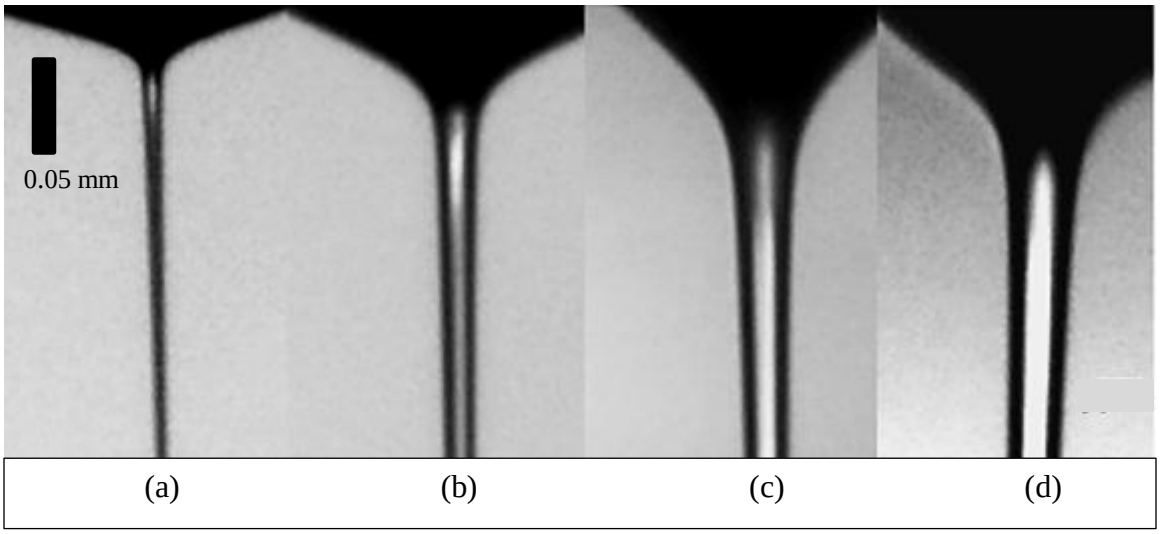

Figure 3.1 The image depicts the variation in the jet diameter with the variation in the electric field (flow rate) as followed: (a) 43.09 (0.03), (b) 60.60 (0.05), (c) 86.19 (0.12), and (d) 90.64 (0.13) kV/m (ml/min). The concentration of polymer solution used is 1 wt% PEO (M_w = 400,000) dissolved in distilled water.

All the radius profiles show the same qualitative behavior, regardless of the variation of the material or process parameters. Process parameters, i.e., applied electric field and volumetric flow rate, were obtained for the stable jetting condition for a given concentration of polymer solution. It is worthwhile to mention that by varying the concentration of the polymer solution, we have effectively varied all the relevant material parameters such as density, polymer relaxation time, surface tension, electrical conductivity, dielectric constant, and viscosity. Variation of these process and material parameters was found to vary the resultant jet diameter [99]. Results have shown that the diameter of the electrospun jet decreases with the decrease in the concentration of the polymer solution [100]. On the other hand, as the concentration of the polymer solution increases, the viscosity increases, and higher electrical forces are required to overcome both the surface tension and the viscoelastic forces for stretching the jet, thus resulting in a thick jet [101-104].

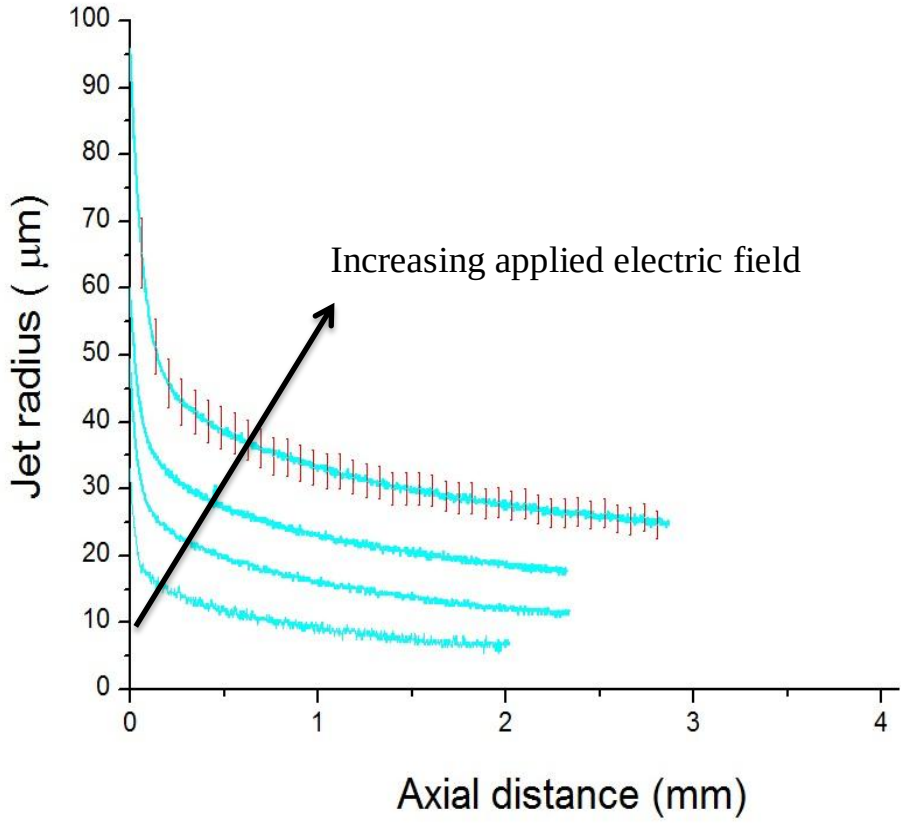

Figure 3.2 A representative plot of radius vs. axial length profile for 1.5 wt% (M_w = 400,000) for 40.40 (0.02), 53.87 (0.04), 65.99 (0.05) and 84.84 (0.11) kV/m (ml/min). The error bars denote an error of 8% of the absolute value.

Viscosity and subsequently the radius of the jet can also be increased by increasing the molecular weight of polymer for a given concentration of the polymer solution [105].

3.4 Dimensional analysis pertaining the straight section of the jet

Firstly, we will try to shed more light on the dominant forces controlling the dynamics of the electrospun jet as it moves from the apex of the Taylor cone to the initiation of bending instability. The dimensionless numbers analyzed are Deborah number, Reynolds number, Capillary number, and Froude number. The variation in the Deborah number ($De_r = \frac{\tau_p Q}{\pi r^3}$, where τ_p is the polymer relaxation time) as the jet travels from the apex of the Taylor cone to

the initiation of the bending instability for the complete data employed for the dimensional analysis based on jet radius (r) is $3.3 \times 10^{-4} < De_r < 4.7 \times 10^{4}$. However, the range of Deborah number $\left(De_{r_o} = \frac{\tau_p Q}{\pi {r_o}^3}\right)$ based on nozzle radius (r_o) is $3.3 \times 10^{-7} < De_{r_o} < 3.8 \times 10^{-2}$.

Under the condition of a relatively low Deborah number based on nozzle radius, extensional viscosity was employed in the dimensional analysis, given by the limiting relationship $\eta_e = 3\eta$. The limiting relationship was employed to incorporate the variation in viscosity of the polymer solution under uniaxial stretching [28, 86]. It is noted that the extensional viscosity may be appropriate for the onset of the straight section of the jet; nevertheless, it may underestimate the extensional viscosity towards the end of the straight section. Therefore, the limiting relationship for extensional viscosity may affect the proposed correlation formulae; nevertheless, excellent correlation of the data for the aqueous PEO solutions and other polymer-solvent systems is observed, thus validating the approach.

Similarly, the range of Reynolds number $\left(Re_r = \frac{2\rho Q}{\pi r \eta_e}\right)$ based on jet radius is $2.9 \times 10^{-3} < Re_r < 3.9 \times 10^{1}$. However, the range of Reynolds number $\left(Re_{r_o} = \frac{2\rho Q}{\pi r_o \eta_e}\right)$ based on nozzle radius (r_o) is $5.8 \times 10^{-4} < Re_{r_o} < 7.0 \times 10^{-1}$. The relatively small Reynolds number signifies that viscosity plays an important role along the straight-line trajectory of the electrospun jet. Furthermore, the low Reynolds number signifies a predominantly laminar flow regime. This also indicates that viscous effects become significant whereas inertia becomes less relevant along the straight section of the electrospun jet.

For low Reynolds numbers, the significance of viscous effects suggests the high relevance of the Capillary number $\left(Ca_r = \frac{\eta_e Q}{\gamma r^2}\right)$. The capillary number signifies the importance of interfacial stress with the reduction in the jet radius and therefore the inclusion of γ as a repeating parameter in the dimensional analysis. The range of Capillary numbers $\left(Ca_r = \frac{\eta_e Q}{\gamma r^2}\right)$ for the data employed for the dimensional analysis based on jet radius (r) is $3.9 \times 10^{-3} < Ca_r < 3.5 \times 10^{3}$. However, the range of Capillary number $\left(Ca_{r_o} = \frac{\eta_e Q}{\gamma r^2}\right)$ based on nozzle radius (r_o) is $1.6 \times 10^{-4} < Ca_{r_o} < 3.5 \times 10^{-1}$.

The complete range of Froude number $\left(Fr_r = \frac{Q^2}{g\pi^2 r^5}\right)$ based on jet radius is $8.0 \times 10^{1} < Fr_r < 3.4 \times 10^{5}$. However, the range of Froude number $\left(Fr_{r_o} = \frac{Q^2}{g\pi^2 {r_o}^5}\right)$ based on nozzle radius (r_o) is $3.5 \times 10^{-5} < Fr_{r_o} < 8.6 \times 10^{-4}$. The relatively large Fr_r along the jet's trajectory signifies that the effect of gravitational forces is smaller than inertial forces. Moreover, inertia is smaller than viscous forces inferred from low Re_r. This further emphasizes the fact that the flow regime is predominantly viscous in nature.

The above dimensional analysis reiterates the fact that the viscosity is dominant whereas density and gravity can be neglected in the current analysis. Therefore, the resultant repeating parameters are η_e, γ, K and ε. The significance of these repeating parameters was also confirmed by the mathematical analysis performed in the section 3.2 pertaining to the straight section of the electrospun jet. It was noted from the raw data collected in section 3.3 that the radius of the straight section of the electrospun jet varies in the axial direction. Therefore, axial distance was included in the analysis as an independent parameter. Therefore, independent parameters for the analysis were $d, E, Q, z,$ i. e. diameter of jet,

applied electric field, flow rate, and axial distance, respectively. The equation depicting repeated and independent parameter is:

$$d = f(\gamma, \eta_e, K, \varepsilon, E, Q, z). \tag{3.8}$$

Dimensional analysis yields

$$\frac{d\eta_e K}{\gamma\varepsilon} = f\left(\frac{E\varepsilon}{(\eta_e K)^{1/2}}, \frac{Q{\eta_e}^3 K^2}{\gamma^3 \varepsilon^2}, \frac{z\eta_e K}{\gamma\varepsilon}\right), \tag{3.9}$$

where dimensionless jet diameter $\left(\tilde{d} \equiv \frac{d\eta_e K}{\gamma\varepsilon}\right)$ is a function of dimensionless flow rate $\left(\tilde{Q} \equiv \frac{Q{\eta_e}^3 K^2}{\gamma^3 \varepsilon^2}\right)$, electric field $\left(\tilde{E} \equiv \frac{E\varepsilon}{(\eta_e K)^{1/2}}\right)$ and the axial distance $\left(\tilde{z} \equiv \frac{z\eta_e K}{\gamma\varepsilon}\right)$. Figure 3.3 (a, b) depicts dimensionless diameter at different axial locations ($\tilde{z}$) along the straight section of jet against the dimensionless parameters $\left(\tilde{Q} \text{ and } \widetilde{E}\right)$, respectively. The locations along the straight section of the jet were governed by the dimensionless axial distance given in Table 3.1.

Table 3.1 Dimensionless axial distance along the straight section of the jet, calculated from the apex of the Taylor cone.

$\widetilde{z1}$	$\widetilde{z2}$	$\widetilde{z3}$	$\widetilde{z4}$	$\widetilde{z5}$	$\widetilde{z6}$	$\widetilde{z7}$	$\widetilde{z8}$	$\widetilde{z9}$	$\widetilde{z10}$	$\widetilde{z11}$
0.41	2.03	4.06	20.3	40.6	203	406	812	2030	4060	24400

In Figure 3.3, each color/symbol represents the wt% of a given polymer in distilled water. Four data values for each color/symbol represent different process parameters $\widetilde{Q}$ and $\widetilde{E}$. Different internal geometry (solid, hollow, half-filled and '+') for a given color/symbol represents different dimensionless axial distance $\tilde{z}$ as shown in the

legend. The dimensionless axial distances were measured from the apex of Taylor cone and chosen to lie within the straight section for a given wt% of the polymer solution.

It is evident from Figure 3.3 that the data values did not collapse on a straight line and require further analysis. Since Equation (3.9) involves four dimensionless parameters, it is difficult to represent the data in two-dimensional plots while keeping the other two parameters constant. The motivation now is to reduce it to a three-parameter system by combining the two geometric parameters $\tilde{d}$ and $\tilde{z}$. This is achieved with the help of analysis presented in Figure 3.4.

As $\tilde{d}$ and $\tilde{z}$ are measured along the same electrospun jet for the given process parameters $\tilde{Q}$ and $\tilde{E}$, each constant slope line represents a line of constant $\tilde{Q}$ and $\tilde{E}$. Hence, the relationship between $\tilde{d}$ and $\tilde{z}$ can be established. It is evident from Figure 3.4 that all the lines have the same slope of -0.25, which is consistent with asymptotic relationship $\left(\tilde{d} \sim \tilde{z}^{-1/4}\right)$ discussed in section 3.2. The relationship was found to be valid under the condition $z/d > 20$. This implies that the diameter of the jet should be obtained at least $20d$ away from the Taylor cone, for the given asymptotic relationship to be valid. This asymptotic relation $\left(\tilde{d} \sim \tilde{z}^{-1/4}\right)$ helped to combine two of the parameters resulting in a three-parameter system depicted by Equation (3.10), and plotted in Figure 3.5.

$$\left(\frac{d\eta_e K}{\gamma\varepsilon}\right) \times \left(\frac{z\eta_e K}{\gamma\varepsilon}\right)^{1/4} = f\left(\frac{E\varepsilon}{(\eta_e K)^{1/2}}, \frac{Q{\eta_e}^3 K^2}{\gamma^3 \varepsilon^2}\right). \tag{3.10}$$

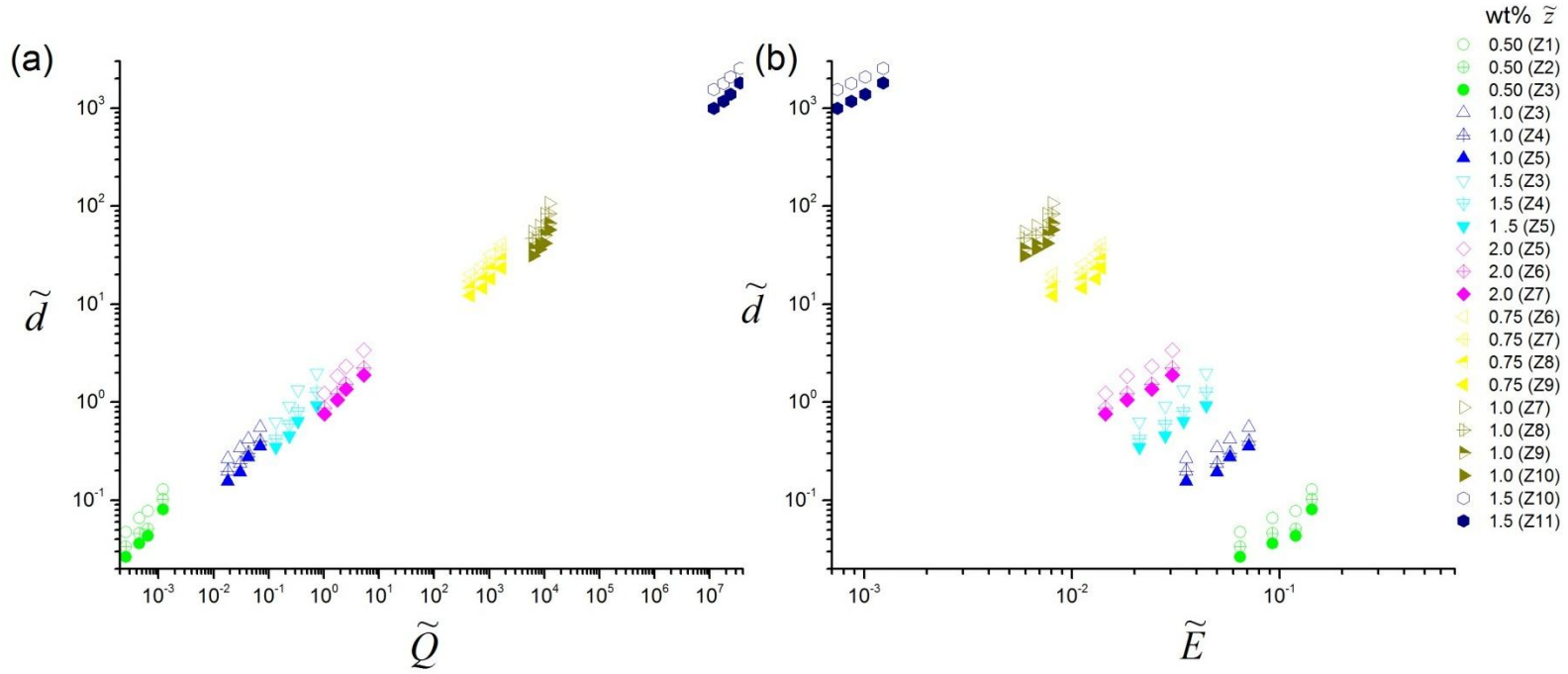

Figure 3.3 Dimensionless diameter along the straight section of jet vs. (a) the dimensionless flow rate, (b) the dimensionless electric field for different operating parameters. Each color represents the wt% of a given polymer in distilled water. Four data values for each color represent different process parameters. Different symbol represents a different dimensionless axial length, written in brackets.

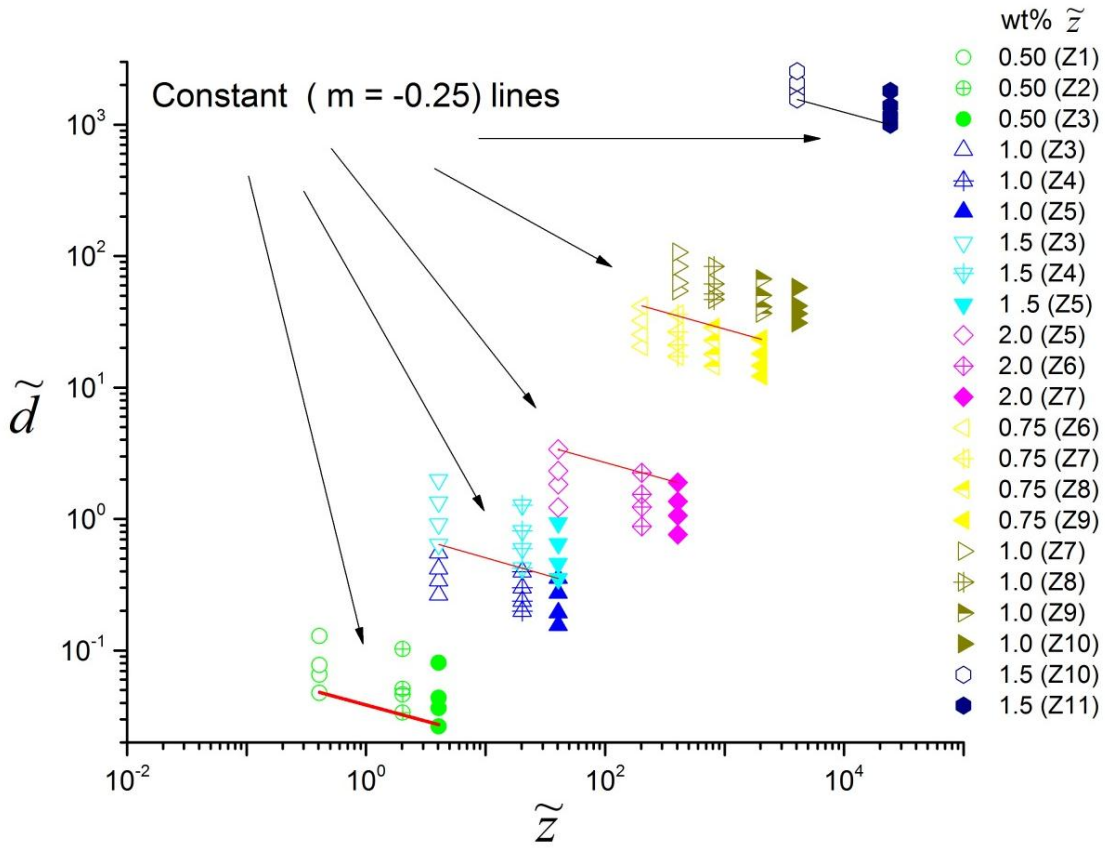

Figure 3.4 Dimensionless diameter of the straight section of jet vs. dimensionless axial distance for different operating parameters. Each color represents the wt% of a given polymer in distilled water. Four data values for each color represent different process parameters. Different symbol represents different dimensionless axial distance, written in brackets.

Figure 3.5 shows that the combined dimensionless geometric parameter $\left(\tilde{d}\tilde{z}^{1/4}\right)$ is a very strong function of the dimensionless flow rate $\tilde{Q}$ and rather weak function of dimensionless electric field $\tilde{E}$. Similar to the analysis for the diameter at the apex of the Taylor cone, further analysis was performed in order to predict the effect of dimensionless electric field on the dimensionless geometric parameter $\left(\tilde{d}\tilde{z}^{1/4}\right)$. Vertical dashed lines in Figure 3.5 (b) depicted data values corresponding to the constant dimensionless electric field. Then, these three constant dimensionless electric field lines were plotted on Figure 3.5 (a) as three color/solid

lines (two of which are overlapping). The slopes of these three parallel dimensionless electric field lines is 0.55, but with slightly different vertical intercepts (log(*B*)). Therefore, the dimensionless geometric parameter $\left(\tilde{d}\tilde{z}^{1/4}\right)$ can be expressed in terms of dimensionless flow rate given by the following equation.

$$\log\left(\left(\frac{d\eta_e K}{\gamma\varepsilon}\right)\times\left(\frac{z\eta_e K}{\gamma\varepsilon}\right)^{1/4}\right) = m\times\log\left(\frac{Q{\eta_e}^3K^2}{\gamma^3\varepsilon^2}\right) + \log(B). \qquad (3.11)$$

As the effect of dimensionless electric field is more prominent in log(*B*) than *m*, *m* is taken to be a constant value of 0.55, whereas log(*B*) is considered as a correction as depicted in Equation (3.11) plotted in Figure 3.6. Thus, if the effect of electric field is to be considered on the combined dimensionless geometric parameter $\left(\tilde{d}\tilde{z}^{1/4}\right)$, Equation (3.11) can be employed for constant *m* with varying log(*B*).

As evident in Figure 3.5 (a), the dimensionless electric field has an even smaller effect on the dimensionless geometric parameter than the diameter at the apex of the Taylor cone shown in Figure 2.5 (a). If the effects of dimensionless electric field are neglected, a more general correlation formula consisting of only two dimensionless parameters can be obtained. This two-parameter general correlation formula, which is shown as a dashed line in Figure 3.5 (a), is given by the following equation.

$$\log\left(\left(\frac{d\eta_e K}{\gamma\varepsilon}\right)\times\left(\frac{z\eta_e K}{\gamma\varepsilon}\right)^{1/4}\right) = m\times\log\left(\frac{Q{\eta_e}^3K^2}{\gamma^3\varepsilon^2}\right) + \log(A). \qquad (3.12)$$

The slope *m* and the intercept log(*A*) for the best-fit dashed line are 0.50 and 0.035, respectively.

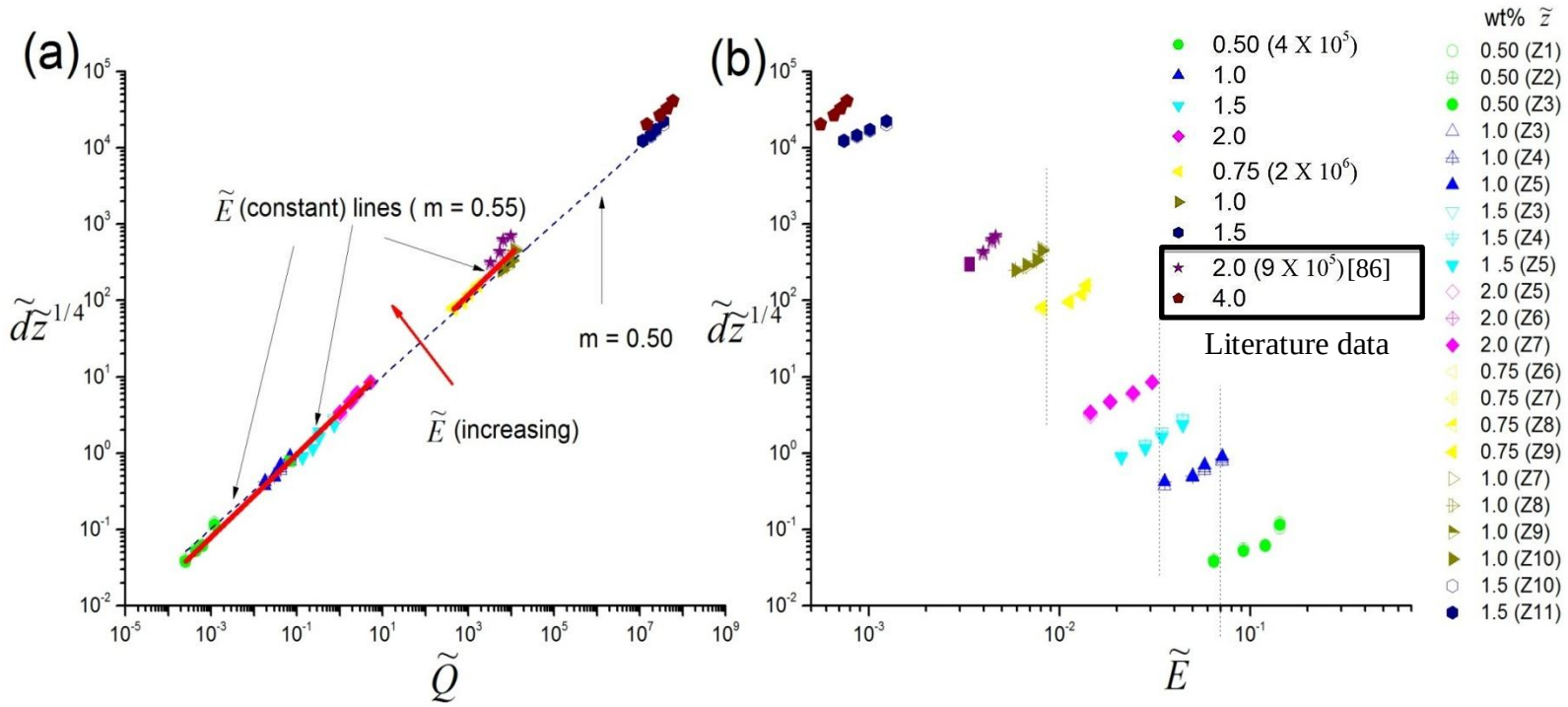

Figure 3.5 Dimensionless geometric parameter for the straight section of jet vs. (a) the dimensionless flow rate, (b) the dimensionless electric field for different operating parameters. Each color/symbol represents the wt% of a given polymer in distilled water. Four data values for each color/symbol represent different process parameters. Different symbol represents a different dimensionless axial length, written in brackets. Literature data correspond to the symbols against the legend placed inside the box.

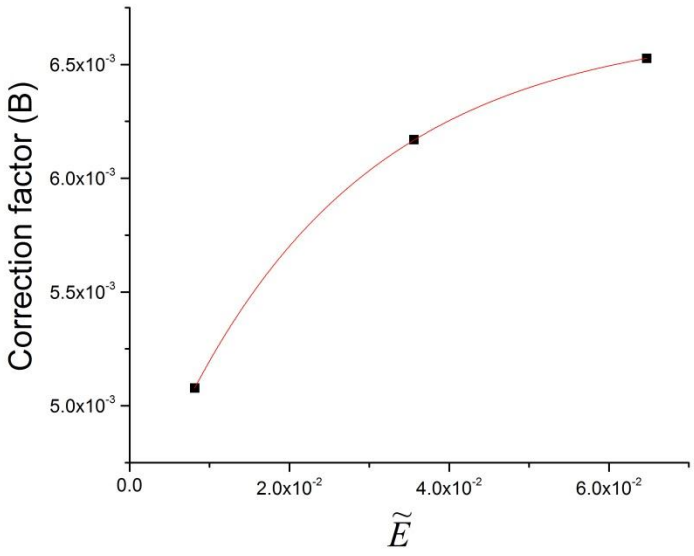

Figure 3.6 The correction factor as a function of dimensionless electric field.

Removing the logarithm, we obtain the correlation between the combined dimensionless geometric parameter and dimensionless flow rate as:

$$\tilde{d}\tilde{z}^{1/4} = 1.09\tilde{Q}^{1/2}\,. \tag{3.13}$$

The expression is valid for the analyzed range of dimensionless flow rates $\left(2.6 \times 10^{-4} < \tilde{Q} < 3.6 \times 10^{7}\right)$ and dimensionless electric fields $\left(7.4 \times 10^{-4} < \tilde{E} < 1.4 \times 10^{-1}\right)$. Additionally, the correlation formula is valid for the analyzed range of dimensionless number, $3.3 \times 10^{-7} < De_{r_o} < 3.8 \times 10^{-2}$, $5.8 \times 10^{-4} < Re_{r_o} < 7.0 \times 10^{-1}$, $3.3 \times 10^{-4} < De_r < 4.7 \times 10^{4}$ and $2.9 \times 10^{-3} < Re_r < 3.9 \times 10^{1}$. As Equation (3.13) represents a universal correlation formula, we argue that it can be employed to predict the diameter along the straight section of the electrospun jet for various polymer-solvent systems.

To check the validity of the correlation formula for diameter at different locations along the jet's straight section, comparisons are made with the data presented in the literature.

The data compared with the proposed correlation formula include 2 and 4 wt% PEO (M_w = 900,000) water solution. This comparison was possible as the diameter of the electrospun jet has reached asymptotic relationship with the axial length $\left(\tilde{d} \sim \tilde{z}^{-1/4}\right)$. Nevertheless, the other literature data compared to the diameter at the apex of the Taylor cone cannot be compared as asymptotic regime $\left(\tilde{d} \sim \tilde{z}^{-1/4}\right)$ was not reached for the plotted axial length for 15 wt% PMMA (M_w = 70,000) chloroform solution [97] and 6 wt% PEO (M_w = 900,000) water solution [86], 6 wt% PEO (M_w = 400,000) water solution [30] and 5 wt% PEO (M_w = 600,000) water solution [97]. The literature data were found to compare well with the correlation formula related to the diameter at different locations along the jet's straight section. The literature data also helped in extending range of dimensionless parameters under which the proposed correlation formula is valid. Therefore, the correlation formula for the diameter at different locations along the jet's straight section is valid for the given range of dimensionless flow rates $\left(2.6 \times 10^{-4} < \tilde{Q} < 5.9 \times 10^{7}\right)$ and dimensionless electric fields $\left(5.6 \times 10^{-4} < \tilde{E} < 1.4 \times 10^{-1}\right)$. Additionally, the correlation formula is valid for the analyzed range of dimensionless numbers, $3.3 \times 10^{-7} < De_{r_o} < 3.8 \times 10^{-2}$ and $2.0 \times 10^{-4} < Re_{r_o} < 7.0 \times 10^{-1}$.

3.5 Conclusion

Four independent dimensionless parameters, namely dimensionless electric field $\tilde{E}$, flow rate $\tilde{Q}$, axial length $\tilde{z}$, and diameter of the electrospun jet $\tilde{d}$ were found to govern the characteristics of the straight section of the electrospun jet. Subsequently, the two geometric dimensionless parameters $\left(\tilde{d}, \tilde{z}\right)$ were combined to obtain a three-parameter system. Subsequently correlation formulae with/without the influence of electrical parameter $\tilde{E}$ were

devised. Finally, the analysis was reduced to a two-parameter-correlation formula $\left(\tilde{d}\tilde{z}^{1/4} = 1.09\tilde{Q}^{1/2}\right)$ after ignoring the weak $\tilde{E}$ effect. The correlation formula is valid for the analyzed range of dimensionless flow rates $\left(2.6 \times 10^{-4} < \tilde{Q} < 3.6 \times 10^{7}\right)$ and dimensionless electric fields $\left(7.4 \times 10^{-4} < \tilde{E} < 1.4 \times 10^{-1}\right)$. Additionally, the correlation formula is valid for the analyzed range of dimensionless numbers; $3.3 \times 10^{-7} < De_{r_o} < 3.8 \times 10^{-2}$, $5.8 \times 10^{-4} < Re_{r_o} < 7.0 \times 10^{-1}$, $3.3 \times 10^{-4} < De_r < 4.7 \times 10^{4}$ and $2.9 \times 10^{-3} < Re_r < 3.9 \times 10^{1}$. The validity of the correlation formula was further increased with the help of literature data. Therefore, the correlation formula for the diameter at different locations along the jet's straight section is valid for the given range of dimensionless flow rates $\left(2.6 \times 10^{-4} < \tilde{Q} < 5.9 \times 10^{7}\right)$ and dimensionless electric fields $\left(5.6 \times 10^{-4} < \tilde{E} < 1.4 \times 10^{-1}\right)$ and dimensionless numbers, $3.3 \times 10^{-7} < De_{r_o} < 3.8 \times 10^{-2}$ and $2.0 \times 10^{-4} < Re_{r_o} < 7.0 \times 10^{-1}$.

The obtained values of the jet diameter against the given flow rate and axial distance can be used to obtain jet characteristics for any given polymer-solvent system. Additionally, the obtained characteristics of the jet's straight section may help to obtain the desired final microfiber morphology by varying the nozzle to collector distance. Therefore, it is intended that the obtained correlation formula will be instrumental in the design as well as controlled manipulation of the electrospinning phenomenon.

Chapter 4 Bending instability experienced by the electrospun jet

4.1 Introduction

This chapter covers the bending instability experienced by the electrospun jet. In section 4.2, the principle and the process pertaining to the occurrence of bending instability is compiled. In section 4.3, dimensional analysis pertaining to the length of the straight section of the electrospun jet before the initiation of bending instability is performed to obtain a correlation formula. In section 4.4, experimental parameters and material employed for analyzing bending instability are presented. In the section 4.5, analysis of the bending instability experienced by the electrospun jet is performed. Parameters such as dimensionless wavelength, growth rate and the phase velocity are calculated against the dimensionless process parameters. In section 4.6, the failure modes of the electrospun jet during bending instability are analyzed. Finally, results are summarized in section 4.7.

4.2 Electrospun jet trajectory

As mentioned, at a critical applied electric field strength, the forces due to electric field overcomes the forces due to surface tension at the tip of the Taylor cone resulting in a single jet from the apex as shown in Figure 4.1. The electrified jet traverses a straight-line path before experiencing bending instability [24, 27]. This instability results in curling and spiraling path responsible for the stretching of the jet as observed in Figure 4.1. During its curling and spiraling motion, the jet in each subsequent loop grows longer and thinner with the increase in loop diameter and circumference.

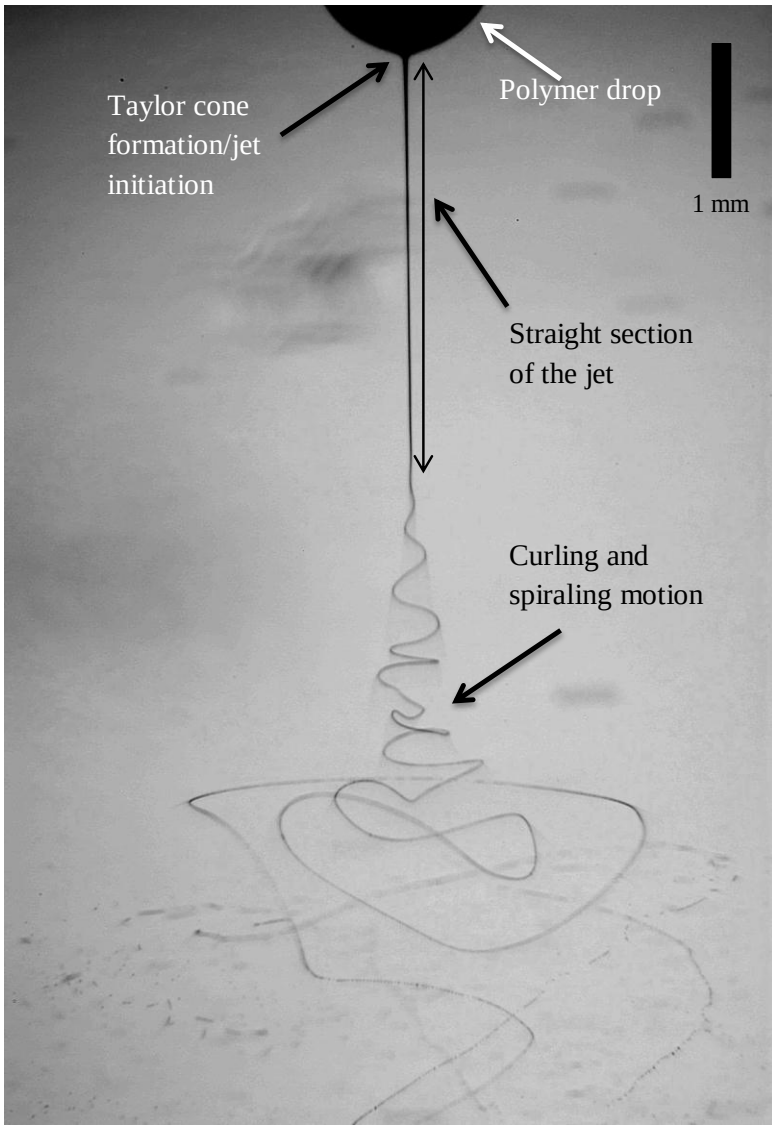

Figure 4.1 Liquid polymeric jet emerging from an electrified drop at electric field strength (flow rate) of 83.50 kV/m (0.095 ml/min). The polymer solution used was 0.125 wt% PEO (M_w = 400,000) dissolved in distilled water.

The elongation and the associated thinning usually continue as long as the free charges on the jet supply enough Coulomb force for the stretching of the electrospun jet. Eventually, the jet solidifies and results in the production of nanofibers. The aim of this chapter is to systematically analyze this bending instability experienced by the electrospun jet.

4.3 Dimensional analysis pertaining to the length of the straight section of the jet

The length of straight section Z_{in} is defined from the apex of the Taylor cone to the initiation of bending instability. The apex of the Taylor is defined as the point of maximum curvature. During the analysis for the diameter at the apex of the Taylor cone, the diameter was measured at the point of maximum curvature, which corresponds to $z = 0$. Therefore, the length of straight section is measured from the point of maximum curvature to the point where the jet starts to bend after following a straight-line trajectory. Therefore Z_{in} is independent of jet diameter d and axial location z. Therefore, the parametric equation governing Z_{in} is given as:

$$Z_{\text{in}} = f(\gamma, \eta_e, K, \varepsilon, E, Q). \tag{4.1}$$

Dimensional analysis yields

$$\frac{Z_{\text{in}}\eta_e K}{\gamma\varepsilon} = f\left(\frac{E\varepsilon}{(\eta_e K)^{1/2}}, \frac{Q{\eta_e}^3 K^2}{\gamma^3 \varepsilon^2}\right), \tag{4.2}$$

where dimensionless length of the straight section of the electrospun jet $\left(\widetilde{Z_{\text{in}}} \equiv \frac{Z_{\text{in}}\eta_e K}{\gamma\varepsilon}\right)$, as a function of dimensionless flow rate $\left(\tilde{Q} \equiv \frac{Q{\eta_e}^3 K^2}{\gamma^3 \varepsilon^2}\right)$, and dimensionless electric field $\left(\tilde{E} \equiv \frac{E\varepsilon}{(\eta_e K)^{1/2}}\right)$ was depicted in Equation (4.2) and shown in Figure 4.2. Figure 4.2 (a) shows that the length of the straight section $\widetilde{Z_{\text{in}}}$ is a very strong function of the dimensionless flow rate $\tilde{Q}$ and rather weak function of dimensionless electric field $\tilde{E}$. Figure 4.2 (b) depicts the relationship between the dimensionless length of the straight section $\widetilde{Z_{\text{in}}}$ and dimensionless electric field $\tilde{E}$ for constant values of polymer solution concentrations. Figure 4.2 (b) shows

that there is overlapping of data points corresponding to the constant dimensionless electric field, which are depicted by vertical dashed lines. Subsequently, these constant dimensionless electric field lines were plotted as three red/solid lines in Figure 4.2 (a). Similar to the analysis previously performed, the slopes of these three parallel dimensionless electric field lines is 0.40, but with slightly different vertical intercepts log(*B*). Therefore, the dimensionless length of the straight section $\widetilde{Z_{\text{in}}}$ can be expressed in terms of dimensionless flow rate $\widetilde{Q}$ given by Equation (4.3).

$$\log\left(\frac{Z_{\text{in}}\eta_e K}{\gamma\varepsilon}\right) = m \times \log\left(\frac{Q{\eta_e}^3 K^2}{\gamma^3\varepsilon^2}\right) + \log(B). \tag{4.3}$$

Equation (4.3) incorporates the effect of dimensionless electric field in slope *m* equal to 0.40 and intercept log(*B*) as the correction factor as shown in Figure 4.3. Similar to the previous analysis, for small or negligible dimensionless electric field effect, a three-parameter system was reduced to a two-parameter system depicted in Equation (4.4).

$$\log\left(\frac{Z_{\text{in}}\eta_e K}{\gamma\varepsilon}\right) = m \times \log\left(\frac{Q{\eta_e}^3 K^2}{\gamma^3\varepsilon^2}\right) + \log(A). \tag{4.4}$$

The data values in Figure 4.2 (a) were found to collapse on a straight line with the best-fit line having a slope *m* equal to 0.42, and the intercept log(*A*) equal to 1.93 for the correlation formula (Equation (4.4)). Removing the logarithm, we obtained the correlation between the dimensionless length of the straight section of the electrospun jet and dimensionless flow rate as:

$$\widetilde{Z_{\text{in}}} = 86\tilde{Q}^{0.42} \tag{4.5}$$

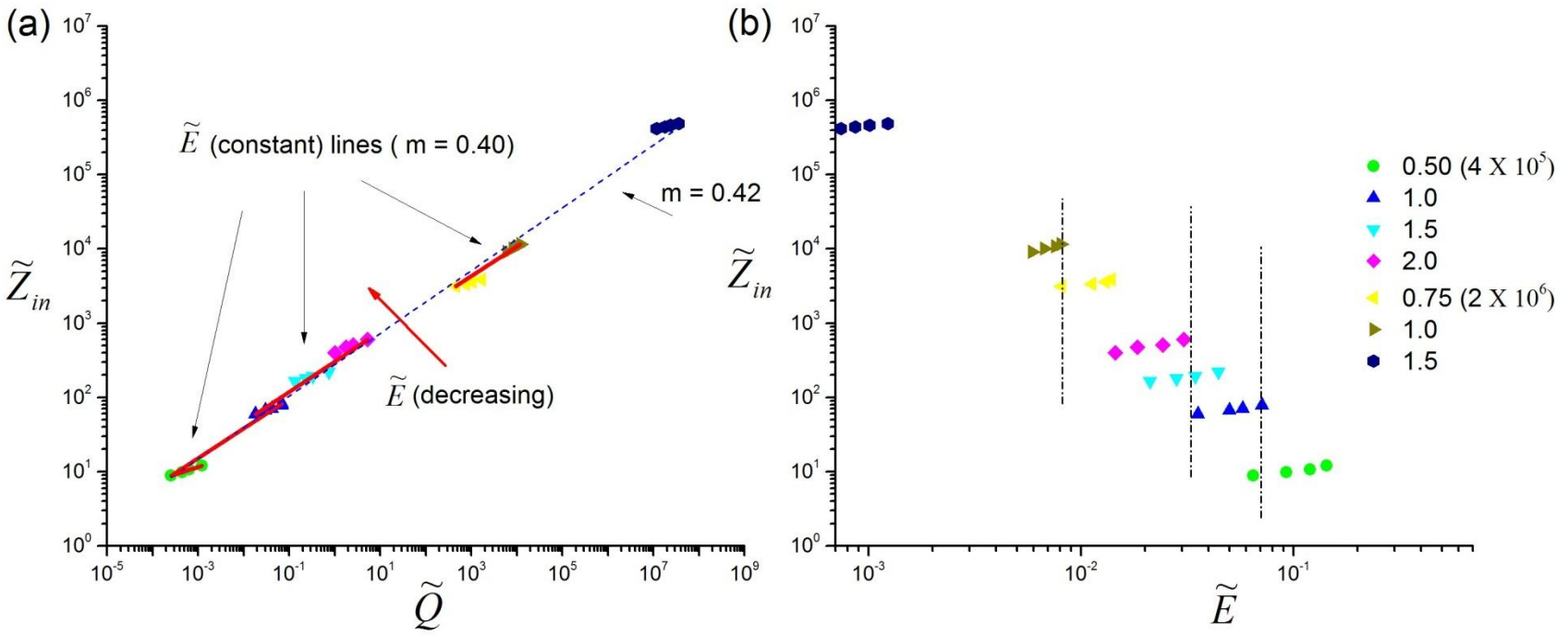

Figure 4.2 Dimensionless length of the straight section of jet vs. (a) the dimensionless flow rate, and (b) the dimensionless electric field for different operating parameters. Each symbol/color represents the wt% of a given polymer in distilled water. The numerical quantity in the bracket represents the molecular weight of the polymer employed. Four data values for each symbol/color represent different process parameters.

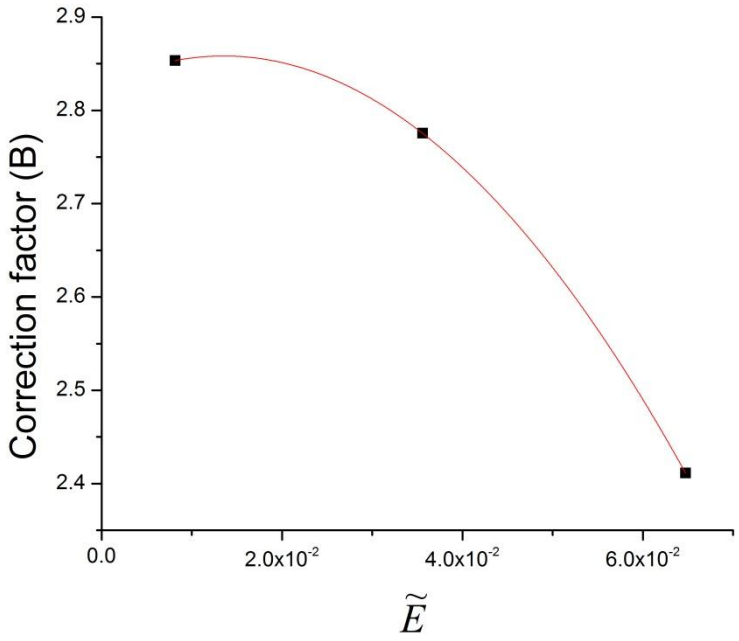

Figure 4.3 The correction factor as a function of dimensionless electric field.

The correlation formula is valid for the analyzed range of dimensionless flow rates $\left(2.6 \times 10^{-4} < \tilde{Q} < 3.6 \times 10^{7}\right)$ and dimensionless electric fields $\left(7.4 \times 10^{-4} < \tilde{E} < 1.4 \times 10^{-1}\right)$. Additionally, the analysis is valid for the analyzed range dimensionless numbers, $3.3 \times 10^{-7} < De_{r_o} < 3.8 \times 10^{-2},\ 5.8 \times 10^{-4} < Re_{r_o} < 7.0 \times 10^{-1},\ 3.3 \times 10^{-4} < De_r < 4.7 \times 10^{4}$ and $2.9 \times 10^{-3} < Re_r < 3.9 \times 10^{1}$. It is argued that Equation (4.5) can be employed to predict the dimensionless length of the straight section of the electrospun jet for the various polymer-solvent systems against the given operating parameters. Furthermore, the predicted dimensionless length of the straight section of the electrospun jet can aid in control and design of the electrospinning setup. For instance, a prior knowledge of $\widetilde{Z_{\text{in}}}$ against given $\widetilde{E}$ and $\widetilde{Q}$ can help in modifying the electrospinning setup to achieve aligned or

patterned fiber structures. This is because knowing $\widetilde{Z_{in}}$, the nozzle to collector distance can be varied in order to suppress bending instability and achieve patterned structures.

During the dimensional analysis, PEO-water solution system was selected as the test system due to the low volatility of water at room temperature, resulting in relatively low evaporation rates as compared to the highly volatile solvents employed in electrospinning. The low evaporation rates results in relatively no variation of material parameters along the straight section of the electrospun jet. Nevertheless, proposed correlation formulae based on experimental data (PEO-water solution) is compared with literature data, which include PMMA-chloroform solution [97] and PEO-water solutions [30, 86 and 97]. The literature data of different polymer-solvent systems was found to compare well with the correlation formulae related to the straight section of the jet. Thus, the appreciable matching between the analyzed and literature data helps in validating the applicability of these correlation formulae under the assumptions made during the analysis.

4.4 Bending instability experienced by the electrospun jet

Numerous mathematical and experimental results pertaining to the straight section of the electrospun jet are available within the literature, as discussed in section 1.3.2. However, results for bending instability of the electrospun jet are much scarcer. Although numerical analysis of the bending instability has previously been performed, only a few parameters have been analyzed [24, 27]. Here, we present experimental research work to analyze the bending instability experienced by the electrospun jet.

4.4.1 Experimental details pertaining to bending instability

Time resolved imaging of the electrospinning process was performed to gain a better understanding of the underlying phenomenon. The images were obtained through a still camera (NIKON D40X) connected to a long-distance microscopic lens with the electrospinning setup shown in Figure 2.1 (a). The light sources employed consist of stroboscopic lamps connected to the time-delay box. The lighting setup was configured in such a fashion to generate two flashes for a given time interval. This lighting setup was capable of producing flashes with a time difference on the order of 10 μs. Subsequently, the strobe light produced the time-resolved signatures of the electrospun jet on the sensor of the still camera. For particular applied electric field strength, the process was sustained for several minutes to obtain a steady-state condition. A continuous electrospinning process was observed for an extended period. The data obtained was employed for the systematic characterization of bending instability experienced by the electrospun jet for different operating parameters. Parameters such as wavelength, growth rate and the phase velocity of the electrospun jet were analyzed.

Later in its trajectories, the bending and spiraling jet experiences failure modes. To capture these failure modes a High-speed camera (Model: Hitachi-made prototype camera [106]**)** connected to a long-distance microscopic lens was employed. The setup of the electrospinning process employed for the analysis is shown in Figure 2.1 (a). The frame rates used for the analysis ranged from 20,000 to 2,000,000 fps. The outer diameter of the metallic nozzle used for the production of electrospun fibers was 3.35 mm (inner diameter = 3 mm). The phenomenon of the failure of the electrospun jet was observed about 70 to 100 mm away from the tip of the metallic nozzle.

4.4.2 Material preparation

The experimental analysis was performed on 0.75 to 1.5 wt% PEO (M_w = 2,000,000)-water/ethanol solution system at varying process parameters, which was accurately measured in the narrow imaging window of the experimental setup. Initially, experiments were performed on 0.5 to 2 wt% PEO (M_w = 400,000, 900,000) - water/ethanol solutions. It was noticed that fiber diameter was too small to be accurately digitized with the help of general thresholding. This required the preparation of the polymer solutions producing jet radius thick enough to be accurately digitized. After a number of iterations, the curling and spiraling phenomenon was experimentally visualized for 0.75 to 1.5 wt% PEO (M_w = 2,000,000) - water/ethanol solution system to gather the bending profile of the jet.

4.5 Analysis of the bending instability experienced by the electrospun jet

During bending instability, as the jet traverses along its curling and spiraling motion, it suffers from linear as well as non-linear instabilities. It was observed that as the jet curls and spirals away from the nozzle, nonlinear instability became dominant. It was observed from the experimental data that jet suffers from the linear instability close to the initiation of curling and spiraling motion. Therefore, the linear instability analysis was performed to characterize bending instability. For the linear instability analysis, the first characteristic bending wave was considered as the representative wave.

The coordinate values (x, y) against the characteristic bending wave for different operating parameters were obtained from the experimental data as depicted in Figure 4.4. The images shown in Figure 4.4 are sufficiently sharp that the coordinate values against characteristic bending wave can be extracted. The coordinate values (x, y) were digitized

through a code written in Matlab®. The digitized coordinates obtained from a set of 50 images at a particular operating condition were numerically fitted to a representative bending wave profile given by Equation (4.6) to calculate the relevant parameters.

$$y = Ae^{\alpha x}\cos(2\pi x/\lambda_{in}). \tag{4.6}$$

Equation (4.6) depicts a representative-bending wave with exponentially increasing amplitude. The relevant parameters calculated numerically from Equation (4.6) are growth rate (α), wavelength (λ_{in}) and amplitude (A) of the characteristic bending wave. The phase velocity (v_p) of the electrospun jet was experimentally quantified by monitoring the movement of maxima or minima for a certain time difference, as shown in Figure 4.4. The distance between two corresponding maxima is depicted in Figure 4.4 (for instance, by Δx). When Δx is divided by the time difference between two instances of the electrospun jet, the average phase velocity is estimated. The repeatability of the data was checked by performing experiments at a regular interval of time in the same controlled laboratory environment. The variation in the absolute value of parameters was found to be about 10% in all the cases.

Later, these parameters $(\alpha, \lambda_{in}$ and $v_p)$ were non-dimensionalized with the length and velocity scale obtained for the straight section of the electrospun jet. The choice of length and velocity scale is reasonable as we are working with first characteristic bending wave close to the end of the straight section of the electrospun jet. Later, these dimensionless parameters were plotted against the dimensionless flow rate and the electric field. The dimensionless flow rate $\left(\frac{Q\eta_e{}^3K^2}{\gamma^3\varepsilon^2}\right)$ and the electric field $\left(\frac{E\varepsilon}{(\eta_e K)^{1/2}}\right)$ are also the same as those obtained for the straight section of the electrospun jet.

.

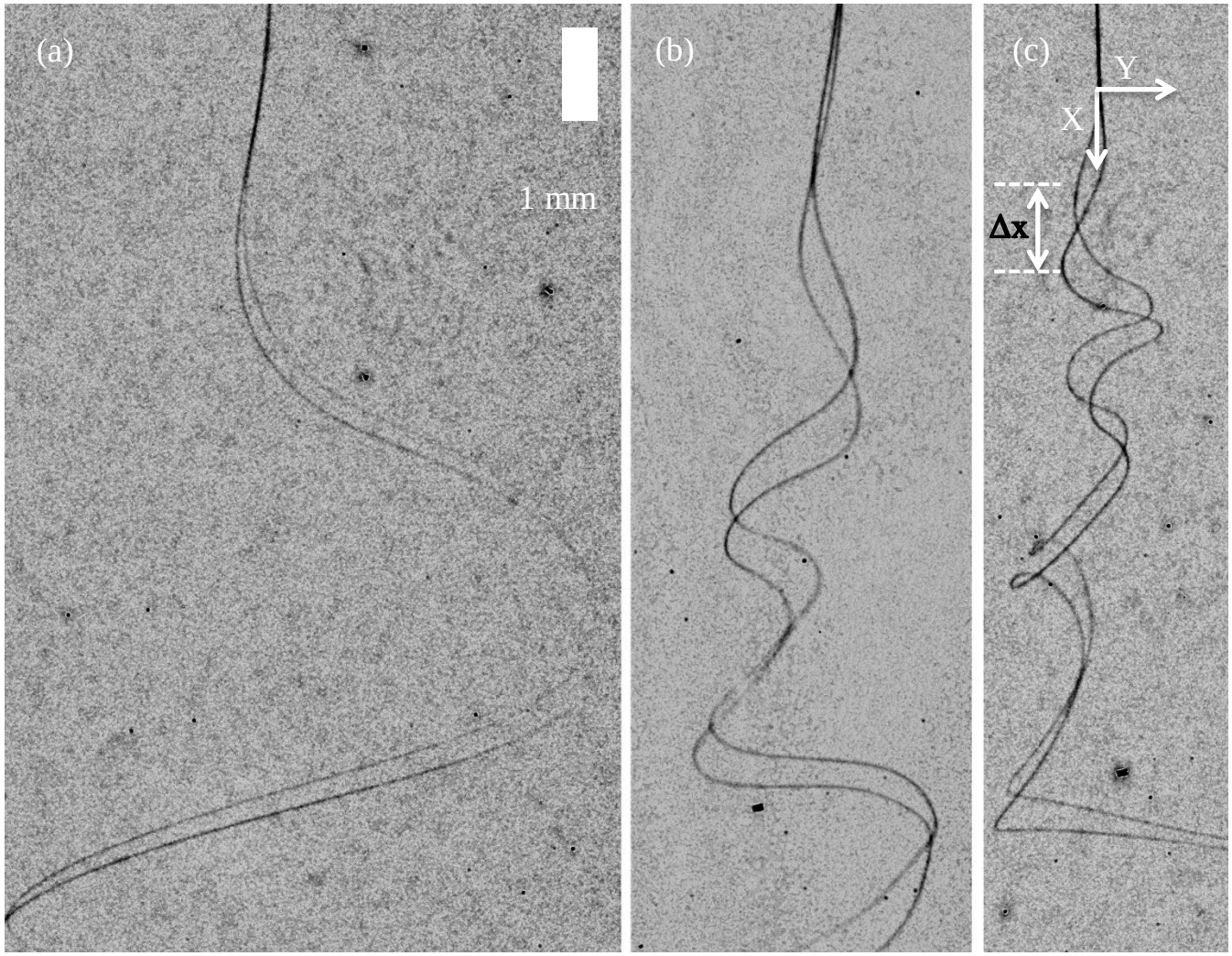

Figure 4.4 Two instances of the electrospun jet. The polymer solution employed was 0.75 w% aqueous PEO (M_w = 2,000,000) solution. The process parameters are applied voltage (flow rate, time difference), (a) 41.75 (0.02, 100), (b) 57.91 (0.035, 100), and (c) 76.76 kV/m (0.11 ml/min, 100 μs).

The length scale used is $\left(\frac{\gamma\varepsilon}{\eta_e K}\right)$, obtained for straight section of the electrospun jet. The velocity scale is obtained by dividing flow rate scale $\left(\frac{\gamma^3\varepsilon^2}{{\eta_e}^3K^2}\right)$ with square of the length scale $\left(\frac{\gamma\varepsilon}{\eta_e K}\right)$, resulting in $\left(\frac{\gamma}{\eta_e}\right)$. Later, this velocity scale was employed to non-dimensionalize the phase velocity. Subsequently, these dimensionless parameters as a function of the dimensionless process parameters are plotted and discussed in subsequent sections

4.5.1 Characteristic wavelength of linear instability

The dimensionless wavelength $\left(\frac{\lambda_{in}\eta_e K}{\gamma\varepsilon}\right)$ is plotted against dimensionless flow rate $\left(\frac{Q{\eta_e}^3K^2}{\gamma^3\varepsilon^2}\right)$, and dimensionless electric field $\left(\frac{E\varepsilon}{(\eta_e K)^{1/2}}\right)$, presented in Figure 4.5 (a and b), respectively. The relationship of dimensionless wavelength with the process parameters is depicted in Equation (4.7). In Figure 4.5, each color/symbol represents the wt% of a given polymer in the solvent mixture. Three data values for each color/symbol represent different process parameters. For a particular experimental case, a certain fraction (80/20) represents a water/ethanol mixture by volume as the solvent. For the rest of the experimental case, pure distilled water is used as the solvent.

$$\frac{\lambda_{in}\eta_e K}{\gamma\varepsilon} = f\left(\frac{E\varepsilon}{(\eta_e K)^{1/2}}, \frac{Q{\eta_e}^3K^2}{\gamma^3\varepsilon^2}\right). \tag{4.7}$$

It is clear from Figure 4.5 (a) that the dimensionless wavelength is a strong function of dimensionless electric field and rather weak function of dimensionless flow rate. Similar to the analysis for the straight section, further analysis was performed in order to predict the effect of dimensionless flow rate on dimensionless wavelength.

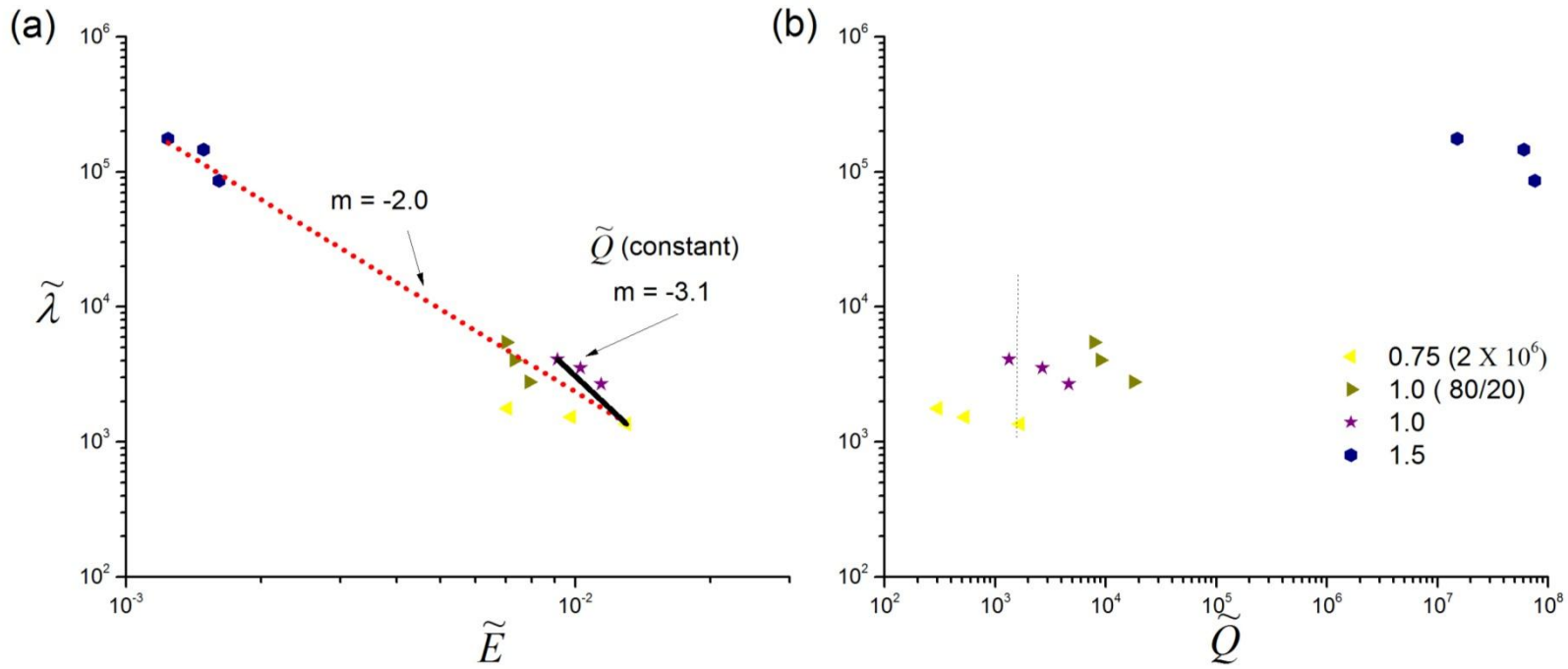

Figure 4.5 Dimensionless wavelength of the linear instability experienced by the electrospun jet vs. (a) the dimensionless electric field, and (b) the dimensionless flow rate for different operating parameters. Each symbol/color represents the wt% of a given polymer dissolved in the solvent mixture. The numerical quantity in the bracket represents the molecular weight of the polymer employed. Three data values for each symbol/color represent different process parameters. Caption (80/20) represents the volume fraction of water/ethanol in the solvent mixture.

Data values corresponding to the constant dimensionless flow rate were obtained, depicted by dashed lines in Figure 4.5 (b). Subsequently, the constant dimensionless flow rate line is plotted as black/solid line in Figure 4.5 (a). The slope of dimensionless flow rate line is -3.1. Therefore, the dimensionless wavelength can be expressed in terms of dimensionless electric field incorporating the effect of dimensionless flow rate as $\widetilde{\lambda_{in}} \sim \left(\tilde{E}\right)^{-3.1}$. The power law relationship between dimensionless wavelength and dimensionless electric field can be expressed as $\widetilde{\lambda_{in}} \sim \left(\tilde{E}\right)^{-2}$, when ignoring the effect of dimensionless flow rate. The power law relationships are valid for the given range of dimensionless flow rates $\left(3.1 \times 10^{2} < \tilde{Q} < 7.6 \times 10^{7}\right)$ and dimensionless electric fields $\left(1.2 \times 10^{-3} < \tilde{E} < 1.3 \times 10^{-2}\right)$.

4.5.2 Characteristic growth rate of the amplitude of linear instability

Similar to the analysis for dimensionless wavelength, the dimensionless growth rate is correlated with the dimensionless flow rate and electric field depicted by Equation (4.8).

$$\frac{\alpha\gamma\varepsilon}{\eta_e K} = f\left(\frac{E\varepsilon}{(\eta_e K)^{1/2}}, \frac{Q{\eta_e}^3 K^2}{\gamma^3 \varepsilon^2}\right), \tag{4.8}$$

where, dimensionless growth rate $\left(\frac{\alpha\gamma\varepsilon}{\eta_e K}\right)$ obtained for the characteristic bending wave is plotted against dimensionless flow rate $\left(\frac{Q{\eta_e}^3 K^2}{\gamma^3 \varepsilon^2}\right)$, and dimensionless electric field $\left(\frac{E\varepsilon}{(\eta_e K)^{1/2}}\right)$ in Figure 4.6. It is inferred from Figure 4.6 that the dimensionless growth rate generally decreases with an increase in the dimensionless flow rate. Similar to the analysis presented for the dimensionless wavelength, the dimensionless growth rate can be expressed in a power law relationship with the dimensionless flow rate.

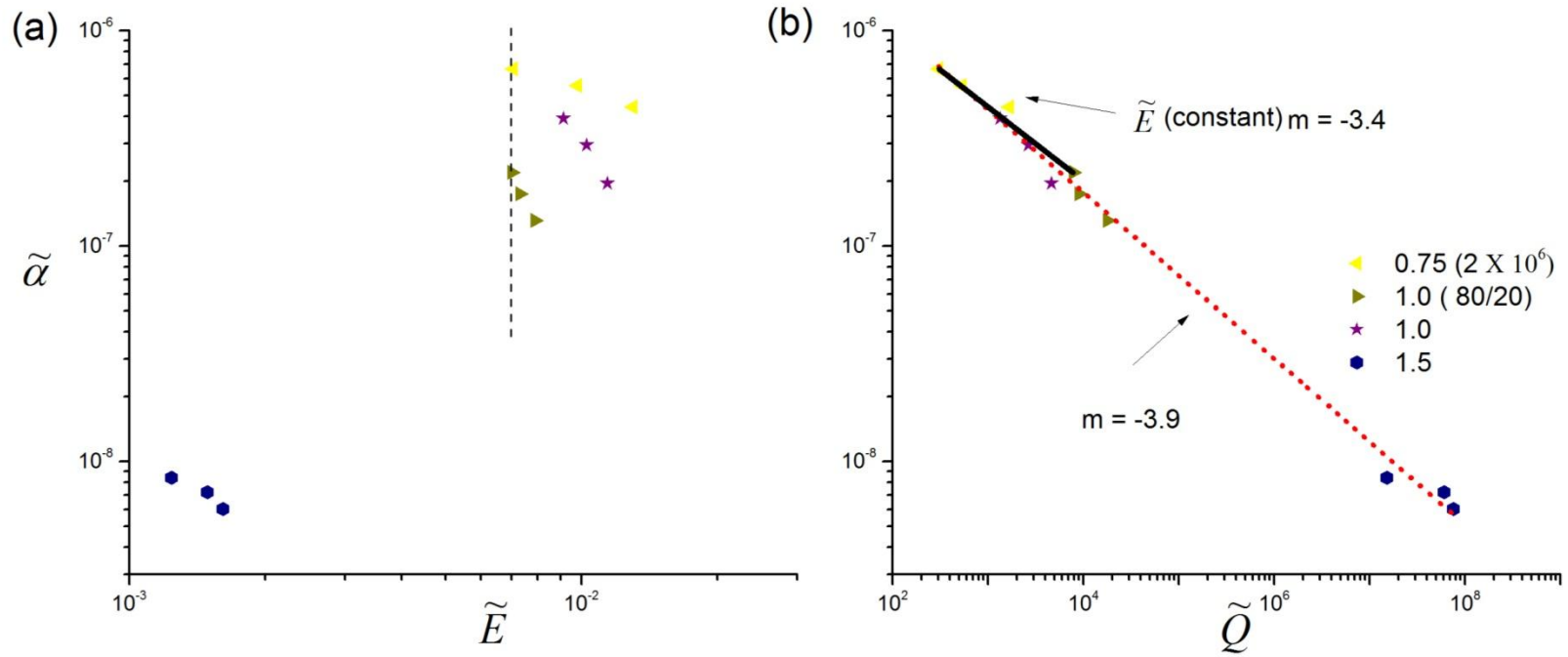

Figure 4.6 Growth rate of the linear instability experienced by the electrospun jet vs. (a) the dimensionless electric field, and (b) the dimensionless flow rate for different operating parameters. Each symbol/color represents the wt% of a given polymer dissolved in the solvent mixture. The numerical quantity in the bracket represents the molecular weight of the polymer employed. Three data values for each symbol/color represent different process parameters. Caption (80/20) represents the volume fraction of water/ethanol in the solvent mixture.

The slope of the constant dimensionless electric field line is -3.4, shown in Figure 4.6 (b). Therefore, the dimensionless growth rate can be expressed in terms of dimensionless flow rate incorporating the effect of dimensionless electric field as $\tilde{\alpha} \sim \left(\tilde{Q}\right)^{-3.4}$. The power law relationship between dimensionless growth rate and dimensionless flow rate can be expressed as $\tilde{\alpha} \sim \left(\tilde{Q}\right)^{-3.9}$, when ignoring the effect of the dimensionless electric field. The power law relationships are valid for the given range of dimensionless flow rates $\left(3.1 \times 10^{2} < \tilde{Q} < 7.6 \times 10^{7}\right)$ and dimensionless electric fields $\left(1.2 \times 10^{-3} < \tilde{E} < 1.3 \times 10^{-2}\right)$.

4.5.3 Characteristic phase velocity of linear instability

The resultant dimensionless phase velocity $\left(\frac{\eta_e v_p}{\gamma}\right)$ is plotted against the dimensionless flow rate $\left(\frac{Q{\eta_e}^3 K^2}{\gamma^3 \varepsilon^2}\right)$ and electric field $\left(\frac{E\varepsilon}{(\eta_e K)^{1/2}}\right)$ shown in Figure 4.7 and depicted in Equation (4.9).

$$\frac{\eta_e v_p}{\gamma} = f\left(\frac{E\varepsilon}{(\eta_e K)^{1/2}}, \frac{Q{\eta_e}^3 K^2}{\gamma^3 \varepsilon^2}\right). \tag{4.9}$$

It can be seen from Figure 4.7 (b) that dimensionless phase velocity increases with the increase in the dimensionless flow rate, depicting a strong relationship. The effect of dimensionless electric field on dimensionless phase velocity was predicted with the help of Figure 4.7 (a). Data values corresponding to the constant dimensionless electric field are obtained, depicted by dashed lines in Figure 4.7 (a). Later, the constant dimensionless electric field lines are plotted in Figure 4.7 (b). The slope of parallel dimensionless electric field lines is 0.26.

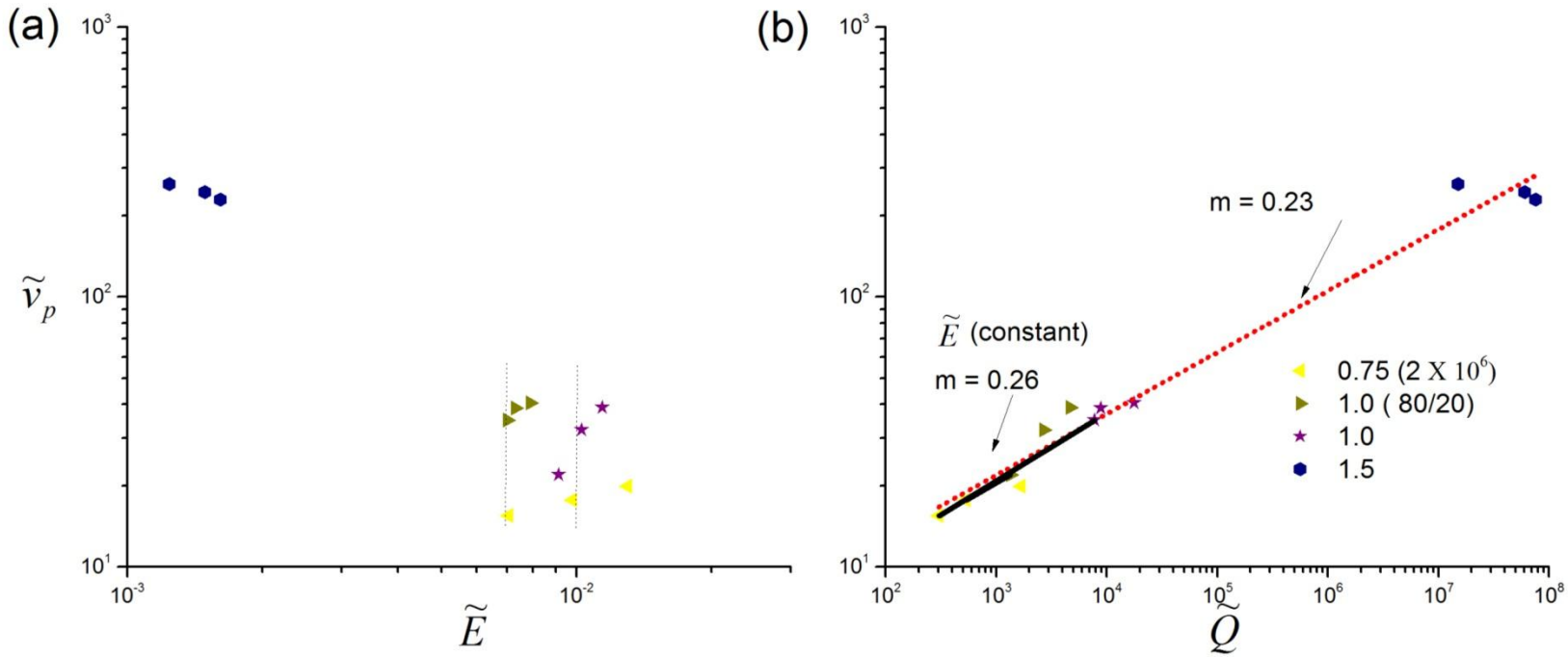

Figure 4.7 Phase velocity of the linear instability underwent by the electrospun jet vs. (a) the dimensionless electric field, and (b) the dimensionless flow rate for different operating parameters. Each symbol/color represents the wt% of a given polymer dissolved in the solvent mixture. The numerical quantity in the bracket represents the molecular weight of the polymer employed. Three data values for each symbol/color represent different process parameters. Caption (80/20) represents the volume fraction of water/ethanol in the solvent mixture.

Therefore, the dimensionless phase velocity is expressed in terms of dimensionless flow rate incorporating the effect of dimensionless electric field as $\widetilde{v_p} \sim \left(\tilde{Q}\right)^{0.26}$. The power law relationship between dimensionless phase velocity and dimensionless flow rate can be expressed as $\widetilde{v_p} \sim \left(\tilde{Q}\right)^{0.23}$, when ignoring the effect of the dimensionless electric field. The power law relationships are valid for the given range of dimensionless flow rates $\left(3.1 \times 10^2 < \tilde{Q} < 7.6 \times 10^7\right)$ and dimensionless electric fields $\left(1.2 \times 10^{-3} < \tilde{E} < 1.3 \times 10^{-2}\right)$. The analysis is valid for the given range of dimensionless numbers. The range of Deborah number $\left(De_{r_o} = \frac{\tau_p Q}{\pi {r_o}^3}\right)$ and Reynolds number $\left(Re_{r_o} = \frac{2\rho Q}{\pi r_o \eta_e}\right)$ based on nozzle radius (r_o) is $1.6 \times 10^{-3} < De_{r_o} < 3.8 \times 10^{-2}$ and $5.8 \times 10^{-4} < Re_{r_o} < 1.2 \times 10^{-2}$, respectively. The obtained characteristic parameters governing the linear instability experienced by the electrospun jet will help in the control and optimization of the electrospinning phenomenon.

4.6 Failure modes of the electrospun jet

The electrospun jet as an entity experiences several instabilities along its trajectory. These instabilities include axisymmetric conducting and non-axisymmetric conducting instabilities as well as axisymmetric non-conducting instability [81, 107]. These conducting instabilities give rise to the bending instability as discussed in the previous sections and result in the reduction of the jet diameter from millimeter at the tip of the metallic nozzle to nanometers, at the collector surface. On the other hand, axisymmetric non-conducting instability better known as capillary instability results in the local increase of the jet diameter. This local increase in the jet diameter is commonly known as bead, which reduces the large surface area of the electrospun fibers and are considered as defects.

4.6.1 Bead formation

The bead formation was found to be responsible for at least two of the failure modes observed during the analysis. It is well known that large surface tension of the aqueous polymer solution is responsible for capillary instability leading to the formation of beads. This local increase in the jet diameter due to the formation of beads can give rise to detached spherical liquid droplets or irregular and undulating morphology with large variations in diameter along the length of the jet [108].

4.6.2 Material parameters affecting morphology of electrospun fibers

It was observed that beads started developing after first few bending waves of the electrospun jet. The location of the occurrence of beads was found to be on the order of 70 mm from the tip of the nozzle. This occurrence of beads close to the collector surface, (i.e. 70 mm from the jet initiation) can be attributed to the dominance of capillary instability. Close to the collector surface, reduction of surface charge density due to the evaporation of the solvent will result in the reduction of the extensional rates endured by the electrospun jet. These relatively low extensional rates will reduce the resultant elastic response of the fluid, which are usually responsible for suppressing capillary instability and thus resulting in the formation of beads and therefore non-uniform fibers.

Further, it is argued that for the given process parameters, the material parameters such as viscosity, surface tension, conductivity, and elasticity of the polymer solution can determine the final morphology of the electrospun nanofibers. Subsequently, the analysis of these material parameters can help to characterize the lower limit of polymer concentration

for defect-free fibers against the given process parameters. Therefore, a qualitative analysis of these material parameters against the electrospun fiber morphology was performed.

The bead formation can be avoided by employing a viscous polymer solution. It is noted that for a highly viscous polymer solution, sufficient viscoelasticity result in the thickening of the electrospun jet. The thick electrospun jet results in regular, cylindrical morphology with a larger and uniform diameter [88]. This implies that an increase in the viscosity of the polymer solution will help in suppression or even complete elimination of beads. The viscosity of the polymer solution can be increased either by increasing the concentration of polymer solution or by increasing the molecular weight of the polymer employed. The change from non-uniform to smooth nanofiber with increasing polymer solution viscosity has previously been documented [109-112].

The conductivity plays an important role in defining the stability of the electrospun jet along its trajectory. Large conductivity with relatively low process parameters (applied electric field strength and flow rate) may result in the formation of non-uniform defective nanofibers. This is possible because relatively low process parameters for large conductivity of the polymer solution will result in less stretching of the jet and therefore may augments capillary instability. The other relevant parameter is the elasticity of the polymer solution. Yu et al. [83] investigated the role of fluid elasticity in the formation of fibers from a polymer solution by electrospinning. Model solutions with different degrees of elasticity were prepared with all the parameters kept constant. The formation of beads-on-string and uniform fiber morphologies during electrospinning was observed for a series of solutions having the same surface tension, zero shear viscosity, and conductivity but different degrees

of elasticity. A high degree of elasticity was found to arrest the breakup of the jet into droplets by the capillary instability and in some cases suppress the instability altogether.

It was documented that the large surface tension of the solvent plays a vital role for the occurrence of these failure modes. Various surfactants were employed to reduce the surface tension of the polymer solution. Fong et al. [88] decreased the surface tension of polymer solution with the addition of ethanol in the solvent mixture. It was observed that decreasing the surface tension of polymer solution resulted in beads-free nanofibers.

4.6.3 Visualization and analysis of failure modes

It was noted that bead formation was responsible for the failure of the electrospun jet later in its trajectory. The first failure mode is represented by a 'beads-on-string' structure shown in Figure 4.8. As the polymer jet moves along its trajectory, it starts to neck on both sides of the bead as depicted by the arrowhead in Figure 4.8 until they fragment down into polymer filament and bead as separate identities. The axisymmetric pinch-off is always observed in the capillary breakup during dripping of a low-viscosity fluid, but in electrospinning, as polymer chains are stretched, the finite extensibility will dictate the thinning dynamics in the last stages of the necking [113]. These extensional stresses generated in the neck region can lead to the formation of very thin and stable filaments between beads resulting in ‘beads-on-string’ structure. The obtained fragmented fibers may also contain thin fibrous structure at their tip due to the phenomenon of necking as also documented by Zussman et al. [114].

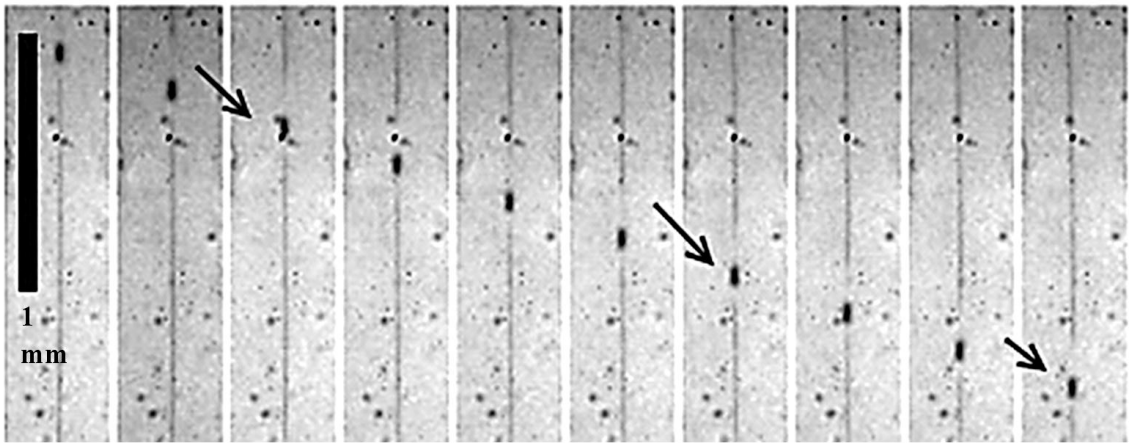

Figure 4.8 Formation of 'beads-on-string' structure. The polymer solution employed was 2.5 wt% PEO (M_w = 900,000) dissolved in distilled water electrospun at 64.76 kV/m. The flow rate was 0.038 ml/min. Arrows points to the bead connected by thin filaments. The frames shown are 50 μs apart.

The second failure mode of an electrospun jet is the formation of a string of beads connected by a fibrous structure shown in Figure 4.9. The large number of beads in close proximity is found to be the direct consequence of the low concentration of polymer solution. It was noted that concentration reduces from 2.5 to 1.5 wt% for the flow phenomenon depicted in Figure 4.8 and Figure 4.9. This low concentration result in an increase in the surface tension, which results in the formation of numerous beads in close proximity. Later, in its trajectory, the thin ligament connecting the beads will stretch under the action of inertia and applied electric field resulting in beads and fiber ligaments as separate identities.

The third mode is the breakup of jet by itself along its trajectory without an apparent increase in its local diameter. Along jets' trajectory, it breaks down into three sections connected with a thin fibrous structure as shown in Figure 4.10.

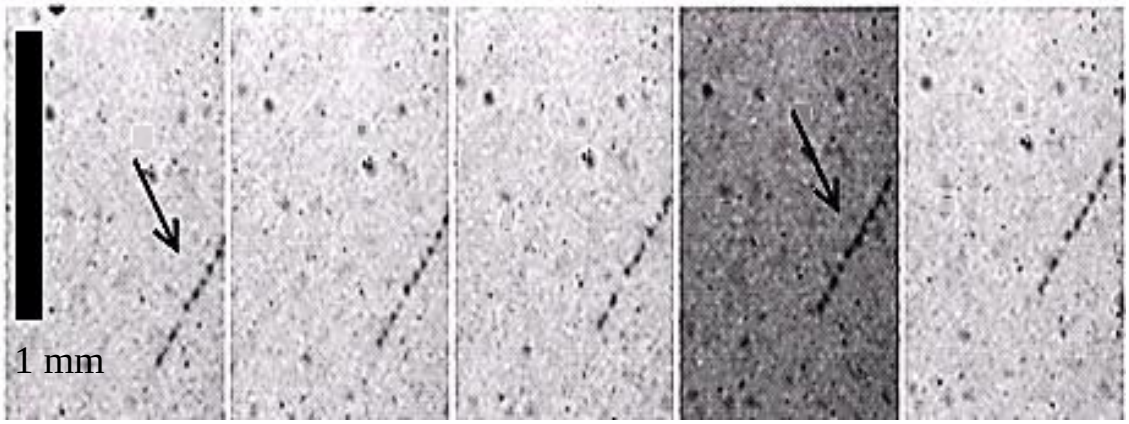

Figure 4.9 Formation of string of beads connected by a fibrous structure. Polymer solution employed was 1.5 wt% PEO (M_w = 900,000) dissolved in distilled water electrospun at 80.95 kV/m. The flow rate was 0.24 ml/min. Arrows points to the string of beads. The frames shown are 5 μs apart.

This particular failure mode is different from the 'beads-on-string' structure as no apparent increase in the diameter of jet was observed. This lack of alteration in jet diameter implies that surface tension is not the dominating factor during the occurrence of this phenomenon. The lack of viscosity or the chain entanglement was considered responsible for this phenomenon. The chain entanglement is inferior for M_w = 400,000 as compared to M_w = 900,000 or higher molecular weight can be the possible reason for this particular failure mode.

A qualitative analysis was presented to provide the reasons for the failure modes visible during electrospinning. In the next sub-section, a correlation formula is presented to devise conditions for the production of uniform fibers.

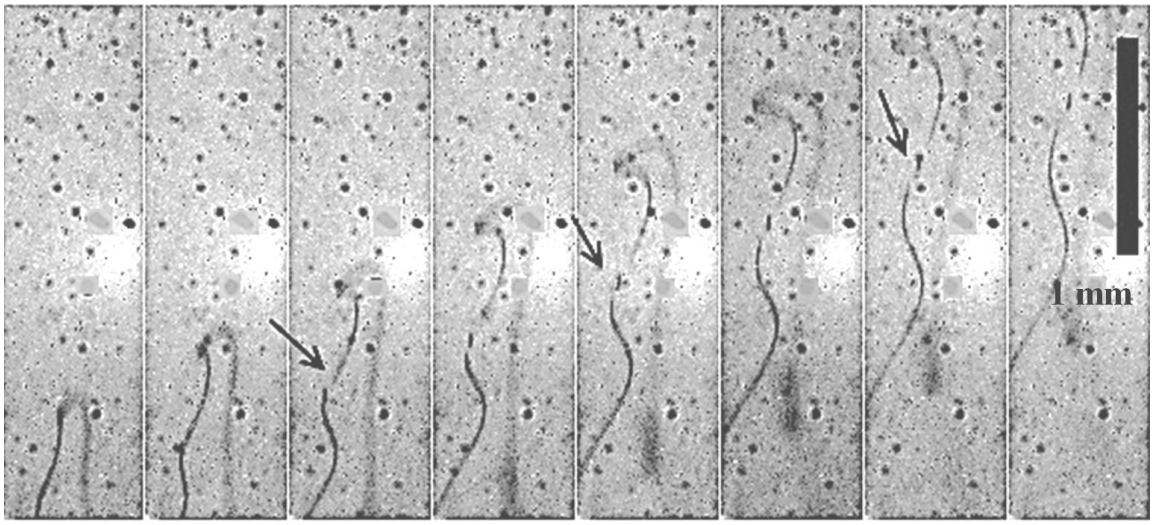

Figure 4.10 The breakup of electrospun jet due to the lack of viscosity. Polymer solution employed was 2.5 wt% PEO (M_w = 400,000) dissolved in distilled water electrospun at 66.67 kV/m. The volumetric flow rate was 0.024 ml/min. Arrows points to the breakup of electrospun jet. The frames shown are 50 μs apart.

4.6.4 Correlation formula for uniform nanofibers

Analysis of the axisymmetric instability experienced by the electrospun jet is performed by outlining the characteristic timescales. These characteristic timescales define the growth rate of the instability relevant to the problem. The relative balance of these timescales was represented in terms of the dimensionless 'correlation formula.' The timescale governing axisymmetric instability of the polymer jet are the polymer relaxation time $\tau_p = \frac{\eta}{G}$, viscous timescale $\tau_{vis} = \frac{\eta r_0}{\gamma}$, and capillary timescale $\tau_\gamma = \sqrt{\frac{\rho {r_0}^3}{\gamma}}$. Therefore, dimensionless parameters obtained from these timescales are Ohnesorge number and Deborah number. Here, Ohnesorge number can be considered as the ratio of viscous and capillary timescale, given by $\left(Oh = \frac{\eta}{(\rho\gamma r_0)^{1/2}}\right)$. Similarly, Deborah number can be considered as the ratio of the polymeric relaxation time (τ_p) to the Capillary timescale, given by $\left(De = \frac{\tau_p}{\sqrt{\rho {r_0}^3/\gamma}}\right)$. These

two dimensionless parameters were then employed to define a 'correlation formula' for the electrospinning process shown in Figure 4.11.

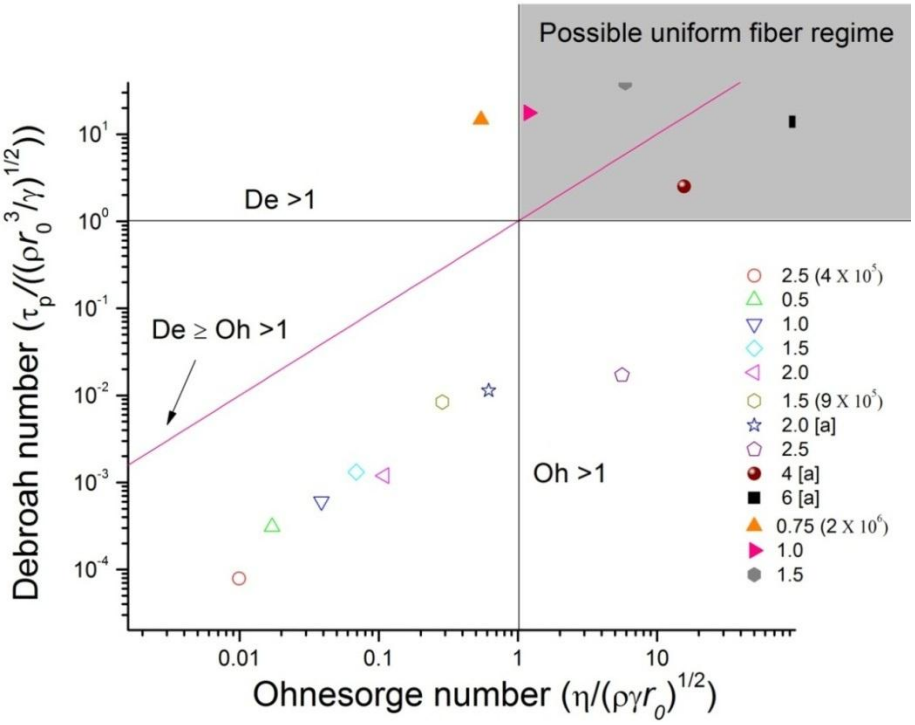

Figure 4.11 Debroah number vs. Ohnesorge number for electrospinning. Solid symbols depict uniform fibers, whereas hollow symbols represent defective fibers. The reference [a] is [86].

In Figure 4.11, solid symbols depict uniform fibers, whereas hollow symbols represent defective fibers. Figure 4.11 depicts that there is a minimum Ohnesorge number ($Oh > 1$) at which electrospun jet can be stabilized. It is clear from Figure 4.11 that non-uniform fibers are more likely the outcome below this limit. A low value of *Oh* implies that viscous forces are insufficient to stabilize capillary waves resulting in truncated nanofibers, 'beads-on-string ' structure, or even electrospraying at sufficiently low *Oh* number.

It was also noted that the polymer solution should have a critical polymer chain entanglement density to avoid beading or non-uniform fibers. This is because critical

polymer chain entanglement is required to provide sufficient elasticity to the polymer jet to arrest capillary instability. Yu et al. [83] studied PEO solutions containing low-molecular weight poly (ethylene glycol) (PEG) and emphasized the role of elasticity of the jet in obtaining uniform fibers. From Figure 4.11, it is clear that Deborah number $(De > 1)$ is required to fabricate uniform fibers. Therefore, the 'possible uniform fiber regime' in Figure 4.11 is represented by $(De > 1)$ and $(Oh > 1)$.

Nevertheless, it has already been mentioned that for electrospinning, the essential requirement for the defect-free nanofibers is $[De \geq Oh > 1]$ [115]. It can be seen from Figure 4.11 that both relationships $[(De > 1)$ and $(Oh > 1)]$ and $[De \geq Oh > 1]$ have few outliners. These outliners can be attributed to large Deborah number or large Ohnesorge number flow regime. Therefore, the data obtained experimentally correlates well with the above-mentioned conditions for the production of defect-free nanofibers as shown in Figure 4.11 with few outliners for both conditions. Consequently, the obtained correlation formula can help to predict the morphology of fiber *a priori*, thus assisting in the control and optimization of electrospinning phenomenon.

4.7 Conclusion

Through dimensional analysis, three dimensionless parameters, namely dimensionless length of the straight section of electrospun jet $(\widetilde{Z_{\text{in}}})$, dimensionless flow rate $(\tilde{Q})$, and dimensionless electric field $(\tilde{E})$ were found to govern the length of the straight section of electrospun jet. Finally, the correlation formula $\left(\widetilde{Z_{\text{in}}} = 86(\tilde{Q})^{0.42}\right)$ for the length of the straight section of electrospun jet, ignoring the weak electric effect was formulated. The

correlation formula is valid for the analyzed range of dimensionless flow rates $\left(2.6 \times 10^{-4} < \tilde{Q} < 3.6 \times 10^{7}\right)$ and dimensionless electric fields $\left(7.4 \times 10^{-4} < \tilde{E} < 1.4 \times 10^{-1}\right)$. Additionally, the analysis is valid for the analyzed range of dimensionless numbers, $3.3 \times 10^{-7} < De_{r_o} < 3.8 \times 10^{-2}$, $5.8 \times 10^{-4} < Re_{r_o} < 7.0 \times 10^{-1}$, $3.3 \times 10^{-4} < De_r < 4.7 \times 10^{4}$ and $2.9 \times 10^{-3} < Re_r < 3.9 \times 10^{1}$.

The predicted dimensionless length of the straight section of the electrospun jet against dimensionless operating parameters can aid in control and design of the electrospinning setup. This is because prior knowledge of $\widetilde{Z_{\text{in}}}$ against the given operating parameters can help in varying nozzle to collector distance in order to suppress bending instability and achieve patterned or aligned structures.

For the analysis of bending instability, the first occurring wave was considered as the 'characteristic bending wave.' This characteristic bending wave was considered representative of the linear instability experienced by the electrospun jet. Parameters such as wavelength, growth rate and the phase velocity were calculated against the dimensionless process parameters to characterize bending instability. The obtained power law relationships for dimensionless wavelength $(\widetilde{\lambda_{in}})$, growth rate $(\tilde{\alpha})$ and the phase velocity $(\widetilde{v_p})$ are $\widetilde{\lambda_{in}} \sim \left(\tilde{E}\right)^{-2}$, $\tilde{\alpha} \sim \left(\tilde{Q}\right)^{-3.9}$, and $\widetilde{v_p} \sim \left(\tilde{Q}\right)^{0.23}$, respectively. The power law relationships are valid for the given range of dimensionless flow rates $\left(3.1 \times 10^{2} < \tilde{Q} < 7.6 \times 10^{7}\right)$ and dimensionless electric fields $\left(1.2 \times 10^{-3} < \tilde{E} < 1.3 \times 10^{-2}\right)$. The analysis is valid for the given range of dimensionless numbers, $1.6 \times 10^{-3} < De_{r_o} < 3.8 \times 10^{-2}$ and $5.8 \times 10^{-4} < Re_{r_o} < 1.2 \times 10^{-2}$.

Failure modes of electrospun jet during bending instability were also investigated. Three failure modes were observed during the analysis. Two of these failure modes were found to be the direct consequence of axisymmetric instability experienced by the electrospun jet. On the other hand, lack of viscosity of the polymer solution and lower polymer chain entanglement was considered responsible for the third mode.

Chapter 5 Branching of an electrospun jet

5.1 Introduction

The chapter covers higher-order instability (branching) experienced by the electrospun jet. In section, 5.2, preliminary remarks regarding the occurrence of higher-order instability are compiled. In section 5.3, surface instabilities experienced by the electrified jet are analyzed to better understand the underlying phenomenon. Emphasis is given to analyze the growth rate of instabilities against viscoelasticity of the polymer jet and applied electric field. In section 5.4, experimental parameters and the conditions required for the initiation of branching are compiled. In section 5.5, linear stability analysis of the electrified jet, including non-Newtonian effects is performed. In section 5.6, comparison is made between the inter-undulation distances obtained experimentally with the theoretically obtained values. The analysis also measures the effect of the relevant dimensionless parameters on the inter-undulation distance. The validity of the theoretical model is checked with the help of experimental data. In section 5.7, the mechanism of the occurrence of branching is analyzed to establish the azimuthal mode $n = 2$ as the dominant mode. In section 5.8, experimental results are reanalyzed against the relevant dimensionless parameters. Finally, concluding remarks are made in section 5.9.

5.2 Preliminary remarks

As explained earlier in chapter 2, when a high electric field is applied to a polymer drop, free and bound charges start to concentrate resulting in their excess buildup on the surface. At some critical value of the applied electric field proposed by Taylor et al. [15], the forces due to applied electric field overcomes the forces due to surface tension and results in jetting

from the polymer drop as was observed during the usual electrospinning process discussed in detail in chapters 2 to 4.

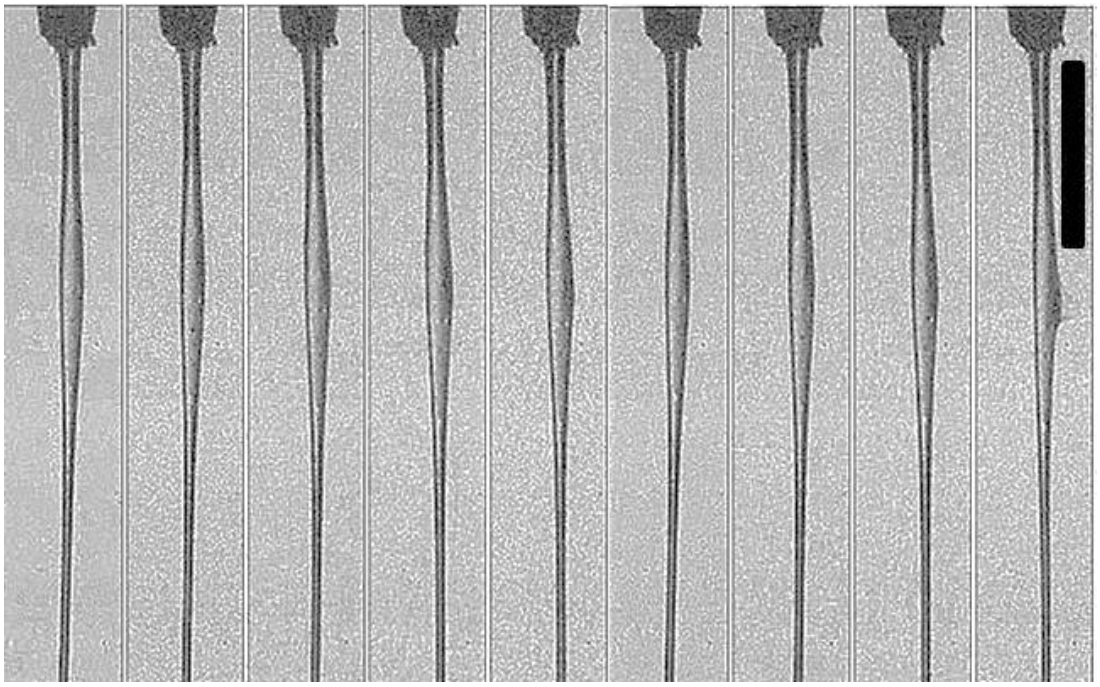

Figure 5.1 The growth of undulation on the electrospun jet. Polymer employed was 6 wt% PEO ($M_w = 400{,}000$) dissolved in 55/45 % v/v ethanol/water solution and the applied field strength was 61.72 kV/m. The time difference between the frames is 10 μs. The scale bar is equal to 0.5 mm.

When the electric field is further increased above that required for producing an electrospinning process, the phenomenon of branching occurs as shown in Figure 5.1. This takes place due to the interaction of electrical and surface tension forces on the surface of the electrospun jet. It has been argued that the energy required for the formation of branches is provided by the radial electric field [116]. The branches were seen on both the straight and bending sections of the electrospun jet. It was observed that the calculated Ohnesorge number was higher than the imposed limit ($Oh \gg 1$**),** which implies that the branching phenomenon requires higher viscous stresses than usually employed for typical

electrospinning. Nevertheless, the wavelength of the resultant branches depends on the competition between the destabilizing electrostatic forces and stabilizing surface tension forces [117]. During the experiment, branching was observed for a certain range of electric field strengths beyond which a further increase in field strength resulted in a predominantly unstable phenomenon.

5.3 Previous works related to surface instability in the presence of electric field

Instability analysis of a charged jet has been studied since the end of the 18th century. In 1894, Bassett [118] obtained the growth rate of both varicose and lateral perturbations in a charged jet. In 1917, Zeleny [75] reported non-axial instabilities in electrified jets. Later, in 1969, Taylor [15] improved Bassett's theoretical results with the help of detailed experiments on jet instability. Since then, theoretical as well as experimental studies have been performed to study surface instability of Newtonian/viscoelastic fluid modeled as either a leaky-dielectric or a perfect conductor. The growth rate of instabilities is usually measured against material parameters such as interfacial surface tension, conductivity, and viscoelasticity of the solution.

In this section, we will study the effect of viscoelasticity of the polymer jet and applied electric field on the jet's instability. The behavior of viscoelastic liquid jet in the absence/presence of electric field has been well documented. Middleman [119] observed the destabilizing effect of viscoelasticity on a jet. Brenn et al. [120] and Liu et al. [121] performed linear axisymmetric and non-axisymmetric stability analysis, respectively for a non-Newtonian liquid jet. They concluded that viscoelasticity destabilizes the jet against both axisymmetric and non-axisymmetric perturbations. Li et al. [122] performed an axisymmetric and non-axisymmetric linear stability analysis of a charged viscoelastic liquid

jet. The viscoelasticity was modeled by the Oldroyd-B constitutive equation, and the fluid was considered a leaky dielectric in nature. They observed that the normal electric field destabilizes both the axisymmetric and non-axisymmetric modes. Furthermore, as electric field increases, the non-axisymmetric modes become unstable and dominate over the axisymmetric modes.

Nevertheless, Wu et al. [123] performed a linear stability analysis of a leaky-dielectric viscoelastic fluid whose constitutive behavior was described using the Jeffreys model assuming the creeping-flow approximation for the entire range of Deborah numbers *De*. They showed that the wavelength corresponding to the maximum growth rate remains unchanged with *De*. In the present analysis, linear stability analysis of a viscoelastic liquid jet confined in a concentric electric field is performed. The analysis helped to analyze the evolution of branches on an electrospun jet. Later, the linear stability analysis was employed to determine the inter-undulation distance. Subsequently, these inter-undulation distances are analyzed and compared with the experimental results.

5.4 Experimental details pertaining to branching of electrospun jet

The polymer employed in the spinning was 6 wt% Poly (ethylene oxide) (M_w = 400,000) dissolved in varying ratios of water and ethanol (99% purity) mixture as solvent. Electrospinning setup shown in Figure 2.1(a) was employed for the analysis. The outer diameter of the glass pipette used for the production of electrospun jet ranged between 50 to 200 μm. The glass pipette was connected to a syringe pump (model SP200IZ, World Precision Instruments, U.S.A.) which was used for controlling the volumetric flow rate of the polymer solution. The volumetric flow rate for the experiments was varied from 1 to

20 µl/hr. The distance between the glass pipette and the collector was about 80 mm. The operating parameters for the analysis can be seen in Table 5.1. The images were obtained with a high-speed camera (model: Photron FASTCAM-Ultima APX-RS, Motion Engineering Company, Indianapolis, U.S.A.**)** connected to a long distance microscopic lens. The images obtained were inverted in nature due to the microscopic lens. The frame rates used for the analysis varied from 5000 to 50,000 fps.

Table 5.1 Table representing the experimental parameters obtained during the analysis.

6 wt% PEO (M_w = 400,000) dissolved in given % v/v ethanol/water mixture	40/60	55/45	70/30
Applied electric field strength for spinning (kV/m)	51.85	51.88	46.91
Applied electric field strength range for branching (kV/m)	74.07-163.17	61.72-128.13	56.79 - 118.53
Volumetric flow rate (µl/hr)	5	5	5

For a particular applied electric field strength, the process was continued for several seconds to ensure a steady-state condition. A continuous branching process was observed for an extended period of time corresponding to a particular applied electric field, keeping all other parameters constant. The phenomenon terminated only when the glass pipette blocked, which was a common occurrence due to the small diameter of the glass pipette used in the analysis. The resultant error for the distance between the branches was found to be less than 10% in all the experimental results repeated over an extended period of time.

The branches presented in Yarin et al. [81] represented a repeated pattern, where the volumetric flow rate was varied cyclically, thus resulting in the appearance and disappearance of branches in a recurring fashion. On the other hand, in our analysis, we gradually varied the applied electric field keeping all other process and material parameters constant. At first, the proper electrospun jet appeared and as the voltage was further increased, branches started forming on the electrospun jet as shown in Figure 5.1. Application of an electric field higher than that required for the production of spinning is necessary but not the sole requirement for the production of branching. It turned out that glass pipette diameter was one of the most important parameter, as it had been noticed that the branching phenomenon was only possible when micro-sized glass pipettes were employed. It was observed experimentally that for a given set of operating conditions, the phenomenon of branching does not occur when the nozzle diameter was on the order of 1 mm.

5.5 Theoretical model pertaining to branching of electrospun jet

In the past decade, a number of mathematical models pertaining to electrospinning have been documented. These mathematical models focused mainly on the straight section [28, 29] and the bending instability [24, 27] of the electrospun jet. To the best of our knowledge, the only work that documented and modeled the phenomenon of branching of electrospun jet was that of Yarin et al. [81]. Yarin et al. [81] performed a static analysis to obtain the possible azimuthal modes on the jet surface. Subsequently, they employed a linear stability analysis to deduce the most unstable azimuthal mode. The axial wavelength corresponding to the most unstable azimuthal mode was then compared to the distance between the branches. Yarin et al. [81] reported that there was fair agreement between the theoretical and

experimental values, and the discrepancies were attributed to low image resolution, which resulted in uncertainties in precisely determining the distance between the branches.

In the present model, a linear stability analysis of the process has been performed to obtain a better understanding of the underlying phenomenon. The analysis follows the work of Yarin et al. [81] with the incorporation of the Maxwell viscoelastic model, thus accounting for the non-Newtonian physical properties of polymer solution. The electrospun jet is modeled as an infinitely long jet of incompressible fluid having perfect conductivity with an unperturbed radius r, enclosed within a virtual cylinder of radius A where $A \gg r$, which acts as a counter electrode, as depicted in Figure 5.2.

The assumption of perfect conductivity was justified by invoking timescale arguments pertinent to this phenomenon. The timescales for the charge relaxation, surface tension (capillary effects) and relaxation time of the polymer was given by $\tau_e = \varepsilon/K$, $\tau_\gamma = \sqrt{\rho r^3/\gamma}$ and $\tau_p = \eta/G$, respectively. The fourth time scale used in the analysis is represented by the ratio of viscous and surface tension forces, which was given by $\tau_a = \eta r/\gamma$. The values of ε and K were interpolated from the data given in Table 1 of Theron et al. [31, 124], whereas the values of ρ and η were obtained from Yarin et al. [24, 125]. It was noted that minor changes occur in the values of $\rho = 10^3$ kg/m^3 and $\eta = 10^2$ Pa. s corresponding to the variations in ethanol content in the ethanol/water solvent mixture. The surface tension of the ethanol/water mixture was calculated using the relation for the surface tension of water/organic material mixtures on Page 421 of Perry et al. [126].

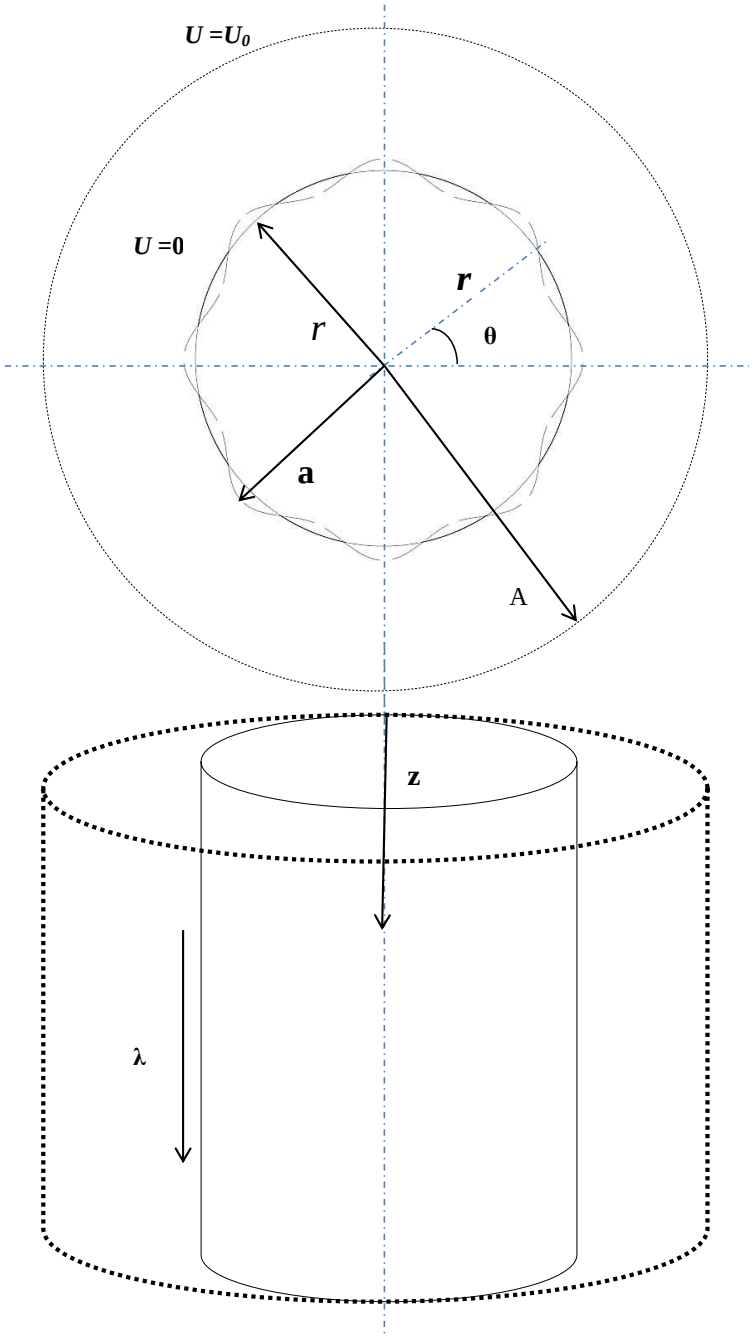

Figure 5.2 Sketch of cross-section of the jet modeled for the mathematical analysis. An infinitely long jet having an unperturbed cross-section radius = *r*, shown by firm line and perturbed cross-section radius = *a*, shown by wavy dashed line is enclosed within a virtual cylindrical of radius *A* where *A*>>*r*. The sketch was not drawn to scale.

The respective time scales are given by $\tau_e = 0.66$ µs, $\tau_\gamma = 42.34$ µs, $\tau_p = 10$ ms and $\tau_a = 0.88$ s. This shows that the charge relaxation time was small in comparison to the

other three characteristic timescales, thus validating our assumption of a perfect conductor for the polymer solution under consideration.

In order for the linear stability analysis to be valid, it is assumed that $\zeta << r$, where ζ is the radial perturbation applied to the unperturbed cylindrical jet and *r* is the initial radius of the jet. The wavelength of the measured inter-branch distance is on the order of $\lambda \approx 10^{-2}$ cm (to be discussed later). *A* is on the order of the tapering length and bending radius of the electrospun jet. This yields $\lambda/A \approx 10^{-2}$, which is sufficiently small to allow for a local analysis of the electrical and hydrodynamic fields. In the local analysis employed, the Laplace's equation for the electric potential was used to obtain the normal Maxwell stress associated with the electric field on the jet surface. In the static analysis performed by Yarin et al. [81], the jet was perturbed by a steady radial undulation given by $\zeta = \zeta_n e^{i[n\theta + k_n z]}$, where ζ_n and k_n were the amplitude of the perturbation and axial wave number corresponding to an azimuthal mode *n*, respectively. The equilibrium state solution was obtained by the balance of surface tension, pressure, and normal component of electrical forces on the surface of jet given by Equation (5.1). For simplicity, the subscript *n* was omitted from the symbols corresponding to the axial wave number and perturbation amplitude in the subsequent equations.

$$\sigma_{\perp\perp}^{inside} = \sigma_{\perp\perp}^{outside} - p_{\gamma} \tag{5.1}$$

$$\sigma_{\perp\perp}^{outside} = \frac{U_0^{\,2}}{8\pi}\left[\frac{1}{r^2 \ln^2(A/a)} - \frac{2\zeta}{r^3 \ln^2(A/a)} + \frac{2\left(dF/dr\right)\big|_{a=r}\zeta}{r\ln(A/a)}\right], \tag{5.2}$$

$$F(a) = \frac{K_n(kA)I_n(ka) - I_n(kA)K_n(ka)}{r\ln(A/r)[I_n(kA)K_n(kr) - I_n(kr)K_n(kA)]}, \tag{5.3}$$

$$\sigma_{\perp\perp}^{inside} = -C, \tag{5.4}$$

$$p_\gamma = \gamma\left[\frac{1}{r} - \frac{1}{r^2}\left(\zeta + \frac{\partial^2\zeta}{\partial\theta^2}\right) - \frac{\partial^2\zeta}{\partial z^2}\right], \tag{5.5}$$

where U_o is the applied electric voltage, C is a constant, I_n and K_n are the modified Bessel function of the first and second kind, respectively, and their subscript *n* denotes the azimuthal mode, with other symbols having their usual meanings. The linearized normal stress outside the liquid jet and the capillary pressure are given by Equation (5.2) and (5.5), respectively. The equilibrium condition resulted in a constant normal stress inside the liquid jet given by Equation (5.4). As the equilibrium analysis was static in nature, it resulted in zero velocities and thus zero viscous stresses on the jet surface. The equilibrium analysis allows possible azimuthal modes on the jet surface to be obtained. In other words, the equilibrium solution yields the possible static cross-sectional shape of the polymer jet.

Subsequently, linear stability analysis was performed to identify the most unstable azimuthal mode. The mode, which developed the highest perturbation amplitude at the earliest time, will arguably result in the formation of undulations on the jet surface, i.e. it gives rise to branches on the jet surface. For the linear stability analysis of the jet, the equilibrium solution was perturbed using the unsteady perturbation function $\zeta = \zeta_n e^{i[n\theta + k_n z] + \delta t}$, where δ is the temporal growth rate of the perturbations and $k = 2\pi/\lambda$ is the axial wave number, with λ representing the axial wavelength corresponding to the azimuthal mode *n*.

The initial evolution of small undulations on the jet surface is governed by the linearized Navier-Stokes equations in cylindrical coordinates. The solution of the linearized Navier-Stokes equation was obtained following the analysis performed in Yarin et al. [127]. The perturbed quantities, such as the perturbation pressure and the perturbation velocity components on the jet surface, are given as follows, where the constitutive properties of a viscoelastic Maxwellian liquid have been incorporated.

$$p' = DI_n(ka)e^{(\delta t+i(n\theta+k_n z))}, \tag{5.6}$$

$$v_r' = \frac{1}{2}\left\{B_1 I_{n+1}(la) + B_2 I_{n-1}(la) + C\left[l_{n+1}(ka) + l_{n-1}(ka)\right]\right\}e^{(\delta t+i(n\theta+k_n z))}, \tag{5.7}$$

$$v_\theta' = \frac{1}{2i}\left\{B_1 I_{n+1}(la) - B_2 I_{n-1}(la) + C\left[l_{n+1}(ka) - l_{n-1}(ka)\right]\right\}e^{(\delta t+i(n\theta+k_n z))}, \tag{5.8}$$

$$v_z' = \begin{bmatrix} \frac{i}{2k}\left\{B_1 lI^1{}_{n+1}(la) + B_2 lI^1_{n-1}(la) + Ck\left[I^1{}_{n+1}(ka) + I^1{}_{n-1}(ka)\right]\right.. \\ \left. + \frac{\left\{B_1 I_{n+1}(la) + B_2 I_{n-1}(la) + C\left[l_{n+1}(ka) + l_{n-1}(ka)\right]\right\}}{r}\right\}... \\ + \frac{ni}{2kr}\left\{B_1 I_{n+1}(la) - B_2 l_{n-1}(la) + C\left[l_{n+1}(ka) - l_{n-1}(ka)\right]\right\} \end{bmatrix} e^{(\delta t+i(n\theta+k_n z))}, \tag{5.9}$$

$$where, l^2 = k^2 + \rho\gamma\left(\frac{1}{\eta} + \frac{\delta}{G}\right), C = \frac{Dk}{\rho\gamma} \tag{5.10}$$

Each prime on the Bessel function represents differentiation with respect to the respective argument. B_1, B_2, C and D are constants, G is the shear modulus, a is the perturbed radius of the jet and the other symbols have their usual meanings. The linearized form of the boundary conditions imposed on the unperturbed jet surface ($a = r$) are given by

$$v_r' = \frac{\partial \zeta}{\partial t}, \tag{5.11}$$

$$\sigma'_{r\theta} = 0, \tag{5.12}$$

$$\sigma'_{rz} = 0, \tag{5.13}$$

$$-\sigma'_{rr} = -\frac{\gamma}{r^2}\left(\zeta + \frac{\partial^2 \zeta}{\partial \theta^2}\right) - \gamma \frac{\partial^2 \zeta}{\partial z^2} - \frac{U_0^2}{8\pi}\left[-\frac{2\zeta}{r^3 \ln^2 \bar{A}} + \frac{2(dF/dr)\big|a = r\zeta}{r \ln \bar{A}}\right], \tag{5.14}$$

where $\bar{A} = A/r$. Equation (5.11) corresponds to the kinematic boundary condition relating the perturbed radial component of the velocity to the imposed undulation ζ on the jet surface. Equations (5.12) and (5.13) signify zero viscous shear stresses on the jet surface. Equation (5.14) balances all the perturbed normal stresses acting on the jet surface. Substituting the perturbed quantities (Equation (5.6)-(5.9)) into the boundary conditions (Equation (5.11)-(5.14)), we obtain a dimensionless characteristic equation for the underlying phenomenon:

$$\begin{aligned}&\left(\tilde{\delta}\right)^2(1+De) + \bar{\delta}Oh^2 \frac{\chi}{I_n(\chi)}\left(\xi Q(\chi,\xi) I^1_{n+1}(\xi) + \xi P(\chi,\xi) I^1_{n-1}(\xi) + \chi\left(I^1_{n+1}(\chi) + I^1_{n-1}(\chi)\right)\right)... \\ &= Oh^2 \frac{\chi}{I_n(\chi)}(1+De) R(\chi,\xi)\left[1 - n^2 - \chi^2 + \frac{U_0{}^2}{4\pi\gamma r\left(\ln^2 \bar{A}\right)}(\chi T - 1)\right],\end{aligned} \tag{5.15}$$

where,

$$\tilde{\delta} = \frac{\delta \eta r}{\gamma}, \tag{5.16}$$

$$Oh = \frac{\eta}{(\rho \gamma r)^{1/2}}, \tag{5.17}$$

$$De = \delta \tau_p, \text{where} \tau_p = \frac{\eta}{G}, \tag{5.18}$$

$$\chi = kr, \tag{5.19}$$

$$\xi = lr = \sqrt{(\chi)^2 + \frac{\tilde{\delta}}{Oh}(1+De)}. \tag{5.20}$$

$\tilde{\delta}$ is the dimensionless growth rate, Oh is the Ohnesorge number representing the ratio of viscous to inertial and surface tension forces, De is the Deborah number representing the ratio of the polymer relaxation time and characteristic flow time. χ and ξ are dimensionless parameters forming the arguments of the Bessel functions. Functions such as $P(\chi,\xi)$, $Q(\chi,\xi)$ and $R(\chi,\xi)$ can be found in the Appendix. The expression *T* in Equation (5.15) is given as

$$T = \frac{K_n(k\bar{A})\left(dI_n(\chi)/d\chi\right) - I_n(k\bar{A})\left(dK_n(\chi)/d\chi\right)}{\left[I_n(k\bar{A})K_n(\chi) - I_n(\chi)K_n(k\bar{A})\right]}. \tag{5.21}$$

5.6 Analysis and comparison of theoretical with experimental results

5.6.1 Results pertaining to the theoretical model

The aim of the theoretical model was to obtain the distance between nascent undulations (λ). Later, this inter-undulation distance was compared with inter-undulation distance (λ_e) obtained experimentally. Theoretical modeling was performed to obtain all possible unstable azimuthal modes (n). Subsequently, Equation (5.15) was solved numerically to obtain dimensionless growth rates $(\tilde{\delta})$ against dimensionless parameter (χ) for all possible azimuthal modes depicted in Figure 5.3. In Figure 5.3, $\tilde{\delta} = 0$ represents the transition from stable to unstable region. Later, dimensionless parameter (χ) for $\tilde{\delta} = 0$ corresponding to the unstable azimuthal mode was obtained. Consequently, dimensionless parameter (χ) was employed to calculate the inter-undulation distance $\lambda = (2\pi r/\chi)$.

The parameters used in Equation (5.15) corresponding to the sample case in Figure 5.3 were: U_0 = 4.6 kV and $\bar{A}$ = 50. The material properties corresponding to 6 wt% PEO (M_w = 400,000) dissolved in 70/30 % v/v ethanol/water mixture were $\rho = 10^3\ \mathrm{kg/m^3}$, $\eta = 10^2$ Pa. s and $\gamma = 30\ \mathrm{mN/m}$. Only solutions for azimuthal modes $2 \leq n \leq N$ were considered, where N is the highest possible unstable azimuthal mode. Here, $n = 0$ corresponds to a circular cylinder, whereas $n = 1$ corresponds to the bending instability of the electrospun jet [81]. It can be seen for the sample case in Figure 5.3 that azimuthal modes $n \leq 14$ are unstable, whereas all higher order modes ($n \geq 15$) are stable for this particular example case.

The next step was to obtain the dominant azimuthal mode. Yarin et al. [81] noted that the condition for highest curvature is likely to be satisfied almost everywhere by the presence of shorter wavelength with small amplitudes. Therefore, it was argued that the amplitude of the static mode that has the longest wavelength would be the dominant mode and if the curvature near the highest peaks is high, it is likely that an undulation will develop near each of the peaks of the longest wavelength mode. It was thereby argued that the highest static curvature occurs at the peaks of the mode with $n = N$, i.e., n =14 (highest order mode).This implies that the undulations close to the n=14, will develop the highest perturbation amplitude at the earliest time, will grow more rapidly, and will result in the formation of branches. Subsequently, dimensionless parameter (χ_N) for $\tilde{\delta} = 0$ corresponding to n=14 was obtained. Consequently, dimensionless parameter (χ_N) was employed to calculate the inter-undulation distance $\lambda = (2\pi r/\chi_N)$.

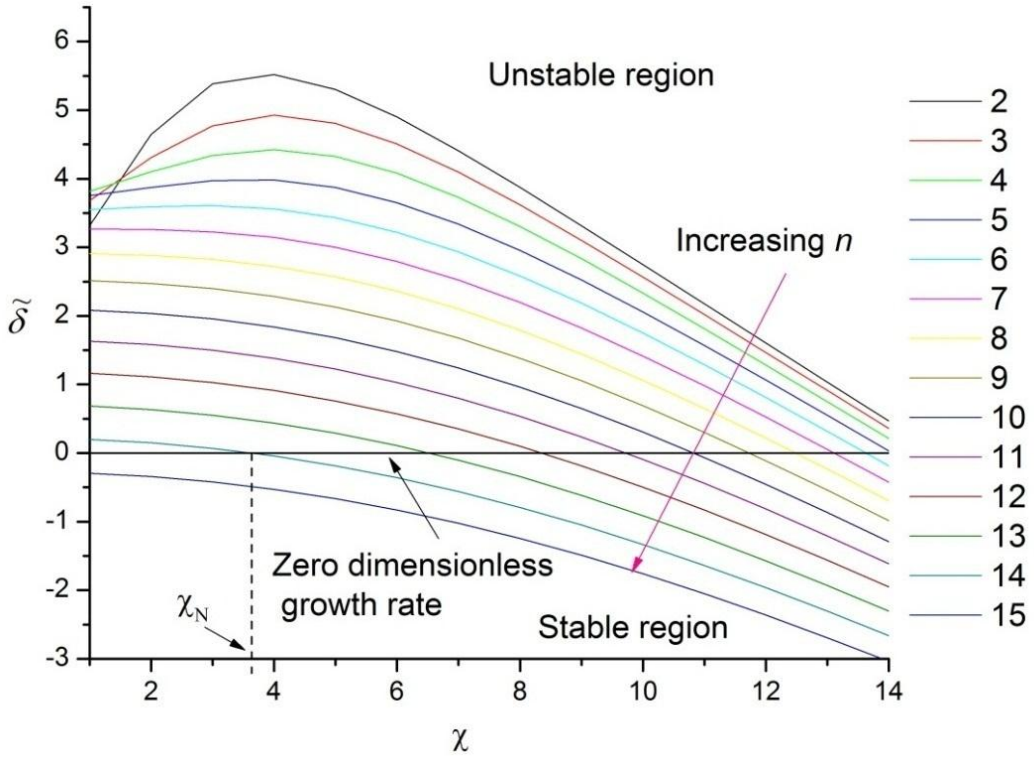

Figure 5.3 The dimensionless growth rate against the dimensionless parameter (χ) for different azimuthal mode (n). Polymer employed for the analysis was 6 wt% PEO (M_w = 400,000) dissolved in 70/30 % v/v ethanol/water mixture, and the applied voltage is 4.6 kV. The distance between the glass pipette and metal collector is 81 mm. The highest order azimuthal mode was found to be N = 14.

These inter-undulation distances were obtained against different operating parameters. Subsequently, a comparison was made between the inter-undulation distances obtained experimentally with the theoretical model. The experimental studies of the inter-undulation distance are presented in the following section. Subsequently, the experimental and theoretical results are compiled in Table 5.2.

5.6.2 Analysis of experimental results

Experiments were performed to yield the distance between the nascent undulations (λ_e) as described in section 5.4. The data collected on inter-undulation distance was averaged over

an extended period of several seconds. The data corresponding to cases where nascent undulations appeared in the given bandwidth were selected. The bandwidth was taken to be within 0.265 mm from the jet initiation. This was done to capture minimum possible inter-undulation distance for a given operating parameter as (λ_e) will increase along the jet's trajectory. The inter-undulation distance (λ_e) within the given bandwidth against different operating parameters is depicted in Table 5.2. During the experimental analysis, the concentration of polymer solution was kept constant at 6% PEO (M_w = 400,000), whereas the percentage of ethanol in the ethanol/water solvent mixture was varied. The reduction in the percentage of ethanol in the solvent mixture resulted in an increase in the surface tension of the solvent mixture. During the experimental analysis, three different solvent mixtures for the given concentration were studied against process parameters. In Table 5.2, experimental cases (1-4), (5-8), and (9-12) depict data pertaining to (70/30), (55/45), and (40/60) ethanol/water solvent mixture for the given polymer concentration, respectively. For a given applied electric field strength (U_0 = 5 kV), it was noted from Table 5.2 that the increase in surface tension for the experimental cases (2 and 5) resulted in an increase in the inter-undulation distance. A similar result was obtained against (U_0 = 5.6 kV) for the experimental cases (3 and 6). This is because surface tension acts as stabilizing force against an externally applied electric field. Li et al. [128] analyzed the non-axisymmetric modes of a charged coaxial jet. They noted that higher non-axisymmetric modes ($n > 1$) were stabilized by the interfacial tension. Therefore, the stabilizing effect of surface tension hinders the growth of undulations resulting in an increase in the inter-undulation distance with an increase in the surface tension of the polymer solution.

For a given polymer solution (for instance, experimental cases (1-4)), an increase in the applied electric field strength was found to decrease the inter-undulation distance. This is because an increase in the applied electric field will surpass the stabilizing surface tension force, thus aggravating non-axisymmetric instability and resulting in reduced inter-undulation distance. The inter-undulation distance showed similar trends with the applied electric field for all three solvent mixtures employed in the analysis.

5.6.3 Comparison between theoretical and experimental results

It became apparent from Table 5.2 that the theoretical results were not in agreement with the experimental data. Through experiments, it was observed that the inter-undulation distance (λ_e) decreases with an increase in the applied electric field strength. This observed effect of applied electric field on inter-undulation distance is visible in experimental cases (1-4), (5-8), and (9-12), for (70/30), (55/45), and (40/60) ethanol/water solvent mixture, respectively. However, no such trend was observed in the inter-undulation distance (λ) obtained theoretically.

It was also noted through experimental analysis that for a given applied electric field strength, an increase in surface tension resulted in an increase in the distance between nascent undulations. Experimental cases (2 and 5) for applied field strength (U_0 = 5 kV) and experimental cases (3 and 6) for (U_0 = 5.6 kV) are two such examples. Theoretically calculated values showed no such trend of surface tension on inter-undulation distance. The apparent differences between the theoretical and experimental values require additional analysis of the theoretical model.

Table 5.2 Comparisons of inter-branch distance for experimental and theoretical analysis, polymer employed for the analysis was 6 w% PEO (M_w = 400,000) dissolved in varying ethanol/water mixture as solvent.

Serial number	Ethanol/water solvent mixture % v/v	Jet Diameter $(2r\ \mu m)$	Applied Electric field (U_0) (KV/m)	Surface tension of polymer solution (γ) (mN/m)	$\bar{A}$	Ohnesorge Number (Oh)	Azimuthal Mode (N)	Dimensionless parameter $(\chi_N = k_N r)$ Obtained against $(n = N)$	Theoretically obtained inter-undulation distance $(\lambda = (2\pi r/\chi_N))$ μm	Experimentally observed inter-undulation distance $(\lambda_e)\ \mu m$
1	70/30	52.92	4.6	30.24	50	3.54e+004	14	3.62	45.90	74.60
2	70/30	52.92	5.0	30.24	50	3.54e+004	17	2.89	57.49	59.91
3	70/30	47.61	5.6	30.24	50	3.74e+004	24	4.58	32.64	52.78
4	70/30	38.90	6.8	30.24	50	4.13e+004	44	8.90	13.72	41.66
5	55/45	64.51	5.0	37.52	50	2.87e+004	11	1.71	118.45	96.77
6	55/45	59.10	5.6	37.52	50	3.02e+04	14	7.15	25.95	67.43

7	55/45	53.80	6.2	37.52	50	3.14e+004	21	3.99	42.33	49.50
8	55/45	44.54	7.2	37.52	50	3.16e+004	35	5.48	25.53	36.67
9	40/60	31.50	6.0	49.31	50	3.596e+04	25	7.29	13.56	49.45
10	40/60	31.50	6.6	49.31	50	3.59e+04	31	6.59	19.05	43.21
11	40/60	26.88	7.6	49.31	50	3.87e+004	49	8.80	9.59	35.60
12	40/60	22.48	8.8	49.31	50	4.26e+004	57	5.22	13.45	26.54

In order to resolve the discrepancy (between theoretical and experimental results), parameters pertaining to the theoretical model were analyzed to quantify their effect on inter-undulation distance. The four parameters of the analysis are $\bar{A} = A/r$, Ohnesorge number (Oh), Deborah number (*De*), and dominant azimuthal mode. It should be noted that Ohnesorge and Deborah numbers were calculated from the data obtained experimentally. It was noted that viscous stresses (which affects Ohnesorge number) dominate during the branching phenomenon. Ohnesorge number was always found to be much greater than unity in the experiments (Table 5.2). When the Ohnesorge number was kept greater than the imposed limit ($Oh >> 1$), almost no variation in the inter-undulation distance was observed. Deborah number was the second parameter varied during the theoretical analysis to establish its effect on the inter-undulation distance. Deborah number for the analysis was $De = \delta\tau_p$, where τ_p is the polymer relaxation time and δ is the dimensional growth rate. It was noted from Figure 5.4 that the dimensionless growth rate $(\tilde{\delta})$ increases corresponding to an increase in relaxation time. This is possibly because an increase in relaxation time provides ample time for undulations to grow before the polymer molecules start to relax back to its steady state. This demonstrates that an increase in polymer relaxation time will promote the formation of undulations, and therefore branches on the surface of the electrospun jet. However, it was observed from the theoretical model that the axial wavelength corresponding to the fastest growing azimuthal mode remains nearly the same for all conceivable variations of τ_p. This is possible as the equilibrium solution obtained from solving Equation (5.1) is independent of the rheological properties of the polymer solution. This has also been observed by Tomar et al. [117] for the long wavelength instability analysis performed on a viscoelastic fluid in the presence of an electric field.

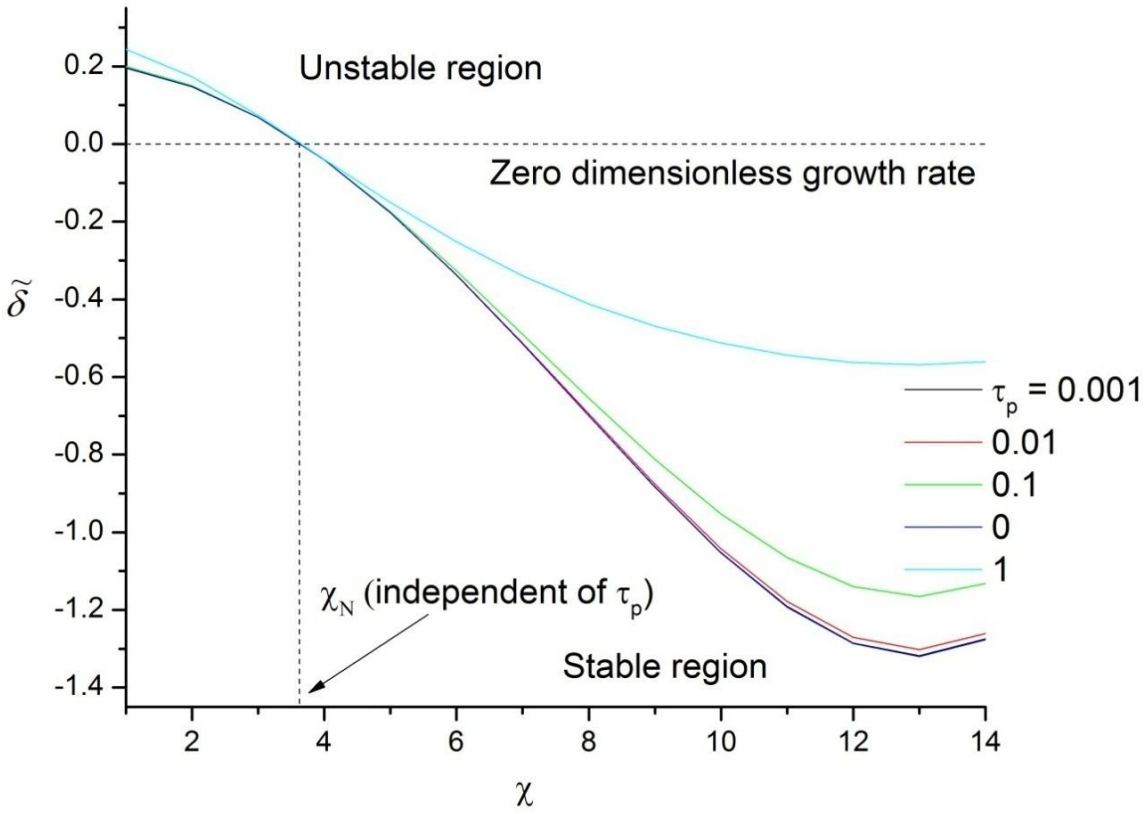

Figure 5.4 The effect of variation of polymer relaxation time (τ_p) on the growth rate of nascent undulations. The parameters used for the analysis corresponds to the sample case in Figure 5.3. The azimuthal mode n was equal to 14, the highest order mode for the sample case.

Therefore, the key parameters affecting the theoretical results are the dominant azimuthal mode and dimensionless parameter $\bar{A} = A/r$. It is visible from Figure 5.3 that the growth rate for *n* =2 will be the highest at any given time for all possible unstable azimuthal modes. This implies that *n* = *N* may not represent the most likely solution for branching of the electrospun jet. It is also known through experimental analysis that the jet flattens before the initiation of undulations, as discussed in detail in the next section. This implies that azimuthal mode $n = 2$ is the dominant mode and responsible for branching of the electrospun jet. Therefore, the theoretical model was reanalyzed against $(n = 2)$ as opposed to $(n = N)$ to calculate the effect of dimensionless parameter $(\bar{A} = A/r)$ on the inter-

undulation distance. The parameter $(\bar{A} = A/r)$ was introduced in the mathematical modeling, which is on the order of the tapering length and bending radius of the electrospun jet.

5.7 Mechanism of the occurrence of branching at azimuthal mode (*n*=2)

n = 0 *n*=1 *n*=2

Figure 5.5 Branching of an electrospun jet can be considered as a complex mixture of azimuthal mode *n*, where *n* is 0, 1 and 2.

It has been documented that a smooth circular cylinder is the only quasi-stable shape of the surface of an *uncharged* fluid jet on time scales shorter than those corresponding to capillary instability [129]. However, as the jet is charged by employing an externally applied electric field, many quasi-stable undulating shapes may occur on the same time scales. An undulation can move an element of area on the surface of the jet in the outward direction, thus carrying the electric charge on that element to a lower potential. By this movement to a lower potential, the undulation acquires enough energy to create the additional surface area required to form the quasi-stable undulation as shown in Figure 5.6. This undulation may recede/vanish if the electric potential is decreased beyond a critical value.

When the applied electric field was increased beyond that required for the production of an electrospinning process, the circular jet emanating from the glass nozzle started to flatten, and undulations started appearing on the edges of those flattened sheets, which subsequently gave rise to branches, as shown in Figure 5.6. This flattening implies that *n* = 2

is the dominant azimuthal mode. Nevertheless, azimuthal mode n = 0, and 1 are also visible during the branching phenomenon. Therefore, the branches on electrospun jet can be considered as a complex mixture of azimuthal modes 0, 1, and 2 depicted in Figure 5.5. These nascent undulations occur in different azimuthal directions to minimize the total potential energy of the system depicted in Figure 5.7.

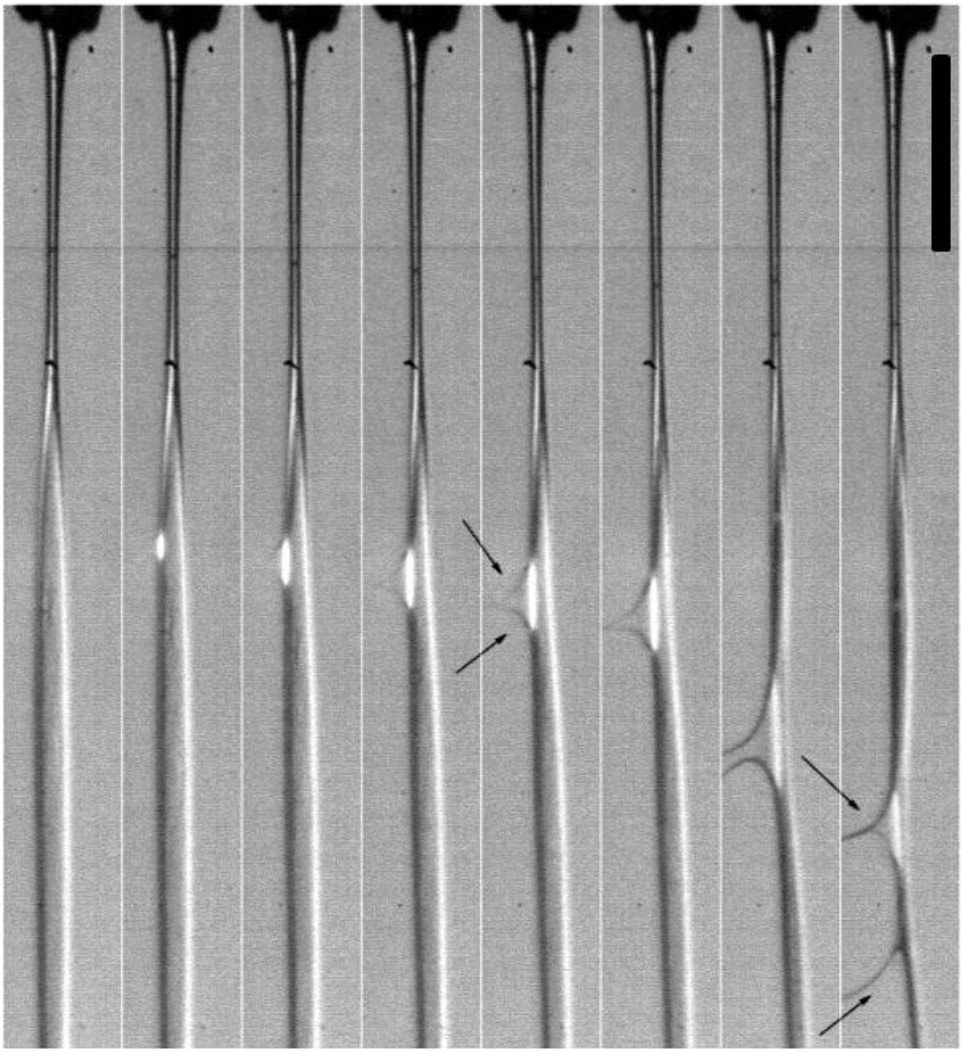

Figure 5.6 Flattening and emergence of undulations on the jet. Polymer employed was 6 w% PEO (M_w = 400,000) dissolved in 70/30 % v/v ethanol/water solution and the applied field strength was 56.79 kV/m. The time difference between the first six frames is 0.4 ms whereas for the last three frames is 2 ms Arrows in the fifth frames depict two growing undulations with time, which later in time result in the formation of two full-grown branches. The scale bar in the image is equal to 0.5 mm.

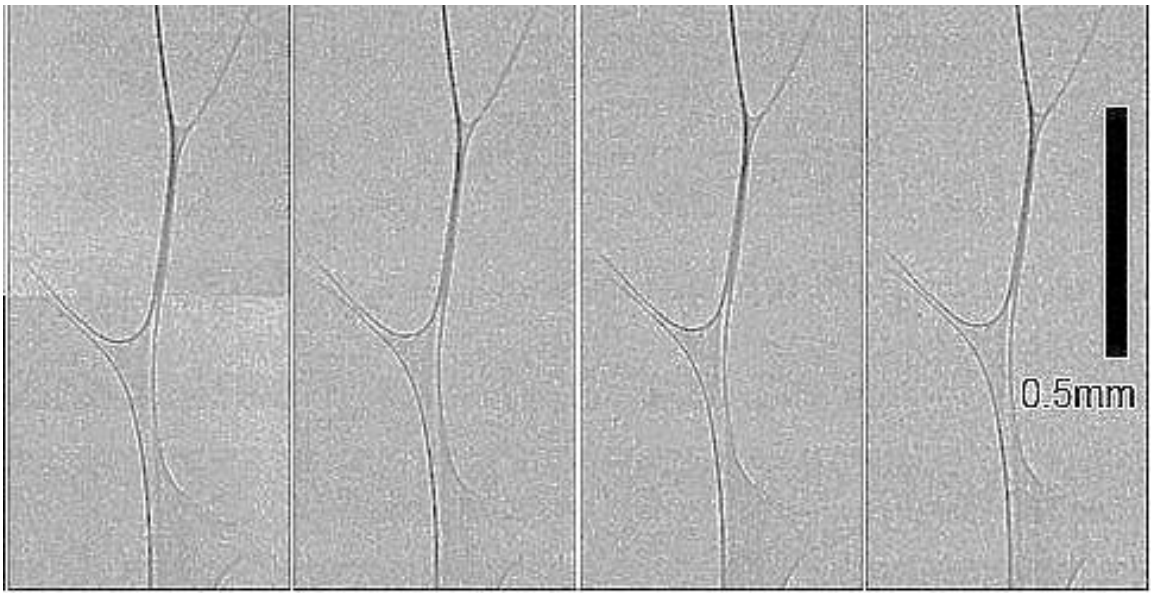

Figure 5.7 Regular pattern of the undulation on the surface of the jet. Polymer employed was 6 w% PEO ($M_w = 400{,}000$) dissolved in 70/30 % v/v ethanol/water solution and the applied field strength was 56.79 kV/m. The time difference between the frames is 10 μs. The image is inverted.

5.8 Effect of dimensionless parameter on theoretical model

It can be seen from Figure 5.3 that the growth rate for n =2 will be the highest at any given time for all possible unstable azimuthal modes. This implies that $n = N$ (highest order mode) may not represent the most likely solution for branching of electrospun jet. Flattening of the electrospun jet before the initiation of undulations also confirms n=2 as the dominant azimuthal mode. Therefore, for n = 2, analysis was performed to check the effect of parameter ($\bar{A} = A/r$) on the results of the theoretical model.

The parameter ($\bar{A} = A/r$) was the one introduced in the mathematical modeling, which was on the order of the tapering length and bending radius of the electrospun jet. Yarin et al. [81] kept $\bar{A}$ equal to 50. They argued that the value of A obtained against $\bar{A} =$

50 was agreeable with those observed experimentally. The same value of $\bar{A} = 50$ was employed in the analysis presented in section 5.6.1.

The effect of $\bar{A}$ on the modeling results was obtained by back processing of the theoretical model. This back processing was achieved with the help of experimental results, which is explained as follows: Equation (5.15) was employed for this analysis. In Equation (5.15), $\tilde{\delta} = 0$, whereas *Oh* and *De* were calculated from the experimental results. Here, *n* was kept equal to 2 and dimensionless parameter $\left(\chi_e = \frac{2\pi}{\lambda_e} r\right)$ was calculated from the average distance between the nascent undulations obtained experimentally. These calculated values of $\bar{A}$ against different operating conditions are presented in Table 5.3.

The results showed that the value of $\bar{A}$ varied with the operating parameters, rather than a constant value assumed by Yarin et al. [81] for all the operating parameters. This discrepancy may be due to the assumption of predominantly radial electric field acting on the electrospun jet in our model, which is based on the work of Yarin et al. [81]. The model assumed that electrified jet was subjected to a radial electric field provided by uniformly distributed charges on its surface. This assumption required the absence of axial electric field and a constant jet radius along the axial direction. These assumptions may not be reasonable as the electrospun jet thins asymptotically along its trajectory, as discussed in section 3.2. Axial electric field, though reducing in value along the jet's trajectory, may not be negligible. This implies that parabolic electric field lines may enclose the jet in case of non-negligible axial electric field strength. Parabolic electric field lines are representative of point-plate experimental setup usually employed in electrospinning.

These parabolic electric field lines imply that $\bar{A}$ will vary along the trajectory of the electrospun jet. The value of $\bar{A}$ will be minimum at the nozzle-tip and will increase gradually towards the collector surface. The variability in the dimensionless parameter $\bar{A}$ was also noted during the back processing. The dimensionless parameter $\bar{A}$ was found to decrease with an increase in the applied electric field. This observed effect of applied electric field on $\bar{A}$ is visible for experimental cases (1-4), (5-8), and (9-12), for (70/30), (55/45), and (40/60) ethanol/water solvent mixture, respectively. This may be because an increase in the applied electric field will accelerate the initiation of the undulations close to the nozzle, thus reducing the value of $\bar{A}$ with the increase in applied electric field strength.

For a given applied electric field strength (U_0 = 5 kV), it was noted from Table 5.3 that the increase in surface tension for the experimental cases (2 and 5) resulted in an increase in the dimensionless parameter ($\bar{A} = A/r$). A similar result was obtained against (U_0 = 5.6 kV) for the experimental cases (3 and 6). This is because the stabilizing effect of surface tension hinders the growth of undulations resulting in an increase in the dimensionless parameter ($\bar{A} = A/r$) (representing the location of occurrence of undulation) with an increase in the surface tension of the polymer solution. The dimensionless parameter ($\bar{A} = A/r$) depicted a reasonable trend with surface tension and applied electric field, making it dependent on operating parameters. Thus, the variation in dimensionless parameter ($\bar{A} = A/r$) can be considered as a possible cause of discrepancy between experimental and theoretical results.

Table 5.3 Calculation of the parameter $\overline{A}$ with the help of experimental data. Polymer employed for the analysis was 6 wt% PEO (M_w = 400,000) dissolved in varying ratios of ethanol/water mixture as solvent.

Serial number	Ethanol/water solvent mixture % v/v	Jet Diameter $(2r\ \mu m)$	Applied Electric field (U_0) (KV/m)	Surface tension of polymer solution γ (mN/m)	$\overline{A}$	Ohnesorge Number (Oh)	Azimuthal Mode (N)	Dimensionless parameter $\left(\chi_e = \frac{2\pi}{\lambda_e} r\right)$ calculated against (λ_e)	Experimentally observed inter-undulation distance (λ_e) (μm)
1	70/30	52.92	4.6	30.24	319	3.54e+004	2	2.22	74.60
2	70/30	52.92	5.0	30.24	256	3.54e+004	2	2.77	59.91
3	70/30	47.61	5.6	30.24	250	3.74e+004	2	2.83	52.78
4	70/30	38.90	6.8	30.24	242	4.13e+004	2	2.93	41.66
5	55/45	64.51	5.0	37.52	339	2.87e+004	2	2.09	96.77
6	55/45	59.10	5.6	37.52	258	3.02e+04	2	2.75	67.43
7	55/45	53.80	6.2	37.52	208	3.14e+004	2	3.41	49.50

8	55/45	44.54	7.2	37.52	186	3.16e+004	2	3.81	36.67
9	40/60	31.50	6.0	49.31	357	3.59e+04	2	1.99	49.45
10	40/60	31.50	6.6	49.31	311	3.59e+04	2	2.28	43.21
11	40/60	26.88	7.6	49.31	299	3.89e+004	2	2.37	35.60
12	40/60	22.48	8.8	49.31	267	4.26e+004	2	2.65	26.54

5.9 Conclusion

In order to characterize higher-order instability, linear stability analyses of the electrified jet including non-Newtonian effects have been performed. The linear stability analysis helped to predict the axial wavelength corresponding to the highest order azimuthal mode. Subsequently, the axial wavelength was compared against the experimentally determined inter-undulation distance. The discrepancy in the inter-undulation and their respective trends for the theoretical and experimental values was attributed to the choice of dominant azimuthal mode. Through experimental analysis, the dominant azimuthal mode was observed to be 2. Later, the theoretical model was reanalyzed against $n = 2$ to calculate the effect of relevant dimensionless parameters on the inter-undulation distance.

The dimensionless parameter ($\bar{A} = A/r$) introduced in the mathematical modeling was found to affect the inter-undulation distance. The effect of $\bar{A}$ on the modeling results was obtained by back processing of the theoretical model. Dimensionless parameter $\bar{A}$ was found to decrease with an increase in the applied electric field strength thus invalidating the assumption of constant $\bar{A}$. The assumption of constant $\bar{A}$ was based on another assumption of a predominantly radial electric field. Therefore, the assumption of a predominantly radial electric field is considered as the possible cause of the discrepancy between experimental and theoretical results.

Chapter 6 Electrospinning as a potential mass production technique

6.1 Introduction

Electrospinning is related to two established manufacturing processes, i.e. conventional mechanical fiber spinning and electrostatic atomization. Nevertheless, electrospinning also has important differences, such as the application of electrostatic forces as the driving force unlike mechanical fiber spinning, and the production of long continuous polymer jet unlike atomization. From the electromechanical point of view, electrospinning is a process of the elongational flow of a charged polymer jet that is stretched by intensive electric forces. An electrospun jet also undergoes instabilities different from those of the atomization process. Nevertheless, these instabilities can be suppressed or eliminated by controlling the operating parameters, thus allowing for the better control of the electrospinning process. Two techniques have been proposed to obtain better control and optimization of electrospinning. They include (a) reduce applied electric field to half the value required for initiating electrospinning, and (b) suppression of bending instability and production of regular sized microfibers. It is argued that these techniques will help in projecting electrospinning as a sustainable manufacturing technique. Finally, results are summarized in section 6.5.

6.2 Overview of the proposed techniques

6.2.1 Laser induced electrospinning

This method uses a pulsed laser, which is focused inside the drop close to the liquid surface. The pulse cavitates the liquid and produces a protrusion from the tip of the drop. The protrusion narrows through drainage and vertical stretching, thus concentrating the electric field and increasing the charge density, until it overcomes the surface tension and produces

the electrified jet. This approach can reduce the value of the applied electric field to half the level required to start conventional electrospinning from a stationary drop.

While gravity plays no role in initiating the jetting in practice, electrospinning is sometimes started by simply turning on the liquid flow into a pendant drop and letting it grow in size until gravity detaches it from the nozzle. The pinch-off leaves a thread that stretches out between the nozzle and the drop, thereby acting as the start of the electrospun jet. As there was no surface tension to overcome in this scenario, the spinning started below the critical voltage. However, this waste liquid and the falling drop interfere with the formation of the nanofibers on the collection surface. Furthermore, a sessile drop sitting on a bottom platform, as in our configuration will not be pinched off by gravity.

Herein the electrospun jet was initiated at relatively lower voltages compared to the conventional process for the same operating parameters. This was achieved through a laser pulse focused just under the free surface of the drop, to form a local protrusion that leads to jetting. A different approach has recently been proposed to reduce the applied voltage in electrospinning. This method was based on striking the drop surface with a tungsten electrode to obtain jetting at relatively low voltages [80]. Here, the wire breaks the surface neutralizing the surface tension, and a thread can be pulled out. However, this process had the limitation of using a tungsten electrode, each time to start jetting, whereas our method is based on a non-contact approach. Furthermore, the presence of the tungsten electrode will interfere with the background electric field.

6.2.2 Production of regular sized microfibers through near-field electrospinning

This technique proposes to produce regular-sized microfibers with the help of near-field electrospinning. For low concentrations of a polymer solution, the fragmentation of a polymer jet has been observed for the relatively high-applied electric field strengths. This phenomenon results in the production of regular-sized fragments of microfibers, in contrast to the long curling and spiraling electrospun jet that is commonly obtained during the conventional electrospinning process. Mass production is rendered feasible using this technology.

For a given polymer-solvent mixture, a minimum viscosity is required for the initiation of electrospinning. Failure to fulfill the requirement may result in fragmented jet, 'beads-on-string' structure or in some cases, electrospraying [130, 131]. The viscosity of the polymer solution can be increased either by increasing the concentration of the polymer solution or the molecular weight of the polymer employed [132-135]. Large molecular weight of the polymer is responsible for the chain entanglement and is mainly accountable for the long fiber formation in electrospinning. The proposed approach is to reduce the resultant chain entanglement and thus provide the electrospun jet the tendency to fragment down into regular fragments under the application of the high electric field.

6.3 Experimental setup

6.3.1 Experimental design and analysis of laser induced electrospinning

The experimental setup consists essentially of a parallel plate system as shown in Figure 6.1. The drop sits in a 1 mm thick metallic collar, which is 6 mm in outer diameter and has a central hole between 2.5 to 4.0 mm in diameter.

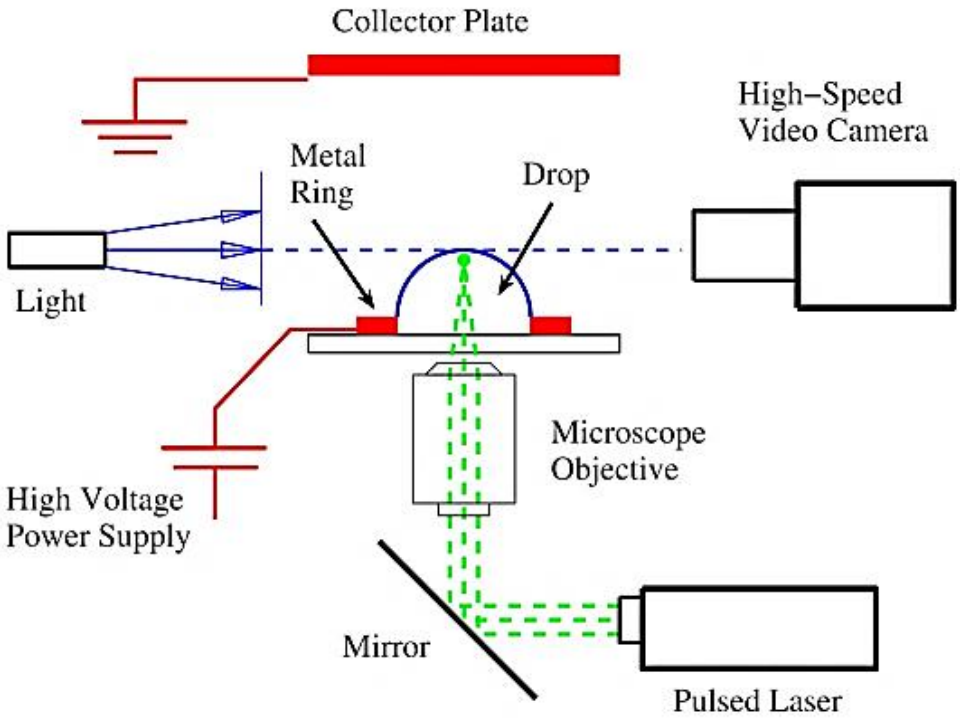

Figure 6.1 Schematic diagram depicting the setup for laser-initiated electrospinning. Not drawn to scale.

This collar is glued to a glass plate, which is about 0.8 mm in thickness. Hydrophobic material was sprayed on the surface of the metallic plate to avoid the spreading of the polymer drop, by pinning the contact line at the inner edge. The metallic collar is connected to a high voltage power supply.

The top circular aluminum plate, of 51 mm in diameter, acts as a grounding surface. The results shown herein all used a 2 wt% PEO (M_w = 400,000) aqueous solution. A pulsed Nd:YAG laser (New Wave Research, model SOLO I15 Hz), with 15 mJ energy per pulse and duration of 5 ns, was employed for the experiments. The laser beam was focused by a 20× microscopic objective directed through the drop with the beam-waist close to the top liquid surface. The location of the laser spot can be adjusted by vertically shifting the objective with a micrometer. Most experiments used a high-speed video camera (Photron

FASTCAM-Ultima APX-RS) at frame-rates up to 30 kfps, with some experiments using a Hitachi-made prototype camera using frame rates up to 100 kfps. Imaging was done with a long-distance microscope (Leica Z-16 APO zoom), or Nikkon 105 mm macro lens, to capture the detailed close-up images of the jetting mechanism.

6.3.2 Experimental design for generating regular-sized fibers

The experimental setup consists of a Point-plate system shown in Figure 2.1 (a). Here, the 'point' is represented by a glass pipette (outer diameter about 5 to 50 µm) connected to High-voltage supply and the dispenser, which controls the volumetric flow rate with the help of backpressure. The 'plate' is an aluminum disc of 50 mm diameter (Thickness = 10 mm), which acts as the collector. The distance between the glass pipette and collector is about 13 mm. The concentration of the polymer solution used for the analysis was kept constant to 0.5 wt% PEO in distilled water, whereas the molecular weight of PEO was varied.

The applied electric field varied from 0.5 to 300 KV/m and the flow rate during the analysis was considered as a dependent variable, i.e. it was varied for a given electric field to generate fragmented polymer fibers. The detailed intricacies of the process are obtained with the help of a High-speed video camera (Model: Photron FASTCAM-Ultima APX-RS) at frame-rates up to 30 kfps, with some experiments using a Hitachi-made prototype camera using frame rates up to 540 kfps connected to a long-distance microscopic Lens (Model: Leica Z16 APO zoom).

6.4 Results and discussion

6.4.1 Analysis of the laser induced electrospinning

Figure 6.2 shows the laser-induced onset of the electrospinning. Here the drop was in a fixed electric field when a laser pulse was applied, at ~200 μm below the surface. The strength of the electric field was 300 kV/m, which was less than half of the critical value, $E \simeq 690$ kV/m needed to produce a singular Taylor cone in our configuration. This critical value was determined by slowly increasing the voltage, in the experiments without the laser pulse. The laser cavitates the liquid, forming expanding plasma under the surface, which forces out a protrusion from the top of the drop. The width of this protrusion is initially about 350 μm (third frame) and it emerges at 1 m/s. The top of the protrusion decelerates to 0.2 m/s in the second row of Figure 6.2 where the overall electric field is pulling it up and the capillary force pulling the top down, are approaching a balance. At the same time, the liquid is being drained back into the drop by the excess capillary pressure $\sigma_\gamma \simeq \gamma/R_p$, where R_p represents the azimuthal radius of the protrusion. Therefore, the protrusion becomes thinner by both drainage and stretching.

The presence of this protrusion greatly concentrates the electric field. Furthermore, the reduction in surface area concentrates the electric charge, and the surface curvature at the tip increases until it becomes unstable, sending out the microjet 4.5 ms after the laser pulse. Figure 6.3(a) shows close-up images of the tip of the protrusion when the electrified fine jet emerges at much higher velocity ($\simeq$ 11 m/s). In Figure 6.3 (b), we estimate the surface curvature at the top of the protrusion, leading up to the ejection time.

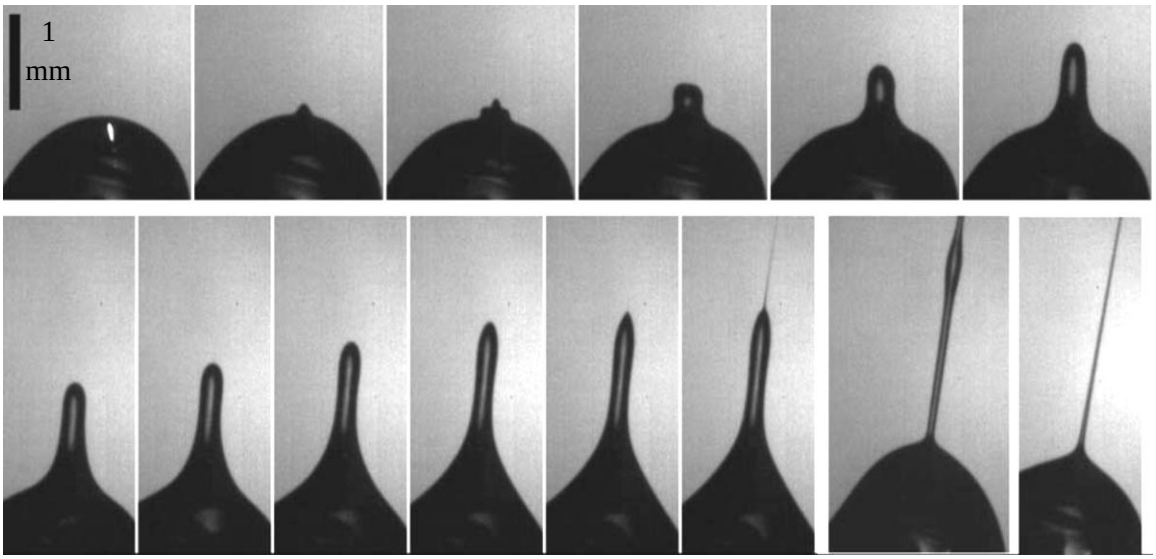

Figure 6.2 The sequence of frames depicts the laser-initiation of the electrified jet, from a drop of 2 wt% PEO (M_w = 400,000) solution. Frames are shown at t = 0.089, 0.178, 0.444, 0.711, 1.11, 1.69, 2.36, 3.33, 4.22, 4.53, 4.78, 10.5 and 40 ms after the laser pulse visible in the first frame. The last frame shows the jet shape much later, at 0.4s after the laser pulse. The applied electric field was 300 kV/m.

When the jet emerges, the tip curvature is ~ 60 times higher than the drop curvature. The half-cone angle appears close to the critical angle observed in the literature, i.e. around 49^{o} [25]. The most important control parameter in this particular mechanism was the depth of the point-of-focus of the laser pulse, below the drop surface. If the laser is focused too close, an ejecta crown emerges out of the surface, producing irregular splashing. Figure 6.4 (a) shows a laser close to the free surface, which opens a crown resulting in irregular side-jets alongside the main vertical jet. Regular concentrated protrusions are generated when the laser depth is between ~150-500 µm, for the 15-mJ pulse energy. Higher pulse-energy will change this range. Figure 6.4 (b) shows regular jetting for a weaker 10 mJ pulse. Here the protrusion is pointier and is missing the thicker bead prominent in Figure 6.2. The microjet emerges after 140 µs.

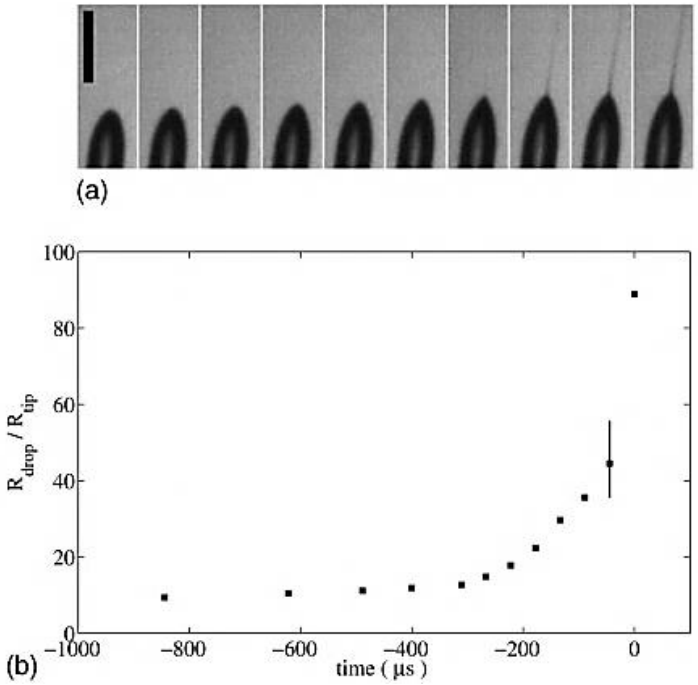

Figure 6.3 (a) Close-up images of the onset of the microjet, from the same sequence as in Figure 6.2. The frames are 44.4 μs apart. The scale bar is 0.5 mm, and (b) the increase in tip curvature vs. time approaching the micro jetting. The tip-curvature is normalized by the undisturbed drop curvature.

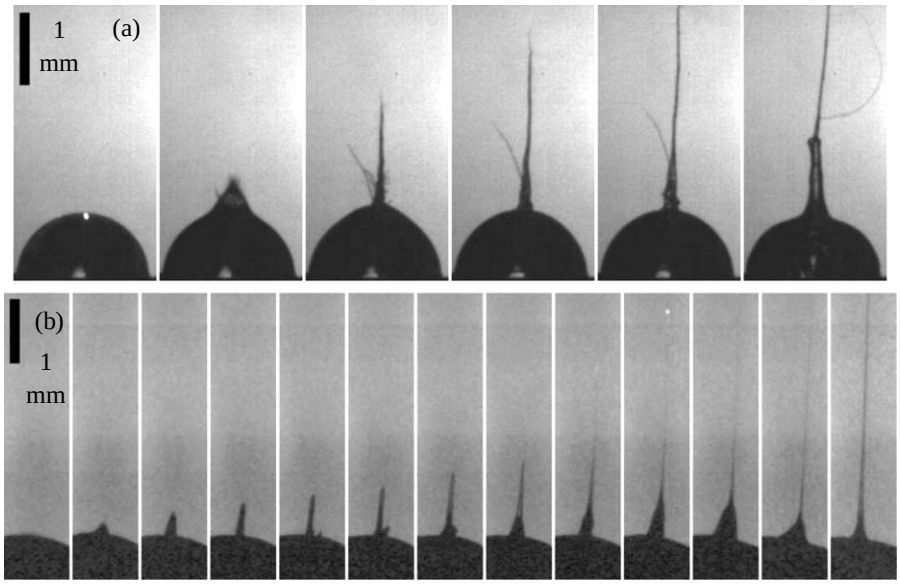

Figure 6.4 (a) Jetting for a laser spot very close to the surface of the drop (< 100 μm). The first 5 frames are spaced by 44.4 μs with the last frame 667 μs after the laser pulse. The applied electric field was 300 kV/m. (b) Jetting from a 10 mJ laser pulse. First, 12 frames are spaced by *dt* = 20 μs, with the last one 2.4 ms later.

6.4.2 Analysis of the production of regular-sized microfibers

Before analyzing near-field electrospinning, we will give a brief overview of electrospraying/atomization to better understand the underlying phenomenon. Electrospraying is one of the most versatile techniques for the mass production of droplets from Newtonian fluids and is being employed in a variety of applications ranging from the ink-jet printer to drug delivery [136-140]. The applied electric field for electrospraying can be as low as 200 kV/m to as high as 10,000 kV/m for electro-flow focusing configuration [141]. Electrospinning uses the same principle of applying a high electric field to a fluid drop, with the difference that the fluid molecule has a chain-like structure, and their entanglement prevents them from breaking down into droplets [142]. Conventionally, electric field on the order of 100 kV/m is ample enough for the production of the electrospinning process, which is relatively smaller than applied for electrospraying [24, 26].

The aim was the production of regular-sized microfibers and therefore, projecting electrospinning as a viable mass production technique. Large molecular weight of the polymer is responsible for the polymer chain entanglement and fiber production. The approach is to use a low concentration of the polymer solution to reduce the resultant chain entanglement and thus provide the electrospun jet the tendency to fragment down into regular sized fragments. For the analysis, the concentration of the polymer solution was kept constant to a 0.5 wt%, whereas the molecular weight of the polymer varied from 600,000 to 2,000,000 to measure their effect on the fragment formation. Surface tension-driven break-up of cylindrical fluid elements into droplets becomes relevant in electrospinning under very low solution concentration (or viscosity), resulting in beaded texture or cups [143, 144].

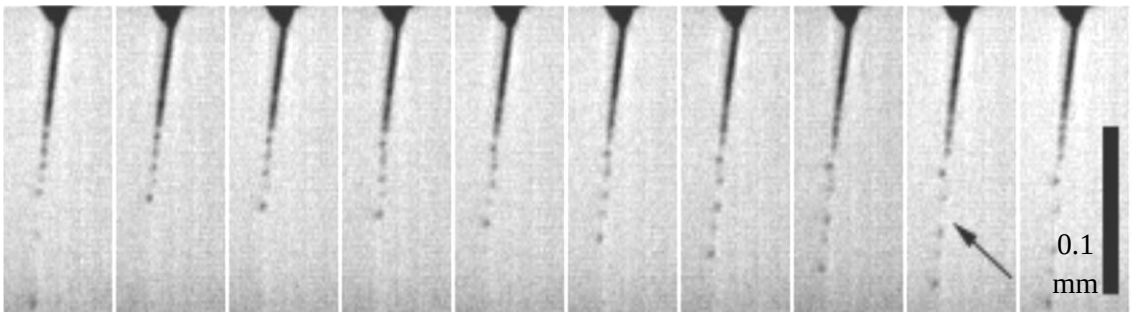

Figure 6.5 The figure depicts 'beads-on-string' structure of 0.5 wt% PEO (M_w = 2,000,000) solution. The applied electric field was 132 kV/m. The time difference between the frames depicted is 50μs. Arrow points to the string attached between the beads.

Nevertheless, it is noted that the application of high externally applied electric field can suppress or eliminate this capillary instability. For 0.5 wt%, PEO (M_w = 2,000,000), the change from 'beads-on-string' structure (Figure 6.5) to regular-sized fragmented fibers connecting with appreciably thin beads (Figure 6.6 (b)). This phenomenon is the direct consequence of the suppression of the capillary instability with an increase in the applied electric field from 132 to 212 kV/m with the other parameters kept constant.

It can be seen from Figure 6.6, the fragmented fibers have regular lengths of 458±72 μm for PEO (M_w = 2,000,000) solution shown in Figure 6.6 (b) and 101±11 μm for PEO (M_w = 600,000) solution in Figure 6.6 (a). The considerable reduction in the size of the fragmented polymer jet when the molecular weight of PEO is reduced from 2,000,000 to 600,000 for PEO solution can be attributed to the reduction in the entanglement of the polymer molecular chains corresponding to the reduction in molecular weight for the given polymer concentration. The regular size of the fragmented jets can be ascribed to the axisymmetric instability (capillary instability) experienced by the electrospun jet.

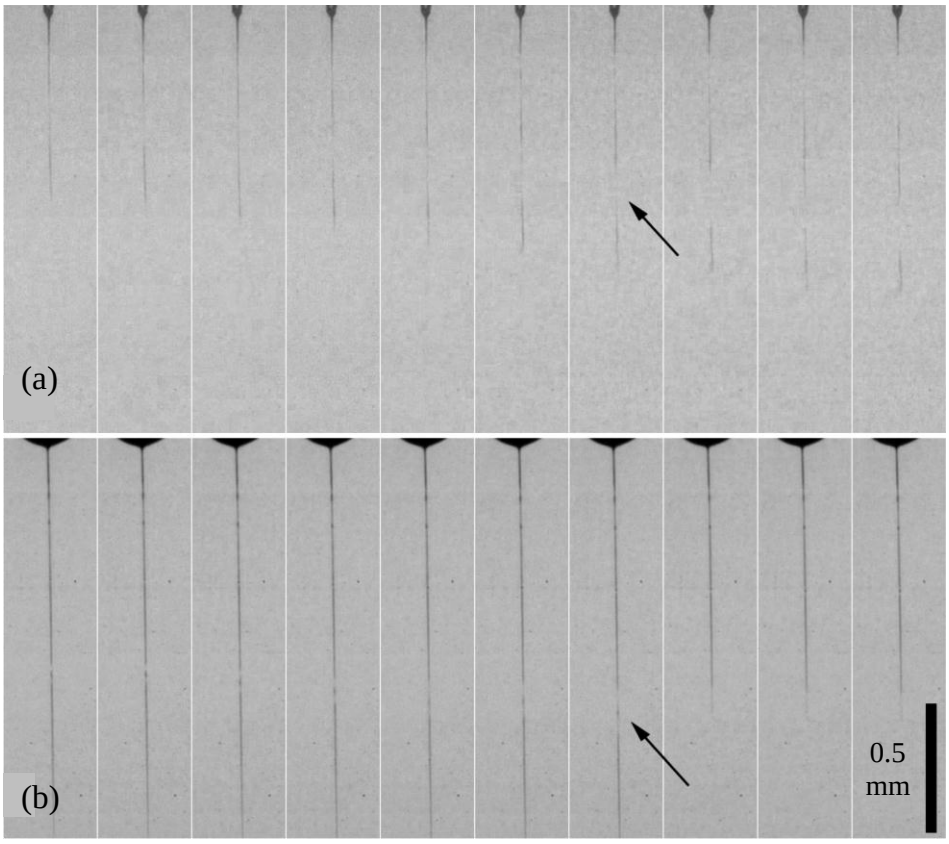

Figure 6.6 The fragmented jet phenomenon for (a) 0.5 wt% PEO (M_w = 600,000) solution. The applied electric field is 269 kV/m. The diameter of resultant fiber is 11 µm. The time difference between the frames depicted is 4.34 µs. Arrow points to the breaking of jet, no beads observed, (b) 0.5 wt% PEO (M_w = 2,000,000) solution. The applied electric field is 212 kV/m. The diameter of resultant fiber is 14 µm. The time difference between the frames depicted is 33.34 µs. Arrow points to the jet necking phenomenon taking place on both sides of a bead.

Capillary flow shown in Figure 6.5 stretch out fluid interfaces down to micrometric size under the effect of high-applied electric field strength (Figure 6.6). As the fragmented jets are invariably stretched from polymer drops, their regular size can be attributed to the regular size of the polymer droplets produced under the given operating conditions. For PEO (M_w = 2,000,000) solution, when the applied electric field is increased from 132 to 212 kV/m, the amount of stretching of the polymer chain as depicted by the average stretch rate has increased from 1×10^3 to $1.5 \times 10^4\ s^{-1}$ shown in Figure 6.7 (a).

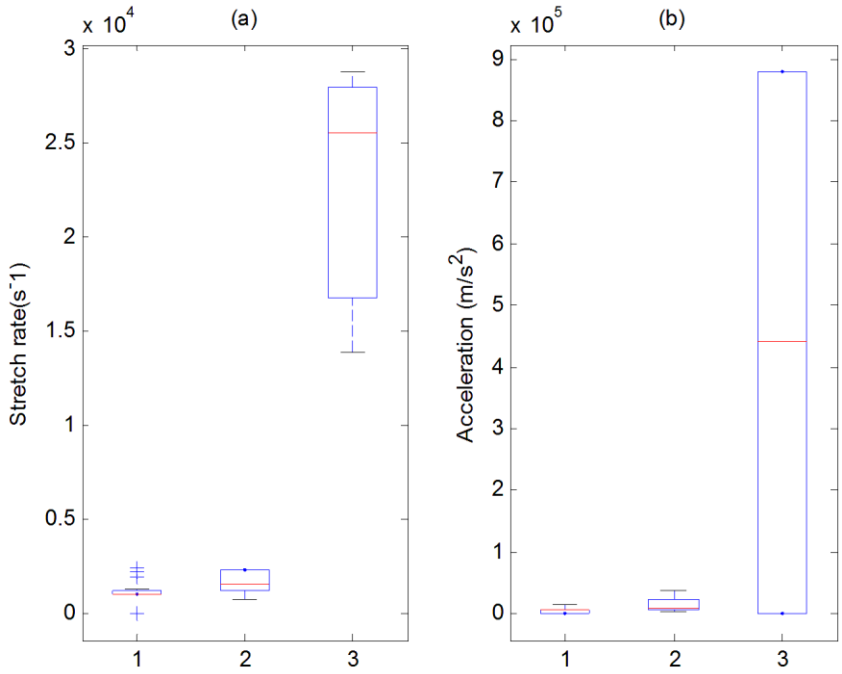

Figure 6.7 The variation of (a) stretch rate and (b) acceleration for three different experimental conditions for 0.5 wt% PEO solution, (1) M_w = 2,000,000 for applied electric field of 132 kV/m, (2) M_w = 2,000,000 for applied electric field of 212 kV/m, and (3) M_w = 600,000 for applied electric field of 269 kV/m.

The strain rate was calculated by following a polymer bead, i.e. a material point, over a period. The strain rate further increases to $2.5 \times 10^4\ s^{-1}$ for PEO ((M_w = 600,000) solution for an applied electric field strength of 269 kV/m (Figure 6.7 (a)). There is thus a progressive increase in stretchability corresponding to an increase in the applied electric strength, irrespective of the molecular weight of the polymer employed. For conventional electrospinning, the stretching was found to be on the order of $20s^{-1}$ for the straight section of the electrospun jet [24]. This implies at least two orders of the magnitude increase in the stretching of the polymer jet due to one order increase in the applied electric field in near-field electrospinning compared to conventional electrospinning

Acceleration analysis of the phenomenon is also performed as shown in Figure 6.7(b), which depicts acceleration on the order of 10^5 m/s^2 which is several orders of magnitude higher

than the acceleration due to gravity. This signifies that gravity has no effect on the underlying process, i.e. electrospinning can be performed in upside-down configuration [145]. The high value of the jet velocity and the associated high longitudinal strain rate imply that the macromolecules in the polymer jet are severely stretched and axially oriented. As the near-field electrospinning was able to surpass bending instability pertaining to electrospinning process, controlled deposition of fibers can be realized on an industrial-scale.

6.5 Conclusion

In this chapter, two novel techniques have been proposed for the mass production of fibers through electrospinning. They are a) laser induced electrospinning, and b) production of regular-sized microfibers through near-field electrospinning. In the first technique, a pulsed laser is focused inside the drop close to the liquid surface. The pulsed laser helped to overcome surface tension and produce an electrified jet. This approach was able to reduce the applied electric field to half of the value required for the conventional electrospinning, under identical operating parameters.

The second technique proposed yields regular-sized fragmented fibers. Using low concentrations of a polymer solution, the fragmentation of the polymer jet was observed for relatively high-applied electric field strengths, which resulted in the production of regular-sized fragmented fibers. As the technique was able to surpass bending instability pertaining to electrospinning, controlled deposition of fibers can be realized on an industrial-scale.

Chapter 7 Summary and Recommendation

7.1 Overall project summary

The thesis described an experimental study of the flow regimes pertaining to the electrospun jet and their characterization through relevant correlation formulae. Instabilities and failure modes experienced by the electrospun jet are also analyzed. Methods for the effective control of the electrospinning for the production of fibers were also proposed.

Dimensional analysis was performed to identify the salient dimensionless parameters, which govern the electrospun jet characteristics. Three new correlation formulae were obtained to characterize the three flow regimes of the electrospun jet from a polymer drop. Three dimensionless parameters, namely dimensionless apex diameter $\tilde{d}$, dimensionless flow rate $\tilde{Q}$, and dimensionless electric field $\tilde{E}$ were found to govern the jet characteristics at the apex of the Taylor cone. The relevant correlation formulae with/without the influence of electrical parameter were devised. Consequently, the correlation formula $\left(\tilde{d} = 1.03\tilde{Q}^{0.44}\right)$ for the diameter at the apex of the Taylor cone ignoring the weak $\tilde{E}$ effect was formulated. The correlation formula is valid for the analyzed range of *De* and *Re* based on jet radius, $4.2 \times 10^{-5} < De_r < 3.8 \times 10^{1}$ and $2.9 \times 10^{-3} < Re_r < 7.8$. The validity of the correlation formula was further increased with the help of literature data. Therefore, the correlation formula for the diameter at the apex of the Taylor cone with the addition of literature data is valid for the given range of dimensionless flow rates $\left(2.6 \times 10^{-4} < \tilde{Q} < 5.1 \times 10^{13}\right)$ and dimensionless electric fields $\left(6.7 \times 10^{-5} < \tilde{E} < 1.4 \times 10^{-1}\right)$ and dimensionless numbers, $3.3 \times 10^{-7} < De_{r_o} < 3.2 \times 10^{-1}$ and $2.0 \times 10^{-4} < Re_{r_o} < 7.0 \times 10^{-1}$.

Four independent dimensionless parameters, namely dimensionless electric field $\tilde{E}$, flow rate $\tilde{Q}$, axial length $\tilde{z}$, and diameter of the electrospun jet $\tilde{d}$ were found to govern the characteristics of the straight section of the electrospun jet. Subsequently, the two geometric dimensionless parameters $(\tilde{d}, \tilde{z})$ were combined to obtain a three-parameter system. Later, correlation formula with/without the influence of electrical parameter $\tilde{E}$ was devised. Finally, the analysis was reduced to a two-parameter-correlation formula $(\tilde{d}\tilde{z}^{1/4} = 1.09\tilde{Q}^{1/2})$ after ignoring the weak $\tilde{E}$ effect. The correlation formula is valid for the analyzed range of *De* and *Re* based on jet radius, $3.3 \times 10^{-4} < De_r < 4.7 \times 10^{4}$ and $2.9 \times 10^{-3} < Re_r < 3.9 \times 10^{1}$. The validity of the correlation formula was further increased with the help of literature data. Therefore, the correlation formula for the diameter at different locations along the jet's straight section is valid for the given range of dimensionless flow rates $(2.6 \times 10^{-4} < \tilde{Q} < 5.9 \times 10^{7})$ and dimensionless electric fields $(5.6 \times 10^{-4} < \tilde{E} < 1.4 \times 10^{-1})$ and dimensionless numbers, $3.3 \times 10^{-7} < De_{r_o} < 3.8 \times 10^{-2}$ and $2.0 \times 10^{-4} < Re_{r_o} < 7.0 \times 10^{-1}$.

Three dimensionless parameters, namely dimensionless length of the straight section of electrospun jet $\widetilde{Z_{\text{in}}}$, dimensionless flow rate $\tilde{Q}$, and dimensionless electric field $\tilde{E}$ were found to govern the length of the straight section of electrospun jet. Finally, the correlation formula $(\widetilde{Z_{\text{in}}} = 86\tilde{Q}^{0.42})$ for the length of the straight section of electrospun jet, ignoring the weak $\tilde{E}$ effect, was formulated. The analysis is valid for the analyzed range of *De* and *Re* based on jet radius, $3.3 \times 10^{-4} < De_r < 4.7 \times 10^{4}$ and $2.9 \times 10^{-3} < Re_r < 3.9 \times 10^{1}$.

Instabilities and failure modes experienced by the electrospun jet were analyzed. These instabilities include bending (first-order instability) and branching (higher-order

instability). In order to characterize bending instability, an imaging system was designed to obtain images at different time instances of the concerned phenomenon. These time-resolved images pertaining to bending instability helped to characterize it against the process as well as the material parameters. The parameters calculated in order to characterize bending instability include wavelength, growth rate as well as their phase velocity. Dimensionless wavelength was found to have a strong relationship with dimensionless applied electric field, i.e. $\widetilde{\lambda_{in}} \sim \left(\tilde{E}\right)^{-2}$. The dimensionless growth rate and phase velocity were found to have strong relationship with the dimensionless flow rate, i.e. $\tilde{\alpha} \sim \left(\tilde{Q}\right)^{-3.9}$ and $\widetilde{v_p} \sim \left(\tilde{Q}\right)^{0.23}$, respectively. The analysis is valid for the given range of dimensionless numbers; $1.6 \times 10^{-3} < De_{r_o} < 3.8 \times 10^{-2}$ and $5.8 \times 10^{-4} < Re_{r_o} < 1.2 \times 10^{-2}$. The failure modes of the electrospun jet during bending instability were also investigated. Three failure modes were observed during the analysis. Two of these failure modes were found to be the direct consequence of axisymmetric instability experienced by the electrospun jet. On the other hand, lack of viscosity of the polymer solution and lower polymer chain entanglement was considered responsible for the third mode.

Linear stability analysis of the electrified jet, including non-Newtonian effects was performed to characterize higher-order instability. The linear stability analysis helped to predict the axial wavelength corresponding to the highest order azimuthal mode. Subsequently, the axial wavelength was compared against the experimentally determined inter-undulation distance. The discrepancy in the results was attributed to the choice of the dominant azimuthal mode. Through experimental data, the dominant azimuthal mode was obtained as 2. Therefore, the theoretical model was reanalyzed against $n = 2$ to calculate the effect of relevant dimensionless parameters on the inter-undulation distance. Dimensionless

parameter $\bar{A}$ was found to decrease with an increase in applied electric field strength thus invalidating the assumption of a predominantly radial electric field made in the theoretical model.

Techniques for the effective control of electrospinning were proposed. The first technique used a pulsed laser focused inside the drop close to the liquid surface. The pulse cavitates the liquid and produces a protrusion from the tip of the drop. The protrusion narrowed by drainage and vertical stretching, thus concentrating the electric field and increasing the charge density, until it overcame the surface tension and produces the electrified jet. This approach can potentially reduce the required value of applied electric field to half its value required to start the conventional electrospinning from a stationary drop. The second technique proposed produced regular-sized microfibers with the help of near-field electrospinning. For low concentrations of a polymer solution emitting from micro-sized nozzles, the fragmentation of a polymer jet into regular-sized fragments was observed for relatively high-applied electric field strengths. Mass production of regular sized microfibers can be rendered feasible using these technologies.

In conclusion, although electrospinning is a promising technology for the production of variety of nanofiber architectures, there is still work to be done to precisely control and optimize the process. It was envisioned that the devised correlation formulae presented in this thesis would help in the determination of appropriate jet characteristics to control, optimize, and improve the electrospinning phenomenon.

7.2 Suggestions for future work

Finally, to put this research in future context and define its industrial directions, we have presented a critical account of the flow dynamics of the electrospun jet. All three-flow regimes pertaining to electrospun jet were critically analyzed. The experimental work was presented and correlated with the theoretical analysis. Techniques for the control of the electrospinning were also presented. Based on the work described in this thesis, some recommendations regarding future research are suggested.

- In the dimensional analysis performed in the thesis, non-Newtonian rheology was incorporated *ad hoc* via empirical relation for the extensional viscosity. A future task can be to incorporate relevant dimensionless parameters into the electro-hydrodynamics of the problem.
- The solvent used in the polymer-solvent system employed for the dimensional analysis was water, a relatively less volatile solvent. Nevertheless, highly volatile solvents are also employed in electrospinning. These highly volatile solvents can result in the variation of material parameters along the straight section of the electrospun jet. An extension of this work can be to investigate the effect of solvent evaporation on the proposed correlation formulae.
- During the linear stability analysis for the higher-order instability of the electrified jet, the assumption of predominantly radial electric field was invalidated. Another extension of this work can be to incorporate the effect of non-negligible axial electric field in the theoretical model.
- For laser-induced electrospinning, results are found to be robust, but can clearly be optimized by adjusting the laser depth and pulse energy. However, our setup does not

allow for inflow into the drop to replenish it, and we cannot tell if the spinning has reached a fully steady state. One drawback of the technique is that it will not work with opaque liquids. In those cases, laser ablation might work, where the laser is directed through the air onto the liquid surface. The process can be extended by designing a setup having an array of laser beams hitting at different locations on a sheet of polymer solution. The proposed setup will result in multiple electrospun jets ensuring high throughput.

- The near-field electrospinning produces a combination of fragmented electrospun fibers, necked fibers and fibers having a non-uniform cross-sectional radius. This implies that fine-tuning of the process as well as the material parameters have to be done to optimize the process for the production of mostly regular-sized polymer fibers.

Bibliography

[1] A. D. Yoffe, Low-dimensional systems-quantum-size effects and electronic properties of semiconductor microcrystallites (zero-dimensional systems) and some quasi-2-dimensional systems, *Adv. Phys.*, 42 (1993) 173-266.

[2] H. R. Heulings, X. Y. Huang, J. Li, T. Yuen, C. L. Lin, Mn-substituted inorganic-organic hybrid materials based on ZnSe: nanostructures that may lead to magnetic semiconductors with a strong quantum confinement effect, *Nano Lett.*, 1 (2001) 521-525.

[3] W. Hipp, H. Karl, I. Grosshans, B. Stritzker, Quantum confinement in CdSe-nanocrystallites synthesized by ion implantation, *Mater. Sci. Eng., B*, 101 (2003) 318-323.

[4] J. Tang, L. Brzozowski, D. A. R. Barkhouse, X. H. Wang, R. Debnath, R. Wolowiec, E. Palmiano, L. Levina, A. G. Pattantyus-Abraham, D. Jamakosmanovic, E. H. Sargent, Quantum dot photovoltaics in the extreme quantum confinement regime: The surface-chemical origins of exceptional air-and light-stability, *Acs Nano*, 4 (2010) 869-878.

[5] L. Zhang, P. Liu, Facile fabrication of uniform polyaniline nanotubes with tubular aluminosilicates as templates, *Nanoscale Res. Lett*., 3 (2008) 299-302.

[6] S. Dougherty, J. Liang, Fabrication of segmented nanofibers by template wetting of multilayered alternating polymer thin films, *J. Nanopart. Res*., 11 (2009) 743-747.

[7] H. Kaplan-Diedrich, G. H. Frischat, Drawing of oxynitride glass fibers, *Glastech. Ber. Glass. Sci. Technol.*, 70 (1997) 109-112.

[8] Y. Baik, S. Lee, Y. Jang, S. Kim, Unidirectional alignment of carbon nano-sized fiber using drawing process, *J. Mater. Sci.*, 40 (2005) 6037-6039.

[9] L. F. Zhang, Y. L. Hsieh, Ultra-fine cellulose acetate/poly(ethylene oxide) bicomponent fibers, *Carbohydr. Polym.*, 71 (2008) 196-207.

[10] S. C. Suen, W. T. Whang, F. J. Hou, B. T. Dai, Low-temperature self-assembly of copper phthalocyanine nanofibers, Org. *Electron.*, 7 (2006) 428-434.

[11] H. Mao, X. F. Lu, D. M. Chao, L. L. Cui, W. J. Zhang, Self-assembly synthesis of hollow, core-shell and solid soluble oligo (3,4-ethylenedioxythiophene) microspheres in a mixed solvent, *Mater. Lett.*, 62 (2008) 2543-2546.

[12] V. Vohra, U. Giovanella, R. Tubino, H. Murata, C. Botta, Electroluminescence from conjugated polymer electrospun nanofibers in solution processable organic light-emitting diodes, *Acs Nano*, 5 (2011) 5572-5578.

[13] P. Zhang, C. Shao, Z. Zhang, M. Zhang, J. Mu, Z. Guo, Y. Liu, TiO2@carbon core/shell nanofibers: Controllable preparation and enhanced visible photocatalytic properties, *Nanoscale*, 3 (2011) 2943-2949.

[14] G. I. Taylor, Disintegration of water drops in an electric field, *Proc. R. Soc. London*, Ser. A, 280 (1964) 383-397.

[15] G. I. Taylor, Electrically driven jets, *Proc. R. Soc. London.*, 313 (1969) 453-475.

[16] J. F. Cooley, Improved methods of and apparatus for electrically separating the relatively volatile liquid component from the component of relatively fixed substances of composite fluids, Patent: *GB 06385*, (1900).

[17] A. Formhals, Production of artificial fibers, Patent: *US 2323025*, (1943).

[18] A. Formhals, Method and apparatus for spinning, Patent: *US 2349950*, (1944).

[19] A. Formhals, Artificial fiber construction, Patent: *US 2109333*, (1938).

[20] P. K. Baumgarten, Electrostatic spinning of acrylic microfibers, *J. Colloid Interface Sci.*, 36 (1971) 71-79.

[21] L. Larrondo, R. S. J. Manley, Electrostatic fiber spinning from polymer melts. I. Experimental observations on fiber formation and properties, *J. Polym. Sci., Polym. Phys. Ed.*, 19 (1981) 909-920.

[22] L. Larrondo, R. S. J. Manley, Electrostatic fiber spinning from polymer melts. II. Examination of the flow field in an electrically driven jet, *J. Polym. Sci, Polym. Phys. Ed.*, 19 (1981) 921-932.

[23] L. Larrondo, R. S. J. Manley, Electrostatic fiber spinning from polymer melts. III. Electrostatic deformation of a pendant drop of polymer melts, *J. Polym. Sci., Polym. Phys. Ed.*, 19 (1981) 933-940.

[24] A. L. Yarin, S. Koombhongse, D. H. Reneker, Bending instability in electrospinning of nanofibers, *J. Appl. Phys.*, 89 (2001) 3018-3026.

[25] A. L. Yarin, S. Koombhongse, D. H. Reneker, Taylor cone and jetting from liquid droplets in electrospinning of nanofibers, *J. Appl. Phys.*, 90 (2001) 4836-4846.

[26] M. M. Hohman, M. Shin, G. Rutledge, M. P. Brenner, Electrospinning and electrically forced jets. II. Applications, *Phys. Fluids*, 13 (2001) 2221-2236.

[27] M. M. Hohman, M. Shin, G. Rutledge, M. P. Brenner, Electrospinning and electrically forced jets. I. Stability theory, *Phys. Fluids*, 13 (2001) 2201-2220.

[28] J. J. Feng, The stretching of an electrified non-Newtonian jet: A model for electrospinning, *Phys. Fluids*, 14 (2002) 3912-3926.

[29] J. J. Feng, Stretching of a straight electrically charged viscoelastic jet, *J. Non-Newtonian Fluid Mech.*, 116 (2003) 55-70.

[30] T. Han, A. L. Yarin, D. H. Reneker, Viscoelastic electrospun jets: Initial stresses and elongational rheometry, *Polymer*, 49 (2008) 1651-1658.

[31] S. A. Theron, E. Zussman, A. L. Yarin, Experimental investigation of the governing parameters in the electrospinning of polymer solutions, *Polymer*, 45 (2004) 2017-2030.

[32] W. Zuo, M. Zhu, W. Yang, H. Yu, Y. Chen, Y. Zhang, Experimental study on relationship between jet instability and formation of beaded fibers during electrospinning, *Polym. Eng. Sci*., 45 (2005) 704-709.

[33] Y. Ishii, H. Sakai, H. Murata, Fabrication of a submicron patterned electrode using an electrospun single fiber as a shadow-mask, *Thin Solid Films*, 518 (2009) 647-650.

[34] D. Li, G. Ouyang, J. T. McCann, Y. Xia, Collecting electrospun nanofibers with patterned electrodes, *Nano Lett.*, 5 (2005) 913-916.

[35] F. L. Zhou, P. L. Hubbard, S. J. Eichhorn, G. J. M. Parker, Jet deposition in near-field electrospinning of patterned polycaprolactone and sugar-polycaprolactone core-shell fibres, *Polymer*, 52 (2011) 3603-3610.

[36] X. F. Wang, K. Zhang, M. F. Zhu, H. Yu, Z. Zhou, Y. M. Chen, B. S. Hsiao, Continuous polymer nanofiber yarns prepared by self-bundling electrospinning method, *Polymer*, 49 (2008) 2755-2761.

[37] E. Smit, U. Buttner, R. D. Sanderson, Continuous yarns from electrospun fibers, *Polymer*, 46 (2005) 2419-2423.

[38] B. K. Gu, M. K. Shin, K. W. Sohn, S. I. Kim, S. J. Kim, S. K. Kim, H. Lee, J. S. Park, Direct fabrication of twisted nanofibers by electrospinning, *Appl. Phys. Lett*., 90 (2007) 3.

[39] L. M. Bellan, H. G. Craighead, Nanomanufacturing using electrospinning, *J. Manuf. Sci. Eng.*,131 (2009) 0340011-0340014.

[40] Y. L. Hong, Y. A. Li, X. L. Zhuang, X. S. Chen, X. B. Jing, Electrospinning of multicomponent ultrathin fibrous nonwovens for semi-occlusive wound dressings, *J. Biomed. Mater. Res., A*, 89A (2009) 345-354.

[41] N. Wang, H. Chen, L. Lin, Y. Zhao, X. Cao, Y. Song, L. Jiang, Multicomponent phase change microfibers prepared by temperature control multifluidic electrospinning, *Macromol. Rapid Commun*., 31 (2010) 1622-1627.

[42] M. V. Jose, V. Thomas, Y. Y. Xu, S. Bellis, E. Nyairo, D. Dean, Aligned bioactive multi-component nanofibrous nanocomposite scaffolds for bone tissue engineering, *Macromol. Biosci.,* 10 (2010) 433-444.

[43] L. Al-Mashat, H. D. Tran, W. Wlodarski, R. B. Kaner, K. Katantar-Zadeh, Conductometric hydrogen gas sensor based on polypyrrole nanofibers, *IEEE Sens. J.*, 8 (2008) 365-370.

[44] R. Arsat, X. F. Yu, Y. X. Li, W. Wlodarski, K. Kalantar-zadeh, Hydrogen gas sensor based on highly ordered polyaniline nanofibers, *Sens. Actuators, B*, 137 (2009) 529-532.

[45] J. An, H. Zhang, J. T. Zhang, Y. H. Zhao, X. Y. Yuan, Preparation and antibacterial activity of electrospun chitosan/poly(ethylene oxide) membranes containing silver nanoparticles, *Colloid. Polym. Sci.*, 287 (2009) 1425-1434.

[46] M. Botes, T. E. Cloete, The potential of nanofibers and nanobiocides in water purification, *Crit. Rev. Microbiol.*, 36 (2010) 68-81.

[47] G. P. Dong, X. D. Xiao, X. F. Liu, B. Qian, Y. Liao, C. Wang, D. P. Chen, J. R. Qiu, Functional Ag porous films prepared by electrospinning, *Appl. Surf. Sci.*, 255 (2009) 7623-7626.

[48] J. Hu, P. X. Ma, Nano-fibrous tissue engineering scaffolds capable of growth factor delivery, *Pharm. Res.*, 28 (2011) 1273-1281.

[49] Y. Y. Huang, D. Y. Wang, L. L. Chang, Y. C. Yang, Fabricating microparticles/nanofibers composite and nanofiber scaffold with controllable pore size by rotating multichannel electrospinning, *J. Biomater. Sci., Polym. Ed.*, 21 (2010) 1503-1514.

[50] J. H. Jang, O. Castano, H. W. Kim, Electrospun materials as potential platforms for bone tissue engineering, *Adv. Drug Deliv. Rev.*, 61 (2009) 1065-1083.

[51] H. M. Cao, Y. H. Zhu, X. Tan, H. G. Kang, X. L. Yang, C. Z. Li, Fabrication of TiO(2)/CdS composite fiber via an electrospinning method, *New J. Chem.*, 34 (2010) 1116-1119.

[52] M. A. Kanjwal, N. A. M. Barakat, F. A. Sheikh, S. J. Park, H. Y. Kim, Photocatalytic activity of ZnO-TiO2 hierarchical nanostructure prepared by combined electrospinning and hydrothermal techniques, *Macromol. Res.*, 18 (2010) 233-240.

[53] Y. Yang, C. C. Zhang, Y. Xu, H. Y. Wang, X. Li, C. Wang, Electrospun Er:TiO2 nanofibrous films as efficient photocatalysts under solar simulated light, *Mater. Lett.,* 64 (2010) 147-150.

[54] R. S. Barhate, S. Ramakrishna, Nanofibrous filtering media: Filtration problems and solutions from tiny materials, *J. Membr. Sci.,* 296 (2007) 1-8.

[55] K. M. Yun, A. B. Suryamas, F. Iskandar, L. Bao, H. Niinuma, K. Okuyama, Morphology optimization of polymer nanofiber for applications in aerosol particle filtration, *Sep. Purif. Technol.,* 75 (2010) 340-345.

[56] W. Sambaer, M. Zatloukal, D. Kimmer, 3D modeling of filtration process via polyurethane nanofiber based nonwoven filters prepared by electrospinning process, *Chem. Eng. Sci*., 66 (2011) 613-623.

[57] C. Drew, X. Y. Wang, K. Senecal, H. Schreuder-Gibson, J. N. He, J. Kumar, L. A. Samuelson, Electrospun photovoltaic cells, *J. Macromol. Sci. - Pure Appl. Chem.*, A39 (2002) 1085-1094.

[58] P. Joshi, L. Zhang, D. Davoux, Z. Zhu, D. Galipeau, H. Fong, Q. Qiao, Composite of TiO2 nanofibers and nanoparticles for dye-sensitized solar cells with significantly improved efficiency, *Energy Environ. Sci.*, 3 (2010) 1507-1510.

[59] S. W. Lee, H. J . Lee, J. H. Choi, W. G. Koh, J. M. Myoung, J. H. Hur, J. J. Park, J. H. Cho, U. Jeong, Periodic array of polyelectrolyte-gated organic transistors from electrospun poly(3-hexylthiophene) nanofibers, *Nano Lett*., 10 (2010) 347-351.

[60] K. J. Aviss, J. E. Gough, S. Downes, Aligned electrospun polymer fibres for skeletal muscle regeneration, *Eur. Cells Mater.*, 19 (2010) 193-204.

[61] G. Dong, X. Xiao, Y. Chi, B. Ian, X. Liu, Z. Ma, S. Ye, E. Wu, H. Zeng, D. Chen, J. Qiu, Polarized luminescence properties of TiO2:Sm3+ microfibers and microbelts prepared by electrospinning, *J. Phys. Chem. C*, 113 (2009) 9595-9600.

[62] M. Maly, S. Petrik, Production technology for nanofiber filtration media, *Nanotech NSTI*, 2010, 673 - 676.

[63] W. E. Teo, M. Kotaki, X. M. Mo, S. Ramakrishna, Porous tubular structures with controlled fibre orientation using a modified electrospinning method, *Nanotechnology*, 16 (2005) 918-924.

[64] P. Katta, M. Alessandro, R. D. Ramsier, G. G. Chase, Continuous electrospinning of aligned polymer nanofibers onto a wire drum collector, *Nano Lett*., 4 (2004) 2215-2218.

[65] B. Sundaray, V. Subramanian, T. S. Natarajan, R. Z. Xiang, C. C. Chang, W. S. Fann, Electrospinning of continuous aligned polymer fibers, *Appl. Phys. Lett.*, 84 (2004) 1222 - 1225

[66] E. Zussman, A. Theron, A. L. Yarin, Formation of nanofiber crossbars in electrospinning, *Appl. Phys. Lett*., 82 (2003) 973-975.

[67] R. Furlan, S. V. Arroyo, R. O. F. Torres, J. A. M. Rosado, A. N. R. da Silva, Study of nanofiber formation by injecting polymeric solutions inside intense electric fields using different electrode configurations, *J. Integr. Circ. Syst.*, 5 (2010) 148-153.

[68] D. Li, Y. Wang, Y. Xia, Electrospinning nanofibers as uniaxially aligned arrays and layer-by-layer stacked films, *Adv. Mater*., 16 (2004) 361-366.

[69] D. Li, Y. Wang, Y. Xia, Electrospinning of polymeric and ceramic nanofibers as uniaxially aligned arrays, *Nano Lett*., 3 (2003) 1167-1171.

[70] C. Berkland, D. W. Pack, K. Kim, Controlling surface nano-structure using flow-limited field-injection electrostatic spraying (FFESS) of poly(D, L-lactide-co-glycolide), *Biomaterials*, 25 (2004) 5649-5658.

[71] Y. Wu, R. L. Clark, Electrohydrodynamic atomization: A versatile process for preparing materials for biomedical applications, *J. Biomater. Sci., Polym. Ed.*, 19 (2008) 573-601.

[72] Salata O. V, Tools of Nanotechnology: Electrospray, *Curr. Nanosci.*, 1 (2005) 25-33.

[73] L. Rayleigh, On the instability of a cylinder of viscous liquid under capillary forces, *Philos. Mag. 5*, 34 (1982) 145-154.

[74] J. Zeleny, The electrical discharge from liquid points, and a hydrostatic method of measuring the electric intensity at their surfaces, *Phys. Rev.*, 3 (1914) 69-91.

[75] J. Zeleny, Instability of electrified liquid surfaces, *Phys. Rev.*, 10 (1917) 1-6.

[76] D. A. Saville, Electrohydrodynamics: The Taylor-Melcher leaky dielectric model, *Annu. Rev. Fluid Mech.*, 29 (1997) 27-64.

[77] A. Spivak, Y. Dzenis, Asymptotic decay of radius of a weakly conductive viscous jet in an external electric field, *Appl. Phys. Lett.*, 73 (1998) 3067-3069.

[78] D. H. Reneker, I. Chun, Nanometre diameter fibres of polymer produced by electrospinning, *Nanotechnology*, 7 (1996) 216-223.

[79] Y. M. Shin, M. M. Hohman, M. P. Brenner, G. C. Rutledge, Experimental characterization of electrospinning: The electrically forced jet and instabilities, *Polymer*, 42 (2001) 9955-9967.

[80] C. Chang, K. Limkrailassiri, L. Lin, Continuous near-field electrospinning for large area deposition of orderly nanofiber patterns, *Appl. Phys. Lett.,* 93 (2008).

[81] A. L. Yarin, W. Kataphinan, D. H. Reneker, Branching in electrospinning of nanofibers, *J. Appl. Phys.,* 98 (2005) 1-12.

[82] Y. Yang, Z. Jia, J. Liu, Q. Li, L. Hou, L. Wang, Z. Guan, Effect of electric field distribution uniformity on electrospinning, *J. Appl. Phys.*, 103 (2008).

[83] J. H. Yu, S. V. Fridrikh, G. C. Rutledge, The role of elasticity in the formation of electrospun fibers, *Polymer*, 47 (2006) 4789-4797.

[84] J. Brandrup, E. H. Immergut, Polymer handbook, 2th ed, *Interscience Publishers*, 1966.

[85] M. G. McKee, The influence of branching and intermolecular interactions on the formation of electrospun fibers, Phd thesis, Virginia Polytechnic Institute and State University, 2005.

[86] M. E. Helgeson, K. N. Grammatikos, J. M . Deitzel, N. J. Wagner, Theory and kinematic measurements of the mechanics of stable electrospun polymer jets, *Polymer*, 49 (2008) 2924-2936.

[87] O. Arnolds, H. Buggisch, D. Sachsenheimer, N. Willenbacher, Capillary breakup extensional rheometry (CaBER) on semi-dilute and concentrated polyethylene oxide (PEO) solutions, *Rheol. Acta*, 49 (2010) 1207-1217.

[88] H. Fong, I. Chun, D. H. Reneker, Beaded nanofibers formed during electrospinning, *Polymer*, 40 (1999) 4585-4592.

[89] A. Jaworek, A. Krupa, M. Lackowski, A. T. Sobczyk, T. Czech, S. Ramakrishna, S. Sundarrajan, D. Pliszka, Nanocomposite fabric formation by electrospinning and electrospraying technologies, *J. Electrost.*, 67 (2009) 435-438.

[90] J. F. De La Mora, The fluid dynamics of Taylor cones, *Annu. Rev. Fluid Mech*., 39 (2007) 217-243.

[91] A. Barrero, I. G. Loscertales, Micro- and nanoparticles via capillary flows, *Annu. Rev. Fluid Mech.*, 39 (2007) 89-106.

[92] J. F. De La Mora, I. G. Loscertales, The current emitted by highly conducting Taylor cones, *J. Fluid Mech*., 260 (1994) 155-184.

[93] A. M. Ganan-Calvo, Cone-jet analytical extension of Taylor's electrostatic solution and the asymptotic universal scaling laws in electrospraying, *Phys. Rev. Lett*., 79 (1997) 217-220.

[94] V. N. Kirichenko, I. V. Petryanov Sokolov, N. N. Suprun, A. A. Shutov, Asymptotic radius of a slightly conducting liquid jet in an electric field, *Sov. Phys. Dokl*., 31 (1986) 611.

[95] S. Reznik, E. Zussman, Capillary-dominated electrified jets of a viscous leaky dielectric liquid, *Phys. Rev. E*, 81 (2010) 026313.

[96] G. C. Rutledge, S. V. Fridrikh, Formation of fibers by electrospinning, A*dv. Drug Deliv. Rev.*, 59 (2007) 1384-1391.

[97] I. Greenfeld, K. Fezzaa, M. H. Rafailovich, E. Zussman, Fast x-ray phase-contrast imaging of electrospinning polymer jets: measurements of radius, velocity, and concentration, *Macromolecules*, 45 (2012) 3616-3626.

[98] M. M. Hohman, A physical theory of the instabilities of electrically driven jets, Ph.D. thesis, University of Chicago, Department of Physics, 2000.

[99] M. M. Demir, I. Yilgor, E. Yilgor, B. Erman, Electrospinning of polyurethane fibers, *Polymer*, 43 (2002) 3303-3309.

[100] S. H. Tan, R. Inai, M. Kotaki, S. Ramakrishna, Systematic parameter study for ultra-fine fiber fabrication via electrospinning process, *Polymer*, 46 (2005) 6128-6134.

[101] J. M. Deitzel, J. Kleinmeyer, D. Harris, N. C. Beck Tan, The effect of processing variables on the morphology of electrospun nanofibers and textiles, *Polymer*, 42 (2001) 261-272.

[102] C. Wang, Y. W. Cheng, C. H. Hsu, H. S. Chien, S. Y. Tsou, How to manipulate the electrospinning jet with controlled properties to obtain uniform fibers with the smallest diameter?- a brief discussion of solution electrospinning process, *J. Polym. Res.*, 18 (2011) 111-123.

[103] A. M. Afifi, H. Yamane, Y. Kimura, Effect of polymer molecular weight on the electrospinning of polylactides in entangled and aligned fiber forms, *Sen-I Gakkaishi*, 66 (2010) 35-42.

[104] T. Jarusuwannapoom, W. Hongroijanawiwat, S. Jitjaicham, L. Wannatong, M. Nithitanakul, C. Pattamaprom, P. Koombhongse, R. Rangkupan, P. Supaphol, Effect of solvents on electro-spinnability of polystyrene solutions and morphological appearance of resulting electrospun polystyrene fibers, *Eur. Polym. J.*, 41 (2005) 409-421.

[105] C. J. Thompson, G. G. Chase, A. L. Yarin, D. H. Reneker, Effects of parameters on nanofiber diameter determined from electrospinning model, *Polymer*, 48 (2007) 6913-6922.

[106] H. Otake, T. Hayashida, K. Kitamura, T. Arai, J. Yonai, K. Tanioka, H. Maruyama, T. Eto, Development of 300,000-pixel ultrahigh-speed high-sensitivity CCD and a single-chip color camera mounting this CCD, *NHK Giken R&D*, (2006) 38-47.

[107] C. P. Carroll, Y. L. Joo, Axisymmetric instabilities of electrically driven viscoelastic jets, *J. Non-Newtonian Fluid Mech.*, 153 (2008) 130-148.

[108] W. K. Son, J. H. Youk, T. S. Lee, W. H. Park, The effects of solution properties and polyelectrolyte on electrospinning of ultrafine poly(ethylene oxide) fibers, *Polymer*, 45 (2004) 2959-2966.

[109] X. H. Zong, K. Kim, D. F. Fang, S. F. Ran, B. S. Hsiao, B. Chu, Structure and process relationship of electrospun bioabsorbable nanofiber membranes, *Polymer*, 43 (2002) 4403-4412.

[110] K. H. Lee, H. Y. Kim, M. S. Khil, Y. M. Ra, D. R. Lee, Characterization of nano-structured poly(epsilon-caprolactone) nonwoven mats via electrospinning, *Polymer*, 44 (2003) 1287-1294.

[111] N. Bhattarai, D. Cha, S. R. Bhattarai, M. S. Khil, H. Y. Kim, Biodegradable electrospun mat: Novel block copolymer of poly(p-dioxanone-co-L-lactide)-block-poly (ethylene glycol), *J. Polym. Sci. Pt. B-Polym. Phys.*, 41 (2003) 1955-1964.

[112] S. Sukigara, M. Gandhi, J. Ayutsede, M. Micklus, F. Ko, Regeneration of Bombyx mori silk by electrospinning. Part 2. Process optimization and empirical modeling using response surface methodology, *Polymer*, 45 (2004) 3701-3708.

[113] B. Yesilata, C. Clasen, G. H. McKinley, Nonlinear shear and extensional flow dynamics of wormlike surfactant solutions, *J. Non-Newtonian Fluid Mech.*, 133 (2006) 73-90.

[114] E. Zussman, D. Rittel, A. L. Yarin, Failure modes of electrospun nanofibers, *Appl. Phys. Lett.*, 82 (2003) 3958-3960.

[115] G. H. McKinley, Dimensionless groups for understanding free surface flows of complex fluids, *Soc. Rheol. Bull*, 2005 (2005) 6-9.

[116] D. H. Reneker, A. L. Yarin, Electrospinning jets and polymer nanofibers, *Polymer*, 49 (2008) 2387-2425.

[117] G. Tomar, V. Shankar, A. Sharma, G. Biswas, Electrohydrodynamic instability of a confined viscoelastic liquid film, *J. Non-Newtonian Fluid Mech.*, 143 (2007) 120-130.

[118] A. B. Basset, Waves and jets in a viscous liquid, *Am. J. Math.*, 16 (1894) 93-110.

[119] S. Middleman, Stability of a viscoelastic jet, *Chem. Eng. Sci*., 20 (1965) 1037-1040.

[120] G. Brenn, Z. Liu, F. Durst, Linear analysis of the temporal instability of axisymmetrical non-Newtonian liquid jets, *Int. J. Multiphase Flow*, 26 (2000) 1621-1644.

[121] Z. Liu, Linear analysis of three-dimensional instability of non-Newtonian liquid jets, *J. Fluid Mech*., 559 (2006) 451-459.

[122] F. Li, X. Y. Yin, X. Z. Yin, Axisymmetric and non-axisymmetric instability of an electrically charged viscoelastic liquid jet, *J. Non-Newtonian Fluid Mech.*, 166 (2011) 1024-1032.

[123] L. Wu, S. Y. Chou, Electrohydrodynamic instability of a thin film of viscoelastic polymer underneath a lithographically manufactured mask, *J. Non-Newtonian Fluid Mech.*, 125 (2005) 91-99.

[124] A. Theron, E. Zussman, A. L. Yarin, Measurements of the governing parameters in the electrospinning of polymer solutions, *Proc. of the 226th ACS Meeting*, New York City, 226 (2003) U424-U425.

[125] A. L. Yarin, Electrospinning of nanofibers from polymer solutions and melts, lecture notes, ISSN 1642-0578, Institute of fundamental technological research, Polish academy of sciences, Warsaw 2003.

[126] R. H. Perry, D. W. Green, Perry's chemical engineers' handbook, 3rd ed, McGraw-Hill New York, 2008.

[127] A. L. Yarin, Stability of a jet of viscoelastic liquid in the presence of a mass flux at its surface, *J. Eng. Phys.*, 37 (1980) 904-910.

[128] F. Li, X. Y. Yin, X. Z. Yin, Axisymmetric and non-axisymmetric instability of an electrified viscous coaxial jet, *J. Fluid Mech*., 632 (2009) 199-225.

[129] S. Chandrasekhar, Hydrodynamic and hydromagnetic stability, Dover publications, 1981.

[130] K. H. Lee, H. Y. Kim, Y. M. La, D. R. Lee, N. H. Sung, Influence of a mixing solvent with tetrahydrofuran and N, N-dimethylformamide on electrospun poly(vinyl chloride) nonwoven mats, *J. Polym. Sci. Pt. B- Polym. Phys.*, 40 (2002) 2259-2268.

[131] H. Q. Liu, Y. L. Hsieh, Ultrafine fibrous cellulose membranes from electrospinning of cellulose acetate, *J. Polym. Sci. Pt. B - Polym. Phys.*, 40 (2002) 2119-2129.

[132] G. Eda, J. Liu, S. Shivkumar, Flight path of electrospun polystyrene solutions: Effects of molecular weight and concentration, *Mater. Lett.*, 61 (2007) 1451-1455.

[133] P. Gupta, C. Elkins, T. E. Long, G. L. Wilkes, Electrospinning of linear homopolymers of poly(methyl methacrylate): Exploring relationships between fiber formation, viscosity, molecular weight and concentration in a good solvent, *Polymer*, 46 (2005) 4799-4810.

[134] R. Nagarajan, C. Drew, C. M. Mello, Polymer-micelle complex as an aid to electrospinning nanofibers from aqueous solutions, *J. Phys. Chem. C*, 111 (2007) 16105-16108.

[135] Q. P. Pham, U. Sharma, A. G. Mikos, Electrospinning of polymeric nanofibers for tissue engineering applications: A review, *Tissue Eng.*, 12 (2006) 1197-1211.

[136] S. Chakraborty, I. C. Liao, A. Adler, K. W. Leong, Electrohydrodynamics: A facile technique to fabricate drug delivery systems, *Adv. Drug Deliv. Rev.*, 61 (2009) 1043-1054.

[137] E. Ford, R. E. Popil, S. Kumar, Breathable water-resistant linerboard coatings by electrospraying application, *Bioresources*, 4 (2009) 714-729.

[138] E. García-Tamayo, M. Valvo, U. Lafont, C. Locati, D. Munao, E. M. Kelder, Nanostructured Fe2O3 and CuO composite electrodes for Li ion batteries synthesized and deposited in one step, *J. Power Sources*, 196 (2011) 6425-6432.

[139] J. K. Hong, S. V. Madihally, Three-dimensional scaffold of electrosprayed fibers with large pore size for tissue regeneration, *Acta Biomater.*, 6 (2010) 4734-4742.

[140] A. Jaworek, A. Krupa, M. Lackowski, A. T. Sobczyk, T. Czech, Novel electrostatic technologies for functional nanomaterials production, *Prz. Elektrotech.*, 86 (2010) 81-83.

[141] A. M. Ganan-Calvo, J. M. Lopez-Herrera, P. Riesco-Chueca, The combination of electrospray and flow focusing, *J. Fluid Mech.*, 566 (2006) 421-445.

[142] S. L. Shenoy, W. D. Bates, H. L. Frisch, G. E. Wnek, Role of chain entanglements on fiber formation during electrospinning of polymer solutions: Good solvent, non-specific polymer-polymer interaction limit, *Polymer*, 46 (2005) 3372-3384.

[143] J. Liu, S. Kumar, Microscopic polymer cups by electrospinning, *Polymer*, 46 (2005) 3211-3214.

[144] G. C. Yang, Y. Pan, J. Gong, C. L. Shao, S. B. Wen, C. Shao, L. Y. Qu, Beaded fiber mats of PVA containing unsaturated heteropoly salt, *Chin. Chem. Lett.*, 15 (2004) 1212-1214.

[145] A. L. Yarin, E. Zussman, Upward needleless electrospinning of multiple nanofibers, *Polymer*, 45 (2004) 2977-2980.

Appendix

The given functions $P(\chi,\xi)$, $Q(\chi,\xi)$ and $R(\chi,\xi)$ are employed in equation 5.15 presented in the theoretical model pertaining to the branching of the electrospun jet.

$$E_1 = (\xi)I'_{n+1}(\xi) - (n+1)I_{n+1}(\xi),$$

$$E_2 = -(\xi)I'_{n-1}(\xi) + (1-n)I_{n-1}(\xi),$$

$$E_3 = \chi\left(I'_{n+1}(\chi) - I'_{n-1}(\chi)\right) - (n+1)I_{n+1}(\chi) + (1-n)I_{n-1}(\chi),$$

$$E_4 = \xi^2 I''_{n+1}(\xi) + \xi(1+n)I'_{n+1}(\xi) - (n+1)I_{n+1}(\xi) + \chi^2 I_{n+1}(\xi)$$

$$E_5 = \xi^2 I''_{n-1}(\xi) + \xi(1+n)I'_{n-1}(\xi) + (n-1)I_{n-1}(\xi) + \chi^2 I_{n-1}(\xi)$$

$$E_6 = \chi^2\left(I''_{n+1}(\chi) + I''_{n-1}(\chi)\right) + \chi(1+n)I'_{n+1} + \chi(1-n)I'_{n-1} - (n+1)I_{n+1}(\chi) + (n-1)I_{n-1}(\chi) + \chi^2\left(I_{n+1}(\chi) + I_{n-1}(\chi)\right)$$

$$P(\chi,\xi) = \frac{(E_6E_1 - E_3E_4)}{(E_2E_4 - E_5E_1)}$$

$$Q(\chi,\xi) = \frac{(E_6E_2 - E_3E_5)}{(E_5E_1 - E_2E_4)}$$

$$R(\chi,\xi) = \tfrac{1}{2}\left[I_{n+1}(\xi)Q(\chi,\xi) + I_{n-1}(\xi)p(\chi,\xi) + \left(I_{n+1}(\xi) + I_{n-1}(\xi)\right)\right]$$

Author's Publications

Journal Papers

1) R. Sahay, C. J. Teo, S. T. Thoroddsen, 'Laser-induced onset of electrospinning,' Physical Review E, 81(3), 2010.
2) R. Sahay, C. J. Teo, Y. T. Chew, New correlation formulae for the straight section of the electrospun jet from a polymer drop,' Journal of fluid mechanics (under revision).
3) R. Sahay, C. J. Teo, Y. T. Chew, 'Experimental and theoretical analysis of branching of an electrospun jet,' Physics of Fluids (under revision).

Conference attended

4) Rahul Sahay, C. J. Teo, Y. T. Chew, S. T. Thoroddsen, 'Branching of an electrospinning jet,' 62nd Annual Meeting of the Division of fluid Dynamics, APS, 22-24 Nov, 2009.